



**MALAVIYA NATIONAL INSTITUTE OF TECHNOLOGY JAIPUR**  
(Institute of National Importance under NITs Act)  
(Established by Govt. of India)  
**JLN Marg, Jaipur-302017 (India)**

---

## **CERTIFICATE**

This is to certify that the thesis entitled “*Study on Ion Irradiation Induced Modifications of P3HT and PCBM Materials*” being submitted by **Trupti Sharma (ID No. 2013RPH9504)** is a bonafied research work carried out under my supervision and guidance in fulfillment of the requirement for the award of the degree of Doctor of Philosophy in the *Department of Physics*, Malaviya National Institute of Technology, Jaipur, India. The matter embodied in this thesis is original and has not been submitted to any other University or Institute for the award of any other degree.

Place: Jaipur

Date: 25-06-2018

(Dr. Rahul Singhal)  
Assistant Professor  
Department of Physics  
MNIT Jaipur (India)

(Dr. S. K. Biswas)  
Professor  
Department of Metallurgical  
& Material Engineering  
MNIT Jaipur (India)



# DECLARATION

I, Trupti Sharma, declare that this thesis titled, “*Study on Ion Irradiation Induced Modifications of P3HT and PCBM Materials*” and the work presented in it, are my own. I confirm that:

- This work was done wholly or mainly while, in candidature for a research degree at this university.
- Where any part of this thesis has previously been submitted for a degree or any other qualification at this university or any other institution, this has been clearly stated.
- Where I have consulted the published work of others, this is always clearly attributed.
- Where I have quoted from the work of others, the source is always given. With the exception of such quotations, this thesis is entirely my own work.
- I have acknowledged all main sources of help.
- Where the thesis is based on work done by myself, jointly with others, I have made clear exactly what was done by others and what I have contributed myself.

Date: 25-06-2018

**Trupti Sharma**  
**(2013RPH9504)**



# ACKNOWLEDGEMENT

First of all, I would like to express deep gratitude and respect to my thesis advisor, Dr. Rahul Singhal for his insightful guidance, encouragement and advice from the very early stage of my research work as well as giving me experiences throughout the work. The enthusiasm he has for research, was contagious and motivational for me. I am also thankful to him to provide opportunities for research, both on and off campus.

I would like to extend my sincere thanks to my second supervisor, Prof. S. K. Biswas, MNIT Jaipur for his constant support and his availability all the time during Ph.D. His constant encouragement, comments and suggestions throughout the research work and during thesis writing made this work accomplishable.

I sincerely thank to Dr. Ritu Vishnoi, MNIT Jaipur for her help and support during my research work.

I am thankful to the Dr. G. B. V. S. Lakshmi, New Delhi and Dr. S. Chand & Dr. Asit Patra, National Physical Laboratory, New Delhi for their fruitful discussion and support during the very initial stage of Ph.D.

I, sincerely thank to the Head, department of Physics for giving me this opportunity to work in this laboratory. I also thank all the Faculty members, Department of Physics, MNIT Jaipur for their suggestions during my research work and their kind support. The characterization facilities provided by Material Research Centre, MNIT Jaipur is also acknowledge.

I am indebted to Dr. Kanjilal, Director, Inter University Accelerator Centre (IUAC), New Delhi for proving me the irradiation and characterization facilities at the center. I am also thankful to Dr. D. K. Avasthi, AMITY University, Noida for his useful discussion.

I would like to express my heartiest thanks to my colleagues, Mr. Shushant Kumar Singh, Mr. Himanshu Sharma, Mr. Veeresh Vishnoi and Pooja Sharma from optical material lab (OML), Department of Physics, MNIT Jaipur for their

support during the Ph.D. work. I acknowledge to my senior Dr. Vikas Sharma and Dr. Udai Bhan Singh, IIT New Delhi for their support.

I am fortunate enough to have many good friends who support me in every aspect throughout my Ph.D. career. I am especially grateful to Ms. Harshita Baswal, Mr. Shashank Soni and Ms. Sumitra Sharma for their continuous moral support, encouragement and all the fun we had in the last four years.

I am forever grateful to my elder sister Mrs. Neha Mishra who motivated and helped for the first step of this journey. Without her initial support, it was impossible to me to reach this stage of career.

From deep of my heart, I am thankful to my parents, Shri. Ramesh Kumar Sharma and Smt. Saroj Sharma, who always encouraged me to pursue my goals and for always being my strength to face every difficulty and challenge in my life. I am also thankful to my elder brother Dr. Vijay Sharma and sister-in-law, Dr. Akanksha Sharma and my sister Mrs. Chhaya Sharma and brother-in-law, Mr. Rohit Sharma.

I also acknowledge one more person, who came in my life during this journey, my husband Dr. Aditya Sharma for his love and support.

I especially acknowledge the Department of Science and Technology, New Delhi, (INSPIRE faculty project, IFA-11PH-01, PI: Dr. Rahul Singhal and young scientist project, SR/FTP/PS-029/2012, PI: Dr. Ritu Vishnoi) and MNIT, Jaipur for providing financial support.

**(Trupti Sharma)**

# ABSTRACT

In the present investigation, the irradiation effect on P3HT and PCBM thin films have been explored. The preparation and characterization of P3HT and PCBM thin films after as well as pre irradiation have been discussed. Thin films were prepared using spin coating method at room temperature with the thickness around 300 nm for P3HT and 100 nm for PCBM material.

These thin films are further explored to irradiation of swift heavy ions (SHI) (90 MeV Ni<sup>7+</sup> and 55 MeV Si<sup>4+</sup>) having different energy & mass and low energy ions (1400 KeV Xe<sup>5+</sup>). The SHI irradiation is concluded in terms of better ordering of P3HT at low fluences. The increased crystallinity along with the bigger crystallite size and conjugation length are also observed which is favoring the higher delocalization of electrons in polymer chains. This increased delocalization of  $\pi$ -bands are associated with enhanced dc conductivity at low fluences. Reduction of bandgap of PCBM is also found at low fluences which is concluded due to 2+2 cycloaddition polymerization reactions initiated by SHI irradiation at low fluences. The structural and morphological properties are also concluded to be dependent on incident ion fluence and energy. High energy deposition during SHI irradiation at higher fluences can deteriorate the material properties for both P3HT and PCBM material. Irradiation with a high mass ion at low energy are shown to destroy the structural properties of P3HT and PCBM concluded by the Raman spectroscopy and UV-visible spectroscopy analysis.





# Contents

<b>Acknowledgements</b>	<b>V</b>
<b>Abstract</b>	<b>VII</b>
<b>Contents</b>	<b>IX</b>
<b>List of Tables</b>	<b>XIII</b>
<b>List of Figures</b>	<b>XV</b>
<b>List of abbreviation</b>	<b>XIX</b>

## 1. Introduction

1.1.Polymers.....	2
1.1.1.    Classification of polymers.....	3
1.1.2.    Properties of polymers.....	5
1.1.3.    Application of polymers.....	8
1.2.Conducting polymers.....	9
1.2.1.    Structure of conducting polymers.....	9
1.2.2.    Poly(3-hexylthiophene) (P3HT).....	10
1.2.3.    Phenyl-C <sub>61</sub> -butyric-acid-methyl-ester (PCBM): A fullerene derivative..	12
1.2.4.    Charge carriers in conducting polymers.....	13
1.2.5.    Conduction mechanism.....	15
1.2.6.    Applications.....	15
1.3.Basic phenomenon of SHI interaction with polymer.....	15
1.3.1.    Nuclear stopping ( $S_n$ ).....	16
1.3.2.    Electronic stopping ( $S_e$ ).....	17
1.3.3.    Range of ions.....	18
1.3.4.    Ion track formation models by SHI irradiation.....	18
1.4.General effects on polymer's properties under SHI irradiation.....	21
1.5.Objective of the present study.....	23

## 2. Literature Review

2.1.Introduction.....	26
2.2.SHI irradiation of conducting/conjugated polymers.....	27
2.3.SHI irradiation of fullerene/fullerene derivatives.....	32
2.4.Summary of some other literature review.....	36
2.5.Motivation of thesis problem.....	39

### **3. Materials and Methods**

3.1.P3HT and PCBM materials.....	42
3.2.Sample preparation technique.....	42
3.3. Ion beam techniques for engineering the properties of materials.....	43
3.3.1.    Swift heavy ion irradiation.....	43
3.3.2.    Low energy ion irradiation.....	46
3.3.3.    Summary of SRIM data of incident ion beams on P3HT and PCBM thin films.....	48
3.4. Sample characterization techniques.....	49
3.4.1.    X-ray diffraction (XRD).....	49
3.4.2.    Fourier transform inferred spectroscopy (FTIR).....	51
3.4.3.    UV-visible absorption spectroscopy.....	53
3.4.4.    Raman spectroscopy.....	56
3.4.5.    Photoluminescence (PL).....	58
3.4.6.    Atomic force microscopy (AFM).....	59
3.4.7.    Contact angle measurement.....	61
3.4.8.    X-ray photoelectron spectroscopy (XPS).....	63
3.4.9.    DC conductivity measurement.....	65

### **4. Investigations on modifications in P3HT thin films with electronic excitation by taking different mass and energy**

4.1.Ion irradiation induced modifications of P3HT by 90 MeV Ni <sup>7+</sup> ion beam.....	68
4.1.1.    Results and discussion.....	68
4.1.1.1. Micro-Raman spectroscopy.....	68
4.1.1.2. Fourier transform infrared (FTIR) spectroscopy.....	74

4.1.1.3. XRD studies.....	75
4.1.1.4. XPS analysis.....	77
4.1.1.5. Optical studies.....	79
4.1.1.6. Surface measurements.....	82
4.1.1.7. DC-conductivity measurement.....	84
4.2.Effect of high energy ions on different properties of P3HT thin films by 55 MeV Si <sup>4+</sup> ion beam.....	88
4.2.1. Results and discussion.....	89
4.2.1.1. Micro-Raman analysis.....	89
4.2.1.2. FTIR studies.....	91
4.2.1.3. HR-XRD analysis.....	93
4.2.1.4. XPS analysis.....	96
4.2.1.5. Optical studies.....	97
4.2.1.6. Surface measurements.....	99
4.2.1.7. Electrical conductivity.....	101
4.3.Study of P3HT thin films under exposure of 1400 KeV Xe <sup>5+</sup> ions.....	104
4.3.1. Results and discussion.....	104
4.3.1.1. Micro-Raman analysis.....	104
4.3.1.2. UV-visible absorption spectroscopy.....	105
4.3.1.3. Surface measurement.....	106
4.4.Summary.....	107

## **5. Investigations on modifications in PCBM thin films with electronic excitation by taking different mass and energy**

5.1.Electronic excitation induced modifications of optical and morphological properties of PCBM thin films under 90 MeV Ni <sup>7+</sup> ion irradiation.....	110
5.1.1. Results and discussion.....	110
5.1.1.1. UV-visible absorption spectroscopy.....	110
5.1.1.2. FTIR spectroscopy.....	113
5.1.1.3. Surface analysis.....	114

5.2. Influence of high energy ion (55 MeV Si <sup>4+</sup> ) irradiation on fullerene derivative (PCBM) thin films.....	116
5.2.1. Results and discussion.....	116
5.2.1.1. UV-visible absorption spectroscopy.....	116
5.2.1.2. FTIR spectroscopy.....	119
5.2.1.3. Micro-Raman analysis.....	121
5.2.1.4. Surface analysis.....	123
5.3. Study of fullerene derivative (PCBM) thin films under exposure of 1400 KeV Xe <sup>5+</sup> ions.....	124
5.3.1. Results and discussion.....	124
5.3.1.1. Micro-Raman analysis.....	125
5.3.1.2. UV-visible absorption spectroscopy.....	126
5.3.1.3. Surface analysis.....	126
5.4. Summary.....	127

## 6. Conclusion and future aspects

6.1. Conclusions.....	130
6.2. Future Scope of this work.....	132

<b>References</b>	<b>133</b>
-------------------	------------

<b>List of publication</b>	<b>153</b>
----------------------------	------------

<b>Bio Data</b>	<b>155</b>
-----------------	------------

# List of Tables

1.1 Some properties of P3HT and PCBM materials.....	11
3.1 Summary of SRIM data.....	48
4.1 Summary of modes of vibration in pristine P3HT thin films at different wavenumbers for 514 nm excitation.....	74
4.2 Summary of FWHM of C=C mode ( $1449\text{ cm}^{-1}$ ) and relative areal intensity ratio of the C-C mode to the C=C mode ( $I_{\text{c-c}}/I_{\text{c=c}}$ ) for pristine and 90 MeV Ni <sup>7+</sup> ion irradiated P3HT thin films at different fluences.....	74
4.3 XRD and XPS analysis of pristine and irradiated P3HT thin films.....	77
4.4 Summary of optical bandgap, RMS roughness and contact angle of pristine and 90 MeV Ni <sup>7+</sup> ion irradiated samples at different fluences.....	82
4.5 Summary of Mott's parameters at room temperature (300 K) for pristine and irradiated thin films.....	88
4.6 Summary of different parameters calculated using HR-XRD spectra for pristine and irradiated thin films of P3HT.....	95
4.7 Summary of different parameters of irradiated P3HT thin films.....	101
4.8 details of calculated Mott's parameters for pristine and 55 MeV Si <sup>4+</sup> ion beam irradiated P3HT thin films.....	104
4.9 Summary of roughness variation of irradiated P3HT thin films.....	107
5.1 Summary of variation in optical bandgap.....	112
5.2 Summary of measured roughness of pristine and irradiated PCBM thin films.....	115
5.3 Summary of variation in the optical bandgap, surface RMS roughness and contact angle of pristine and 55 MeV Si <sup>4+</sup> ion beam irradiated PCBM thin films.....	118



# List of Figures

1.1 Polymer Classification.....	3
1.2 Thermal transition in polymers.....	7
1.3 Stress-strain curve for polymers.....	8
1.4 Molecular structure of P3HT.....	12
1.5 Molecular structure of PCBM.....	13
1.6 Effect of dopant on conductivity of polymers.....	14
1.7 Qualitative curve of the energy loss ( $S_e$ and $S_n$ ) of an ion in the material as a function of the ion energy.....	18
1.8 Radiation-induced reactions in polymer.....	23
3.1 Schematic of spin coating process.....	42
3.2 Spin coating unit used for present deposition.....	43
3.3 Schematic diagram of Pelletron accelerator at IUAC, New Delhi.....	45
3.4 Image of LEBIF facility available at IUAC, New Delhi (a) and electron cyclotron resonance source (b).....	47
3.5 Schematic of diffraction pattern (Bragg's law).....	50
3.6 Conventional layout of XRD instrument.....	51
3.7 Different vibrational modes of a molecule.....	52
3.8 Block diagram of FTIR instrumentation.....	53
3.9 Diagram of electronic energy levels ( $E_0$ represents the ground state and $E^*$ represents the excited state) (a); Energy level diagram for different electronic transition (b).....	54
3.10 Schematic diagram of UV-visible spectroscopy.....	55
3.11 Energy level diagram of Rayleigh scattering, Stokes Raman scattering and anti-Stokes Raman scattering.....	56
3.12 Block diagram of micro-Raman scattering experiment.....	57
3.13 Schematic of Photoluminescence process.....	59
3.14 Block diagram of Atomic force microscopy.....	61
3.15 Illustration of contact angles formed by liquid drop on a smooth homogenous solid surface.....	62

3.16 Schematic representation of the necessary components for XPS.....	64
3.17 Image of R-T measurement setup at IUAC, New Delhi.....	66
4.1 Raman spectrum of pristine P3HT thin film under 514 nm excitation.....	69
4.2 Raman spectra of pristine and 90 MeV Ni <sup>7+</sup> ion beam irradiated thin films of P3HT.....	70
4.3 Variation of FWHM (a), peak height (b) and normalized intensity (c) corresponding to C=C mode (1449 cm <sup>-1</sup> ) and C-C mode (1380 cm <sup>-1</sup> ) with different fluences of 90 MeV Ni <sup>7+</sup> ion beam.....	72
4.4 Represents the variation of relative areal intensity ratio of C-C mode to C=C mode ( $I_{c-c}/I_{c=c}$ ) with different fluences.....	73
4.5 Schematic diagram of radial gradient of temperature around the ion path.....	73
4.6 FTIR spectra of pristine and irradiated P3HT thin films.....	75
4.7 XRD pattern of pristine and irradiated P3HT thin films.....	76
4.8 Typical XPS survey scan of pristine and irradiated P3HT thin films.....	78
4.9 High resolution spectra of C 1s and S 2p of pristine and irradiated P3HT films.....	79
4.10 UV-visible absorption spectra of pristine as well as 90 MeV Ni <sup>7+</sup> ion beam irradiated thin films of P3HT. The inset shows the Tauc plot of pristine and 90 MeV Ni <sup>7+</sup> ion irradiated P3HT thin films.....	80
4.11 (a) PL spectra of pristine and 90 MeV Ni <sup>7+</sup> ion beam irradiated P3HT thin films at room temperature. (b) Normalized PL spectra of P3HT thin films.....	81
4.12 Images of pristine and irradiated P3HT samples.....	82
4.13 Three dimensional AFM micrographs of pristine and 90 MeV Ni <sup>7+</sup> irradiated P3HT thin films at different fluences.....	83
4.14 Contact angle measurement images of pristine and 90 MeV Ni <sup>7+</sup> ion irradiated P3HT films.....	84
4.15 The plot of log of dc conductivity ( $\sigma_{dc}$ ) as a reciprocal of Temperature (1000/T) in the range of 200-400 K for pristine and 90 MeV Ni <sup>7+</sup> ion irradiated P3HT thin films.....	86



4.16 The log of dc conductivity ( $\sigma_{dc}$ ) plotted as a function of reciprocal of Temperature ( $T^{-1/4}$ ) in the range of 200-400 K for pristine as well as 90 MeV $Ni^{7+}$ ion irradiated P3HT thin films.....	86
4.17 Plot of $\log E_A$ versus $\log T$ in the temperature range 200-400 K for pristine and 90 MeV $Ni^{7+}$ ion irradiated P3HT thin films.....	87
4.18 Raman spectrum of Pristine P3HT thin film confirming the presence of all Raman active modes of P3HT.....	90
4.19 Raman spectra of 1380 $cm^{-1}$ and 1448 $cm^{-1}$ vibrational peaks for pristine and irradiated P3HT thin films.....	91
4.20 Variation of FWHM and relative intensity ratio ( $I_{c-c}/I_{c=c}$ ) corresponding to 1448 $cm^{-1}$ peak for pristine and irradiated P3HT films.....	91
4.21 FTIR of as deposited as well as irradiated thin films of P3HT.....	92
4.22 HR-XRD patterns of P3HT thin films for different peaks before and after irradiation with 55 MeV $Si^{4+}$ ion beam.....	94
4.23 Schematic of possible a-axis orientation (main polymer chains are parallel and alkyl side chains are perpendicular to the substrate) of the thiophene crystallites with respect to the substrate.....	95
4.24 High resolution spectra of C 1s and S 2p of pristine and irradiated P3HT films.....	96
4.25 Optical absorption spectra of pristine and irradiated P3HT thin films (a).The bandgap variation with different fluences (b).....	98
4.26 Emission spectra of pristine and irradiated P3HT thin films.....	98
4.27 Three dimensional AFM micrographs of pristine and 55 MeV $Si^{4+}$ ion beam irradiated P3HT thin films.....	99
4.28 Snapshots of contact angle measurement of pristine and irradiated P3HT thin films.....	100
4.29 The plot of dc conductivity ( $\sigma_{dc}$ ) as a function of (a) reciprocal of temperature, $1000/T$ ; (b) $T^{-1/4}$ in the range of 230-350 K and (c) plot of $\log$ activation energy ( $E_A$ ) versus $\log$ temperature (T) of pristine and irradiated P3HT thin films.....	103
4.30 (a) Raman Spectra of pristine and irradiated P3HT thin films. (b) Variation of FWHM with incident fluences corresponding to 1448 $cm^{-1}$ Raman band.....	105

4.31 (a) Absorption spectra of pristine and irradiated P3HT thin films. (b) Tauc plot for determining the bandgap values of pristine and irradiated samples.....	106
4.32 Images of AFM micrographs for pristine and irradiated P3HT thin films.....	107
5.1 UV–visible absorption spectra of pristine and 90 MeV Ni <sup>7+</sup> ion beam irradiated PCBM thin films.....	111
5.2 Variation in optical bandgap of pristine and irradiated PCBM films.....	112
5.3 The measured FTIR spectra of pristine and irradiated PCBM thin films.....	113
5.4 Variation of FTIR peak intensity of pristine and irradiated PCBM thin films.....	114
5.5 Three dimensional AFM micrographs of pristine and irradiated thin films of PCBM.....	115
5.6 UV–visible absorption spectra of pristine and irradiated PCBM thin films. The inset shows the Tauc’s plot of pristine and irradiated thin films at fluences of 1×10 <sup>10</sup> and 1×10 <sup>11</sup> ions/cm <sup>2</sup> .....	117
5.7 (a) Schematic of “2+2 cycloaddition” reaction of adjacent molecules where carbon double bonds faces each other. (b) Schematic of the expected polymerized fullerene molecules.....	118
5.8 The measured FTIR spectra of pristine and irradiated PCBM thin films.....	119
5.9 Normalized areal intensity variation of FTIR peak for pristine and irradiated PCBM thin films.....	120
5.10 Raman spectra of pristine and 55 MeV Si <sup>4+</sup> ion beam irradiated thin films of PCBM.....	121
5.11 Curve between the normalized areal intensity of three Raman modes (1428 cm <sup>-1</sup> , 1462 cm <sup>-1</sup> , 1568 cm <sup>-1</sup> ) with different fluences of 55 MeV Si <sup>4+</sup> ions.....	122
5.12 (a) Two-dimensional (2D) AFM height images and (b) Contact angle images of a water droplet with pristine and ion irradiated PCBM films at the fluences of 1×10 <sup>11</sup> and 1×10 <sup>12</sup> ions/cm <sup>2</sup> .....	124
5.13 Raman Spectra of pristine and irradiated PCBM thin films.....	125
5.14 Absorption spectra of pristine and irradiated PCBM thin films.....	126
5.15 Three dimensional AFM micrographs of pristine and irradiated PCBM thin films.....	127

# List of abbreviations

- HOMO:** Highest Occupied Molecular Orbital
- LUMO:** Lowest Unoccupied Molecular Orbital
- SHI:** Swift Heavy Ion Irradiation
- P3HT:** Poly(3-Hexylthiophene)
- PCBM:** Phenyl-C<sub>61</sub>-butyric-acid-methyl-ester
- OPV:** Organic photovoltaic
- BHJ:** Bulk Heterojunction
- OSC:** Organic Solar Cells
- S<sub>e</sub>:** Electronic energy loss
- S<sub>n</sub>:** Nuclear energy loss
- SRIM:** Stopping and Range of Ions in Matter
- BE:** Binding Energy
- XRD:** X-ray Diffraction
- IR:** Infrared
- AFM:** Atomic Force Microscopy
- PL:** Photoluminescence
- XPS:** X-ray Photoelectron Spectroscopy



# Introduction

## 1.1 Polymers

The materials called “Plastics” have been developed with the beginning of Rayon in 1891 which continued in progress with the development of Bakelite in 1907, when, two chemicals, Formaldehyde and Phenol, reacting at controlled pressure and temperature formed a compound that could be cast into hard, infusible substances. Jacques Brandenburger introduced a famous material which was transparent in appearance in 1912 called cellophane. Hermann Staudinger proposed the linear structure (atoms in a long chain joint together by covalent bonds) for polystyrene and natural rubber and awarded with Noble Prize in Chemistry in 1924. After the concept of the linear structure of macromolecules, various materials such as Cellulose acetate in 1927, polyvinyl Chloride (1929), Polyethylene (1933), Teflon, Nylon and Polystyrene in 1938, and many more were discovered and is still continuing.

The word polymer is a Greek word which means “many-parts.” Polymers are macromolecules with a high molecular weight which composed with repeating units in long chains, built up by linking together of smaller molecules which are called monomers. These monomers are combined with covalent bonds to form a polymer [1]. Polymers have achieved a great importance in research during last few decades. Nowadays, polymeric materials are used in nearly all areas of daily life. Polymers are replacing metals and ceramics in many areas as it have outstanding properties such as low cost, easy processibility, light weight, durability, high corrosion resistance, high electric resistance, etc. In last few decades, many researchers and scientific laboratories have reported on polymers with better properties such as rigidity, strength, toughness, resistance and dimensional stability etc., which make them more promising than conventional materials as metals, alloys etc. The polymers with superior properties are also using in space, nuclear technology, sensor application and medical sciences etc. Nowadays, several types of conducting polymer are developing along with the newer processing techniques.

### **Some common characteristics of polymers:**

- Low density
- Low friction coefficient
- Good corrosion resistance

- Economical
- Good moldability
- Excellent surface finish can be obtained
- Poor tensile strength
- Low mechanical properties
- Poor temperature resistance
- Can be produced transparent or in different colors

### 1.1. 1 Classifications of polymer

In general, the orientation of the polymer chains and the linked monomer units composing polymer chains are responsible for the overall physical and mechanical properties of any polymer. As the polymers consist the various type and numbers of atoms in their molecules, they have a different type of chemical structure, mechanical behavior, thermal properties, physical properties etc. So the classification of polymers based on their different properties can be summarized as in **Figure 1.1** and a brief description is also given below.

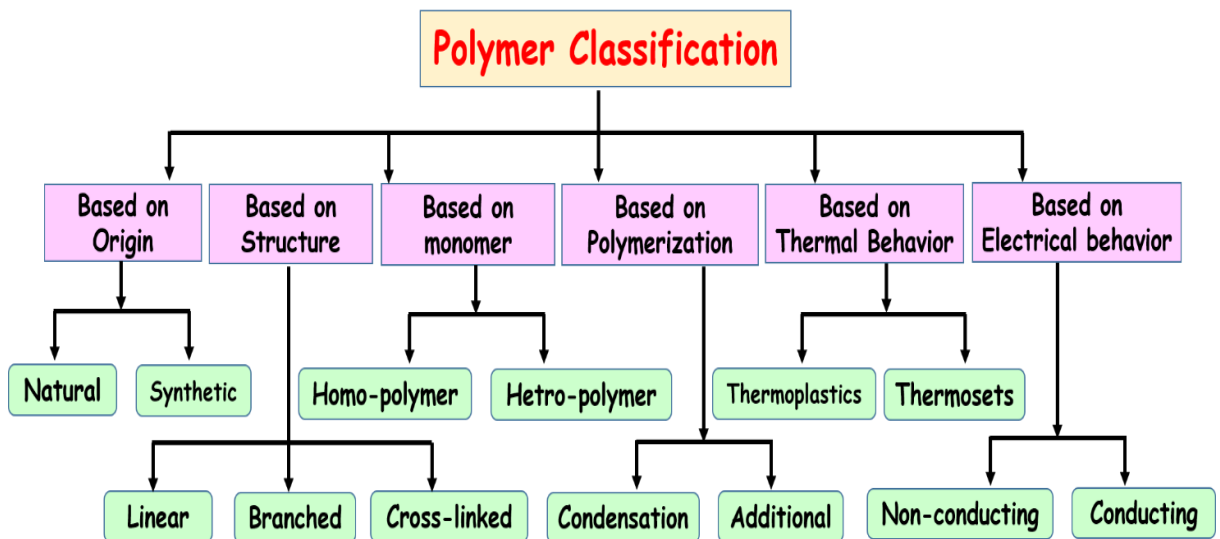


**Figure 1.1:** Polymer classification

**Based on origin [2]:**

a) *Natural Polymers*:- These type of polymers occur in nature. In more general terms, examples of these polymers are starches, cellulose, amino acids, proteins, natural rubber, natural silk etc.

b) *Synthetic Polymers*:- This type of polymers are synthesized in laboratories for the specified tasks or aim such as paper films, pipes, food packing etc. Examples of monomers in the synthesis of such polymers are polyvinyl alcohol, polyethylene, polystyrene, polysulfone, etc.

#### **Based on structure:**

a) *Linear Polymer*: - These type of polymers having the monomers which are linked in a long chain in a linear manner. This chain is called the backbone and usually made of hundreds of thousands of atom to be linked. These type of polymers have no side chains, high density, and tensile strength and closely packed.

b) *Branched Polymer*: - The polymers having the different side chains joined in a branched manner are called branched polymer. The side chains are extending from the backbone. As the monomers in this type of polymers are joined irregularly hence, they have low density, low tensile strength and low melting temperature. For example, glycogen and polypropylene are branched polymers.

c) *Cross-linked Polymer*: - These polymer having the network of linear chains joined covalently. Two chains bonded to a third common molecule or bonds between the neighboring chains can made cross-linked polymers. These polymers are hard, brittle and rigid due to the cross-linked structure. Polymers with memory have high degree of cross-linking; they do not dissolve in solvents. For example vulcanized rubber, Bakelite and melamine.

*Cross-linked polymers do not have the properties to be reprocessed in another shape upon heating, called thermosets. But linear and branched polymers thermoplastics.*

#### **Based on monomer used:**

a) *Homo-polymers*:- These polymers have a single type of repeating units or monomers. For example, Polyethylene composed of ethylene monomers.

b) *Hetro-polymer*: - Polymers in this class are made up of two type of monomers. These are also called copolymers. Polyvinyl Chloride (PVC) is the example of copolymers.



**Based on polymerization [2]:**

a) *Condensation Polymer*: - This type of polymers are formed with two type of monomers having different groups of atoms with the removal of small molecules such as water ( $H_2O$ ). Polyesters and polyamides are examples of this type of polymers.

b) *Additional Polymer*:- The additional polymers are formed by adding the monomers repeatedly possessing double or triple bonds. In these type of polymers, there is no loss of small molecules. For example polythene.

**Based on thermal behavior [3]:**

a) *Thermoplastic Polymers*:- These polymers can be softened while, heating and hardened when, cooling at room temperature without large changes in their properties. This polymer can be linear, branched and can be recycled much time. Examples are polythene, PVC.

b) *Thermoset Polymers*:- These polymers are hard and not remolded. Upon heating, they undergo some chemical changes and convert into infusible. These type of polymers are cross-linked or branched and they cannot reuse or recycled. Resins, urea, Bakelite etc. are the examples of these polymers.

**Based on electrical behavior [4]:**

a) *Non-conducting Polymers*:- The polymers having chemically saturated structures consisting tightly bound electrons in the  $\sigma$ -bonds between atoms. Therefore, there are no electrons free to carry an electric current because all electrons are fixed in the  $\sigma$ -bonds. Hence, saturated polymers are characteristically electrical insulators.

b) *Conducting Polymers*:- The polymer main chain having conjugated molecular structure and delocalized with  $\pi$ -electrons. The difference between the top of the valence band, HOMO and the bottom of the conduction band, LUMO is called the bandgap ( $E_g$ ) of the conjugated polymers. The  $E_g$  values of most conjugated polymers are in the range 1.5–3.0 eV.

**1.1.2 Properties of polymers [5][6][7]**

The physical, thermal and mechanical properties of polymers are briefly described in the following section:

**Physical properties:**

The physical properties basically include the length of chains, molecular weight, crystallinity of material, density, molar volume, the degree of polymerization and so on. Among all of these, the crystallinity of polymer has discussed here because most of the polymers are composed of crystalline and amorphous regions.

a) *Crystalline nature:* Crystallinity can define as an ordered arrangement of molecules in a regular manner in any material. Ideally, no polymer is completely crystalline, so the term “semi-crystalline” is more appropriate for polymers. There is only some region in polymers where molecules are parallel aligned to one another and separated by disordered regions where molecules are randomly aligned. The crystallization of polymer improves the strength, stiffness and high melting point properties rather than the amorphous polymers. The example of a crystalline polymer is polyethylene.

b) *Amorphous nature:* These type of polymer adopt the random arrangement of molecules in a material. These polymers are soft and have a low melting point than crystalline one. These polymers will not return in the previous length when, they are stretched because individual molecule starts to slip past one another. Polystyrene is the example of an amorphous polymer.

**Thermal properties:**

At low temperature, the molecules of the amorphous region of the polymer are in the frozen state, i.e., molecules can vibrate slightly but cannot move significantly. This state is called *glassy state*. When, the temperature is giving to any polymer, the chain can move which make polymers soft and flexible as rubber. This state of the polymer is called *rubbery state*. Polymeric materials have two types of transition temperatures (**Figure 1.2**).

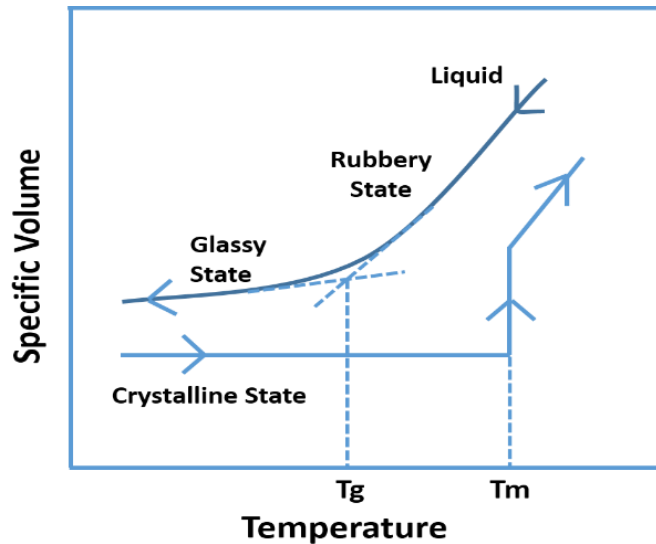


**Figure 1.2:** Thermal transition of polymers

*Glass transition temperature ( $T_g$ )* at which glassy state (hard, rigid) of polymers makes a transition to rubbery state (soft). This type of transitions can only occur in amorphous regions.

*Crystalline melting temperature ( $T_m$ )* is the melting temperature of crystalline regions of polymeric material at which ordered region turns into the disordered region. If a polymer contained double bonds, large side groups and attached aromatic group, they have high melting temperature because they limit the chain flexibility.

*It should be mentioned here that amorphous polymers do not possess melting point ( $T_m$ ), but all polymers possess the glass transition temperature ( $T_g$ ).*

### **Mechanical properties:**

The mechanical properties of any polymer can be specified by the parameters such as strength, tensile modulus, ultimate elongation, toughness, etc. The mechanical behavior can easily describe using stress-strain curve (**Figure 1.3**). These properties depend on temperature and can change from brittle glass-like behavior to rubber-like soft behavior with temperature change.

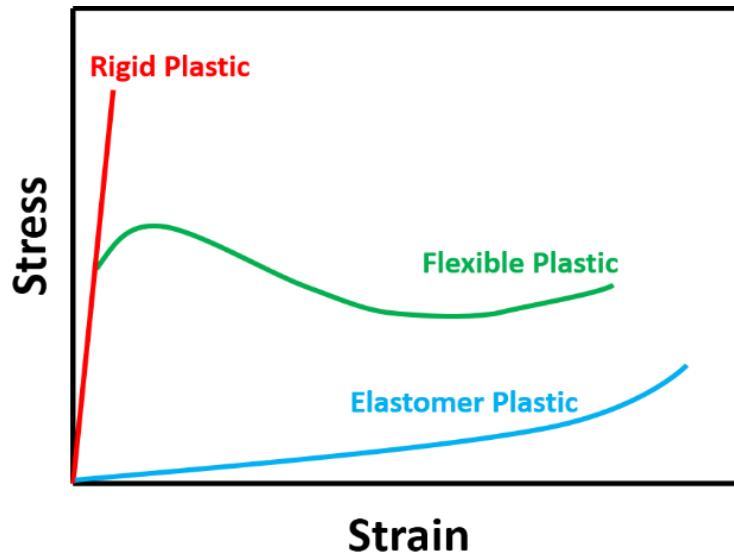


**Figure 1.3:** Stress-strain curve for polymers

### 1.1.3 Application of polymers

Nowadays, the polymers are playing a prominent role in everyday life. Because of their exceptional properties like low density, durability, transparency, thermal and electrical resistance, etc., polymers are widely used in many industrial applications. Some of the major applications are listed below:

- Polymers are used in soil as it provides mulch, it promotes plant growth and health.
- Plastic containers are light weight and cost effective. Polymers are also being used in clothing, floor coverings, garbage disposal bags, shampoos, engine oils, super absorbent diapers and packing.
- Polymers are also used in sports industry such as in equipment for the playground, various type of balls, golf sets, swimming pool, protective helmets, etc.
- Prosthetic components like heart valves and blood vessels are being made from polymers like Dacron, Teflon, etc. Dissolvable sutures, implants, drug delivery systems are also made from polymers.
- Automobile parts, pipes, packing material, insulation, wind shields for fighter planes, wood substitutes, sterilized bottles, tanks, TV cabinets, toys, garden equipment, adhesives, etc. are also typical areas for polymer applications.

- Polymers are also used in windows, optical fibers, films packages, lenses, drafting equipment, reflectors, etc. because of their outstanding light transmission and reflection properties.

## **1.2 Conducting polymers**

Traditional polymers like rubbers, plastics, etc. were supposed to be resistant to electrical conduction and most commonly used as insulators or dielectrics. The invention of electrically conducting polyacetylene, in 1977 by Alan J. Heeger, Alan G. MacDiarmid and Hideki Shirakawa [8], is a turning point in the field of electrical conduction. This pioneering discovery and development [9][10][11] of electrically conducting polymers was awarded Nobel Prize in Chemistry in 2000. The discovery of electrical conductivity in polymeric materials [12][13][14][15] has provided the future impetus for the growth of polymer-based electronic devices. These conducting polymers possess many chemical advantages such as ion transport possible, catalytic behavior, redox behavior, junction effect, photo activity, electrochemical effects along with the mechanical properties like light weight, non-metallic, flexible, surface properties, etc. The conduction properties [16][17][18], electroluminescence, optical and many other physical properties [19][20][21][22] of conducting polymers have investigated earlier. In last few years, the understandings of the relationship between structure and material's properties have also been developed for many conducting polymers [23][24][25]. These conducting polymers having importance in emerging technological applications such as chemical sensors [26], non-linear optics [27], molecular electronics [28], electrochromic displays [29], actuators [30][31] etc.

### **1.2.1 Structure of conducting polymer**

Conducting polymer are different because of their conjugation structure, i.e., carbon atoms have alternate single and double bonds in the polymer backbone chain. The positions of these single and double bonds can be changed with no or slight energy difference. The backbone of conducting polymers contains the  $\sigma$ -bonds between carbon atoms which are  $sp^2$  hybridized resulting every carbon atom has one unpaired electron ( $\pi$ -electron). The  $\pi$ -

electrons leads to the electron delocalization along the polymer backbone. This delocalization along the polymer backbone allows the charge carriers to move.

*Conducting polymers contains alternated single-double bonds or single-triple bonds within their main chain. These polymers are also described by sigma ( $\sigma$ ) bonds and pi ( $\pi$ ) bonds. The  $\sigma$  bonds are immobile and fixed because they form covalent bonds between the carbon atoms while, the  $\pi$  electrons can easily delocalize upon doping. The doping process makes them capable of conducting electricity. Polyacetylene (PA), polythiophene (PT), Polyaniline (PAni), Poly(*p*-phenylene vinylene) (PPV), polypyrrole (PPY), etc., are the examples of this type of polymers. The doping process is most widely used to make polymers conducting, i.e., some extra electrons or holes are injected into the material which acts as charge carriers. The doping mechanism into polymeric materials led to significant increase in the conductivity of conjugated polymers. However, the conjugated structure is not enough to make the polymers conductive.*

### **1.2.2 Poly (3-Hexylthiophene) (P3HT)**

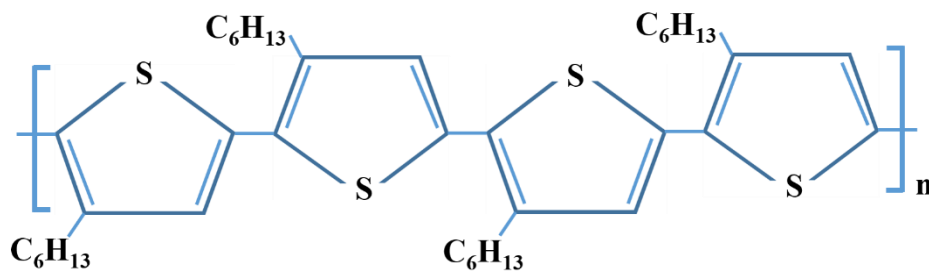
P3HT is a widely used semiconductor in the research field on conjugated polymers with the advance in synthetic methodology. Based upon semiconducting properties, P3HT is used in different organic electronic devices such as organic light emitting diodes (OLED), organic field effect transistors (OFET), organic solar cells (OSC) and much more. The synthesis of P3HT is easy and having good optoelectronic properties. Therefore, various fundamental studies such as film morphology, charge transport, absorption and emission, etc. have been done [32][33][34][35].

Thiophene is an aromatic, heterocyclic compound. This compound also has a non-carbon element which is *sulfur*. It (sulfur) forms a node of a ring containing alternating single and double bonds with four atoms of carbon. The electrons in the plane of carbon nuclei form the single bonds by sigma bonding. An overlapping of p-orbitals above and below the plane of the ring formed a sigma bond and a  $\pi$ -bond which formed double bonds. These orbitals are free to move and interact as they want because they are out of the plane of the nuclei, and hence become delocalized. The lone pairs on the sulfur atom along with the electrons in the  $\pi$ -bonds also participate in high charge mobility of thiophene and responsible for its semiconducting properties. This kind of system is called conjugated

system, i.e., *the single and double bonds delocalize the  $\pi$  electrons to lower the overall energy of the molecule and increase stability.* **Figure 1.4** is showing a P3HT molecule. P3HT, a semiconducting polymer, consisting of a  $\pi$ -conjugated backbone with polythiophene units and pendent alkyl side group which provides high solubility in organic solvents. Polythiophenes are having a combination of different coupling those are referred as regio-random or regio-regular. If the polymer has non-uniform substituent distribution, unfavorable Head to Head (HH) coupling will be there and result the twisting of the thiophene units away from the planarity. This leads to a decrease in the conjugation length. In contrast, regio-regular polythiophenes having a uniform distribution of substituents contain Head to Tail (HT) coupling exclusively. They can acquire a planar conformation with low energy and extended  $\pi$ -conjugation. This regio-regularity leads to better properties such as high absorption in the visible range and effective charge transport for device applications. In the crystalline structure of P3HT, the chains are aligned and stacked on top of each other with the thiophene rings forming a planar alternating ‘up-down’ conformation, and the alkyl side chains are perpendicular to the stacking direction [36]. The crystallinity of P3HT depends on many factors like average molecular weight, regioregularity, etc. and their electronic bandgap lies within the visible region of the electromagnetic spectrum. P3HT has the bandgap about 1.9 eV and mobility is about 0.1  $\text{cm}^2/\text{Vs}$  and is a good electron donor material that effectively transports positive holes.

**Table 1.1:** Some properties of P3HT and PCBM materials.

<b>Properties</b>	<b>P3HT</b>	<b>PCBM</b>
Composition	$(\text{C}_{10}\text{H}_{14}\text{S})_n$	$\text{C}_{72}\text{H}_{14}\text{O}_2$
Density	1.1 $\text{g}/\text{cm}^3$	1.5 $\text{g}/\text{cm}^3$
Glass transition temperature	12 $^\circ\text{C}$	118.3 $^\circ\text{C}$
Melting temperature	178 $^\circ\text{C}$	279.5 $^\circ\text{C}$



**Poly (3-Hexylthiophene) (P3HT)**

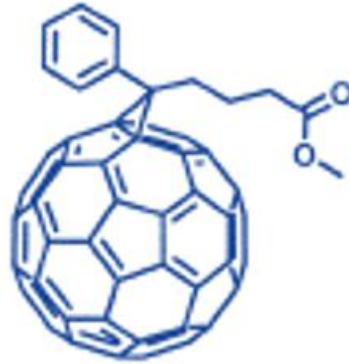
**Figure 1.4:** Molecular structure of P3HT

### 1.2.3 Phenyl-C<sub>61</sub>-butyric-acid-methyl-ester (PCBM): A fullerene derivative

Fullerene derivatives such as PC<sub>61</sub>BM [37] (as shown in **Figure 1.5**) have exhibited increasing commercial usage in organic field effect transistors [38] and organic solar cells (OSCs) [39][40], memory applications [41], fluorescence spectroscopy measurement of fullerenes [42] etc. as they have deep-lying LUMO levels and n-type organic semiconducting nature. PC<sub>61</sub>BM has a phenyl-butyric-acid-methyl-ester side tail attached to the C<sub>60</sub> cage. The enhanced solubility of fullerene in organic solvents such as chloroform, chlorobenzene and dichlorobenzene, etc. than C<sub>60</sub> molecules is due to side tail. Enhanced solubility leads to low-cost and easy manufacturing processes such as spin coating. Then the interactions determining the molecular packing become more complicated as compared with the case of C<sub>60</sub> on the metal surface. Previously, Rispen et al. have reported that the solvent choice is very important for the PCBM crystallization behavior [43]. In particular, when, PCBM films are casting from chlorobenzene (CB) leads to the formation of reddish triangle-shaped crystals with a triclinic unit cell ( $a = 13.83$ ,  $b = 15.29$ ,  $c = 19.25$  Å,  $\alpha = 80.3^\circ$ ,  $\beta = 78.6^\circ$ , and  $\gamma = 80.41^\circ$ ) whereas, drop casted from ortho-dichlorobenzene (oDCB), it form red-brown platelet-shaped crystals with a monoclinic unit cell ( $a = 13.76$ ,  $b = 16.63$ ,  $c = 19.08$  Å, and  $\beta = 105.3^\circ$ ) [43]. Various modeling studies for charge transport features and the structure-property relationship in PCBM have been carried out by other groups also [44][45]. This derivative of buckminsterfullerene (C<sub>60</sub>) is soluble and good electron acceptor materials used in solution-processed OSCs. It effectively transports electrons from molecule to molecule as well because of their higher electron mobility, high thermal stability and higher electron affinity. High symmetry of



PCBM molecules is advantageous as it leads to a better mixing/contact with neighboring molecules. The mobility of PCBM molecules lies between  $2 \times 10^{-3}$  and  $2 \times 10^{-2}$   $\text{cm}^2/\text{vs}$ .



### **Phenyl-C<sub>61</sub>-butyric-acid-methyl-ester (PCBM)**

**Figure 1.5:** Molecular structure of PCBM

#### **1.2.4 Charge carriers in conducting polymer**

A band-like electronic structure can be formed by a continuous system of strongly interacting atomic orbitals. In conjugated polymers, the origin of the band structure is the interaction of the p orbitals of repeating units along the complete chain. The molecular orbitals (bonding and anti-bonding) is formed by the association of two or more adjacent p-orbitals in which the pairs of the electron are allocated by more than two atoms which resulting in a delocalized  $\pi$ - band. The bonding  $\pi$ -orbitals introduces the HOMO and anti-bonding  $\pi$ -orbital is referred to as LUMO [46]. These HOMO and LUMO orbitals can assume to be analogous to valance and conduction bands of solid-state materials. The doping process in conjugated polymers is directly relevant to its increased conductivity. Upon doing, the formation of self-localized excitations like polarons, bipolarons and solitons happens as shown in **Figure 1.6**. Thus, in conjugated polymers, the charge carriers are not free electrons and holes, but they are quasi-particles such as polaron, bipolaron and solitons. These quasi-particles can also move relatively free throughout the material.

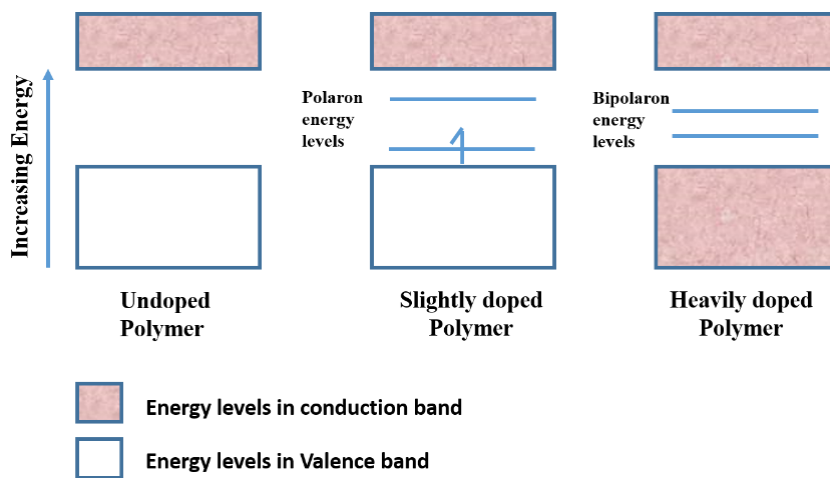


**Figure 1.6:** Effect of dopant on conductivity of polymers

If conjugated polymers having non-degenerate ground state structure and electron is ejected from the  $\pi$ - system by oxidation, an unpaired electron with spin  $\frac{1}{2}$  (a free radical) and a positive charge (spin less) called cation are created. The radicals and cation are combined with each other via a local bond rearrangement and generate a polaron [47][48]. If the oxidation process continues, this creates dication in the polymer. During this process, an electron can be ejected from either the polaron or neutral part remained in the polymer. If an electron is ejected from the polaron, then it lost its free radical nature and formed a dication which made up of two positive charges conjoin through the lattice distortion. This creates the bipolaron which are spinless defects [49]. While, if an additional electron is ejected from the neutral part of the polymer chain, it would produce two polarons, which, is energetically favorable. Because the larger decrease in ionization energy will produce when, bipolaron forms as compared to the formation of two polarons. For example polyacetylene, poly-pyrrole, polythiophene, poly (p-phenylene) are non-degenerate conjugated polymers.

When, the conjugated polymers have degenerate ground state structure, they will create defects called solitons upon oxidation. These solitons are isolated, non-interacting charged defects and generates a new localized electronic states. These energy states are situated in the middle of the energy gap. These states are overlapping with increasing doping to form soliton bands [50]. The example of a degenerate conjugated polymer is trans-polyacetylene.

### 1.2.5 Conduction mechanism

Most generally two types of conduction process are essential in conducting polymers. They are as follows:

- a) *Intra chain mobility*:- In this type of process, the charge transport is along with the polymer chain. This kind of transport may be possible because of the formation of polarons and solitons which are localized but mobile excitations.
- b) *Inter chain mobility*:- When, the charge transport is between the chains, it is called inter chain mobility. This type of transport may be due to the inter soliton hopping because these charges are delocalized and mobile on the polymer chains. Thus, these are current carrying for the conduction mechanism. During conduction, these species must hop from chain to chain and along the chain.

### 1.2.6 Applications

The electrical and optical properties of the polymer consisting extended  $\pi$ -orbitals can be controlled using oxidation and reduction. Therefore, Conducting polymers exhibit a wide range of tunable properties that make them ideal for use in devices. Following are some important applications in which conducting polymers are widely used.

- Polymeric Batteries
- Electro chromic Displays (ECD)
- Light Emitting Diodes (LED)
- Sensors
- Drug release systems and artificial nerves
- Electromechanical Actuators
- Antistatic coating in aircraft structures,
- Electromagnetic shielding of computers
- Conducting fabrics
- Organic field effect transistors
- Organic solar cells

## 1.3 Basic phenomenon of SHI interaction with polymer

Nowadays, the use of energetic ions for modification of the material's property has attracted great attention. SHI is a unique tool for material modification which is not possible by conventional radiations. The main advantage of using ion beam is the limited depth of penetration, which allows for the efficient use of energy for material modifications. Ion beams also provide the surface alteration/modifications without changing the properties of underlying materials. The modification of the structures and phases of polymeric materials using energetic ions has also attracted great attention of researchers [51][52][53][54][55][56][57] in recent years. Increasing use of polymers in space crafts, sterilization, nuclear power plants, high energy particle acceleration, shielding materials in satellites for thermal control, etc. encounters harsh radiation environments [58][59][60]. The high-density ionization induced by the energetic ions has been found to modify the molecular structure and macroscopic properties of the polymer. Such modifications depend on the incident ion parameters and target materials. It is, therefore, necessary to understand the ion beam induced alteration/ modification of material. To understand the, to the matter. When, an ion having high energy passes through the polymeric material, it loses its energy mainly through four processes.

1. Nuclear stopping (nuclear energy loss) " $S_n$ "
2. Electronic stopping (electronic energy loss) " $S_e$ "
3. Phonon decay
4. Plasmon decay

The former two processes (**Figure 1.7**) are most significantly responsible for changing the material properties and the latter two processes consist mainly of thermal energy losses through thermal vibrations of atoms and electrons. The energy loss by phonon happens from the recoil of atoms and its magnitude of loss will increase when, the mass of ion increases. Plasmon decay is essentially negligible.

**1.3.1. Nuclear Stopping ( $S_n$ ):** In this process, when, energetic ions incident on the target material, it transfers energy by elastic collisions between the incident ion and target nuclei. When, the colliding particle transfers energy larger than displacement threshold energy to target atom, displacement of atoms occur [51]. This threshold energy is the amount of energy which required by a recoil atom to overcome the binding forces and to move a

distance more than the atomic spacing away from its original site. If the imparted energy is less than the threshold energy, then the energy of knock-on atoms vanishes as atomic vibrations which are called phonons and these atoms cannot escape their site.

The nuclear collisions occur between the two atoms having electrons around their nuclei. Therefore, the interaction mechanism of the nucleus of the target material with the incident ions is considered as two screened particles. To derive the nuclear energy loss, it is assumed that the momentum is transferred from the incident ion to the target material and the inter-atomic potential between them is also considered. Therefore, the incident ion velocity and charges of two colliding atoms are the two parameters on which nuclear stopping depends. If the velocity of ions slows down and comes around the Bohr velocity, then nuclear stopping plays a major role. Therefore, at the end of the ion track, maximum nuclear energy loss happens. For nuclear stopping, the distribution of the energy transferred to the material by the energetic particle per unit distance, called the energy loss, has a maximum around 1 KeV/amu and extends to around 100 KeV/amu, i.e., predominates at lower energies [61].

**1.3.2. Electronic Stopping ( $S_e$ ):** In this process, the electromagnetic interaction between the electrons and incident ions (positively charged) of the material leads to the energy loss mechanism. The electronic stopping can be explained by following two mechanisms [51]:

- a) Glancing collision- Inelastic scattering, small momentum transfer and distant resonant collisions
- b) Knock-on collision- Elastic scattering, large momentum transfer and close collision

The energy is transferred by the ionization and electronic excitation in both knock-on and glancing collisions. When, an orbital electron is raised to a higher energy level called electronic excitation and when, an electron of the orbital is ejected from the atom, is called ionization. It is reported theoretically and experimentally that glancing collisions and knock-on collisions contribute equally to the electronic energy loss mechanism [62][63]. The energy rationing between the different loss processes can be simulated by Monte Carlo simulation program “Stopping and Range of Ions in Matter (SRIM)” [63].

**1.3.3. Range of ions:** The projected ion range is the distance from the target surface over which an ion dissipates its energy completely via elastic and inelastic collisions. The rate of energy loss  $(dE/dx)_{total}$  along the ion trajectory explained the range of an ion in a solid and can be expressed as:

$$R = \int_{E_0}^0 \frac{1}{|dE/dx|_{total}} dE \quad (1.1)$$

Where R denotes the range of an ion having energy  $E_0$ . The most important parameters on which range of an ion depends are the energy  $E_0$ , the atomic number of incident ion ( $Z_1$ ) and the atomic number of the target material ( $Z_2$ ). The range of an ion along the path can be described by the total distance traveled by the ion along the ion trajectory.

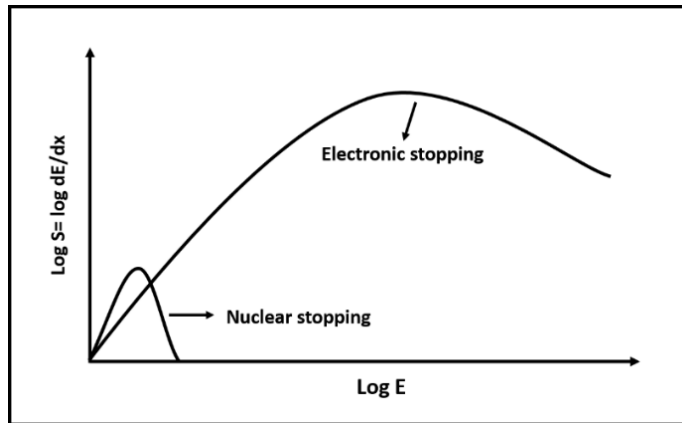


**Figure 1.7:** Qualitative curve of the energy loss ( $S_e$  and  $S_n$ ) of an ion in the material as a function of the ion energy.

The collision between projectile ions and target atoms are random. Therefore the energy loss mechanism is statistical. The penetration of ion into the solid can be explained by two type of straggling: longitudinal straggling and lateral straggling. All the ions penetrating the target do not travel to the similar penetration depth, but they have distribution along the ion path called longitudinal straggling. Each collision between the incident ion and target atoms leads to the deviation from the straight-line path of ions to a lateral direction called lateral straggling.

#### 1.3.4. Ion track formation models by SHI irradiation

When, energetic ions interact with the target material, it deposits large electronic energy along the ion trajectory. This deposited high energy leads to the formation of damage zones in the material. These damaged zones consist the modified/disordered material across the trajectory of ions are known as latent tracks. The formation of latent tracks can be explain using two different mechanisms named as Coulomb explosion model and Thermal spike model.

**(a) Coulomb Explosion Model:**

Fleischer et al. [64] have proposed the track formation model in insulators. According to this model when, an energetic ion travels in insulating material, it creates a highly ionized cylindrical zone across the path of incident ion. A repulsive electrostatic force act during the span of time before which the charge neutrality is reestablished which leads to an explosion. If the neutralization of charge is greater than  $10^{-14}$  s, only then this coulomb explosion phenomenon occurs [65]. This mechanism results in the localized damage in the lattice within the cylindrical zone. Coulomb explosion model explains the condition that the coulomb repulsive forces within the ionized region are sufficient to overcome the lattice bonding forces in terms of a local electrostatic stress being greater than the local bonding strength. If two ions in a material have charge ‘ne’, then the force (F) between those charges can be described as:

$$F = \frac{n^2 e^2}{\epsilon a_0^2} \quad (1.2)$$

Where ‘ $\epsilon$ ’ is the dielectric constant of the material, ‘ $a_0$ ’ is the average atomic spacing. Therefore, the electrostatic stress ‘ $\sigma_e$ ’ or local force per unit area can be expressed as [64]:

$$\sigma_e = \frac{n^2 e^2}{\epsilon a_0^4} \quad (1.3)$$

When, the inter atomic force are relating regarding macroscopically measurable quantities, the mechanical tensile strength ‘ $\sigma_M$ ’ of the material of Young’s modulus (E) is approximately E/10. So the condition for coulomb explosion to occur is ‘ $\sigma_e > \sigma_M$ ’ i.e.

$$\frac{n^2 e^2}{\epsilon a_0^4} > \frac{E}{10} \quad (1.4)$$

The above equation clearly explains that the materials with low mechanical strength, small inter-atomic spacing and low dielectric constant are more feasible for track formation.

**(b) Thermal Spike Model:**

The thermal spike model describe that how a high energy ion can create a region of intense heating in the lattice. This model is two-step thermodynamic process and the target material is considered as a two-component medium. First, the electrons, those are explained using the gas theory of quasi-free electrons and second, the atomic lattice whose thermal properties are known. Initially, the energy of projectile ions is imparted to the electron gas which leads to the transfer of energy to the lattice. This energy transformation occurs via electron-phonon coupling during the specific time  $10^{-13}$  s [66]. The local polarization mechanism is the origin of interaction phenomenon between electrons and phonons. It is supposed that when, the lattice temperature goes beyond the melting temperature of the target material, a transient molten state is produced in a localized zone which is in nanometers scale. This molten state is existing for a short span of time, i.e., picosecond time scale. An amorphous track is formed along the incident ion path by the swift thermal quenching across the cylindrical region. This process occurs for the very short duration of time ( $t \geq 10^{-11}$  s). This amorphous track typically has a diameter of few nanometers. A modified material is observed along the cylindrical region which was transiently heated to high temperature and then quenched rapidly by thermal conduction.

The energy exchange ' $U_{e-ph}$ ' between the electron and phonons at a radius  $r$  from the ion path is given by:

$$U_{e-ph} = g (T_e - T) \quad (1.5)$$

Where ' $g$ ' indicates the constant of electron-phonon coupling, ' $T_e$ ' is temperature for the electronic system and ' $T$ ' is the temperature of the atomic system. The ' $g$ ' factor depends on the thermal conductivity ' $K$ ,' velocity of sound ' $s$ ' and the temperature ' $T$ ' of the atomic system as per the following relation [67].

$$g = \pi^4 \frac{(K_B n_e s)^2}{18KT} \quad (1.6)$$



Since, the electronic and atomic systems are not in thermal equilibrium with each other, space and time evolution of the electronic and atomic system, are regulated by a coupled non-linear differential equations in cylindrical geometry [68] as follows:

$$\rho C_e(T_e) \frac{dT_e}{dt} = \frac{d}{dr} \left[ K_e(T_e) \frac{dT_e}{dr} \right] + \frac{K_e T_e}{r} \frac{dT_e}{dr} - g(T_e - T) + A(r) \quad (1.7)$$

$$\rho C(T) \frac{dT}{dt} = \frac{d}{dr} \left[ K(T) \frac{dT}{dr} \right] + \frac{K(T)}{r} \frac{dT}{dr} - g(T_e - T) \quad (1.8)$$

Where ‘C’ and ‘C<sub>e</sub>’ are specific heats for the atomic and electronic systems, respectively. ‘K’ and ‘K<sub>e</sub>’ are the thermal conductivities for the atomic and electronic systems, respectively. ‘ρ’ represents the material’s density, ‘A(r)’ is the deposited energy in the electronic system within the time duration of ~10<sup>-17</sup> s and ‘r’ represents the radius of the cylindrical region where the path of heavy ion is assumed as the axis.

It is experimentally observed that [69] if the deposited energy is greater than a threshold value (S<sub>e</sub>) then only continuous tracks across the incident ion path are formed. The thermal spike equations show that the value of S<sub>e</sub> depends on the physical properties of the target material. The track diameters of two different ions can be different if they have same S<sub>e</sub> but different velocity [69]. The track diameter will be greater when, ions are slower moving.

#### 1.4. General effects on polymer’s properties under SHI irradiation

The passage of high energy ions through polymers initiate several cascade of processes and dissipation of initial energy occur in form of thermal energy or chemical reactions. The extent of reaction depends upon the nature of the polymer, irradiation conditions and post-irradiation conditions. Under irradiation, the energy is transferred to the medium in ionizations and excitations. Having absorbed energy, polymers suffer bond cleavages, giving rise to non-saturated fragments called "free radicals" and responsible for most of the chemical reactions observed in polymers [70]. **Figure 1.8** illustrates various functional chemical entities created by irradiation [71]. The following major modifications/process are also observed in polymers as a result of irradiation to heavy ions:

- Cross-linking
- Chain scission

- Gas liberation
- Changes in the molecular weight
- Color centers

**Cross-linking:**

Cross-linking is describe by the formation of lateral chemical bonds between different polymer chains. When, radical pairs on neighboring chains or two free dangling ion connect, cross-linking occurs. The mechanism of cross-linking improves the optical density and electrical conductivities because of the formation of conjugated double and triple bonds and increased cross-links by irradiation [51]. This phenomenon also improves the scratch and wear resistance as well as increase hardness and slow diffusion. The solubility of chemical solvents decreases due to cross-linking.

**Chain scission:**

When, a carbon of the main chain is adjoining by four atoms, chain scission becomes significant. The isotrope distribution of the excitation involves enough energy to break all bonds. The presence of bulky side groups, in particular, inhibits the restoration of main chain scissions. The scissoring of chains may cause breakage of bonds, decreases mechanical strength and dissolution of polymers in different solvents can also enhance.

Generally during the irradiation of any material, scission processes and cross-linking can occur simultaneously. Even so, it is noticed that one process tends to dominate the other process.

**Gas Liberation:**

When, high energy radiation incident on polymers, some reactions will be induced and create some gaseous molecules like  $H_2$  and  $CO_2$  with lower molecular weight. These gaseous molecules may create from the primary cleavage of bonds from a main chain or side chains.

**Change in the molecular weight:**

The molecular weight of polymers can increase by cross-linking process induced by heavy ion irradiation. With the increase in the incident fluence, a three-dimensional network is formed between the chains and the polymer becomes a large molecule. Besides this, the chain scission process results in the decrement in molecular weight with increase the incident fluence.

### Color Centers:

In conjugated polymers, the delocalized  $\pi$ -electrons are bound loosely. Using the energy of visible light, these delocalized electrons can be excited which is followed by the absorption of light and leads to change in color. The defects produced by the radiation such as cation, anion and radicals form a broadened band in the bandgap which also contributes to the absorption of light as well. Color changes of irradiated polymers can be used in commercial applications. For example in the medical field, when, the material appearance is of importance when, optical properties must keep same in high radiation surroundings.

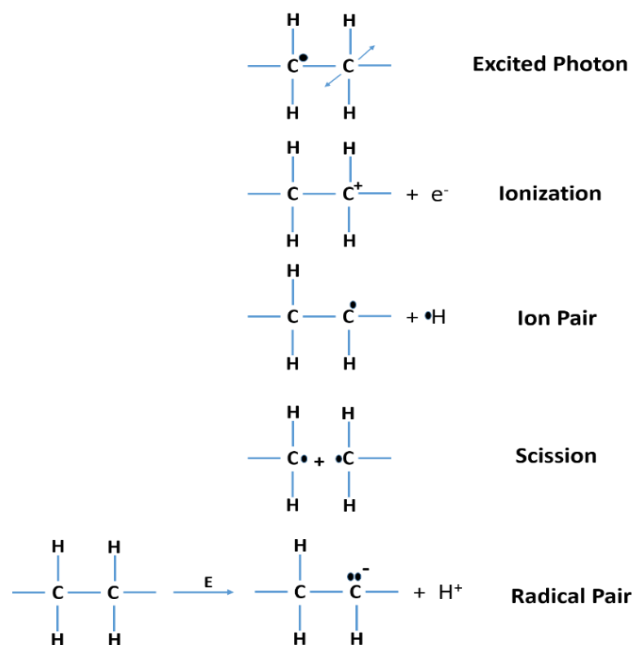


**Figure 1.8:** Radiation-induced reactions in polymer.

### 1.5. Objective of present study

Considering the changes in structure and properties of the polymers with ion irradiation, the present study is, therefore, focused on the modification of the properties of P3HT and PCBM thin films using incident ion beam energies and the mechanism underlying the changes. Any useful improvements in their optical and electrical properties could be used for the fabrication of organic devices with improved performance. It is expected that the results of this work would bear important relevance to material science and especially in the application of polymers in OPV. The objectives of this study are:

- To understand the effect of different electronic energy losses ( $S_e$ ) in the modification of properties of both P3HT and PCBM thin films.
- To investigate the difference in the optical, structural, electrical and morphological properties of P3HT thin films before as well as after irradiation using three different ion beam (90 MeV  $Ni^{7+}$ , 55 MeV  $Si^{4+}$  and 1400 KeV  $Xe^{5+}$ ).
- To investigate the difference in the optical, structural and morphological properties of PCBM thin films before as well as after irradiation using three different ion beams (90 MeV  $Ni^{7+}$ , 55 MeV  $Si^{4+}$  and 1400 KeV  $Xe^{5+}$ ).

# **Literature Review**

## 2.1. Introduction

Conjugated polymers possess the electrical and optical properties similar to that of a semiconductor and also have the processing and mechanical advantages such as they are flexible, solution processable, lightweight etc. P3HT is a semiconducting polymer consisting of a  $\pi$ -conjugated backbone with polythiophene units and pendent alkyl side group. In the crystalline structure, the chains are aligned and stacked on top of each other with the thiophene rings forming a planar alternating 'up-down' conformation and the alkyl side chains are perpendicular to the stacking direction [36]. Such polymers with lamellar  $\pi$ -stack have phase separation with crystalline and amorphous domains that are referred to as a semicrystalline state. P3HT is also a semi-crystalline polymer where the crystallinity depends on many factors like average molecular weight, regioregularity etc. The higher the average molecular weight, less is the crystallinity [72][73][74]. It can be used in flexible optoelectronics devices like organic photovoltaics, field effect transistors, organic light emitting diodes, etc. as it has good charge carrier mobility and efficient energy transfer ability. Two different materials are used in BHJ structure, one as an electron donor and the other as an electron acceptor, to make a blended structure in the active layer. The donor material leads to the major light absorption in the visible region and a coulomb bound electron-holes pair called exciton is generated. This blend structure of donor-acceptor material provides a large interface of the sufficient potential gradient to dissociate the generated excitons into charge carriers within the exciton diffusion length ( $\sim 10$  nm). This charge carries, thus, transport towards the opposite electrodes through the acceptor material.

Therefore, a model combination of P3HT as donor along with PCBM as electron acceptor material is attractive for the fabrication of OSCs. P3HT is efficiently used as the light absorbing and the hole transporting layer (donor material) while, blended with PCBM to form the active layer in OSCs [75][76][77]. High thermal stability, high electron mobility, and electron affinity are the principal properties for the choice of PCBM as an acceptor and charge carrier transporting material [78][79]. Moreover, PCBM containing Phenyl rings and Butyric acid methyl ester side chains attached to the  $C_{60}$  cage improve the solubility and consequently the ease of solution process in different solvents such as chloroform, chlorobenzene and dichlorobenzene etc. [37][80]. PCBM, is a versatile

material, can also be used in thin film transistors [81], memory applications [82], fluorescence spectroscopy measurement of fullerenes [42], etc. as they have deep-lying LUMO levels and n-type semiconducting nature.

Therefore, manipulation and control of the microstructure and morphology of thin film surface are required to improve the performance of any device and new methods to achieve this goal are continuously being pursued worldwide. On the other hand, the role of the impingement of high energy ions on polymer matrix in modifying the structure of the polymers is well known [83][61][84]. Impingement of SHI could produce the collective excitation followed by a large excited volume surrounding the ion path. This excitation can rotate the backbone bonds, and different conformations may be acquired. Moreover, after cooling, the regular section of chains may pack together, and regions of crystallinity are formed [85]. Reduction of the weight is also very much important in the application of solar cells in space [86]. Need for the use of thin film OPVs arises due to their excellent performance as a light weight device in aerospace. Although donor-acceptor blend as active layer performs satisfactorily, but multilayer OPVs are still being studied for improved performances [87]. However, these OPVs may encounter different types of ions in space [88]. Hence the alteration of the performance of these materials under the impingement of ion beams is needed to be studied thoroughly before their qualifications in applications.

A brief literature review on the irradiation effects on certain conducting polymers and the study of fullerene and fullerene derivatives under energetic ions is presented in the following sections.

## **2.2. SHI irradiation of conducting/conjugated polymers**

Irradiation has established itself as one of the most acceptable approaches to alter the properties of any polymer significantly [89][90][91]. To have more insight into polymer modifications induced by swift heavy ion irradiation, a look at the comprehensive literature review is presented below.

- ❖ Eal H. Lee [51] studied the fundamental principle of ion beam interaction of polymeric materials. They explained the interaction mechanisms of charged particles with polymeric materials given nuclear and electronic stopping. The main cause of property change in polymeric material is cross-linking and chain scission.

It is known that cross-linking occur due to electronic process and scission occur due to nuclear process. The linear energy transfer (LET) and ion track concepts can explain the cross-linking and scission mechanisms. The authors have supported the mechanism from their experimental evidence.

- ❖ Mittal et al. [92] have been reported the Hydrogen loss under heavy ion irradiation in polymers. They irradiated polyvinylidene fluoride (PVDF) polymer with 100 MeV Ag ions and polystyrene (PS), polymethyl methacrylate (PMMA), PVDF polymers with 110 MeV Ni ions. They also used 85 MeV Ni ions and 55 MeV Si ions to irradiate polypropylene (PP) and polyimide (PI) polymers to analyze the hydrogen loss mechanism for different ion beam. The authors found that the rate of hydrogen loss is depend on the electronic energy loss and type of bonds present in it. As the ions pass through a polymer, hydrogen gets partially released within the path of the track. At the overlapping ion fluence, the rate of loss of hydrogen decreases and the hydrogen loss curve tends to flatten. This fluence also reveals the track radius.
- ❖ Calcagno et al. [93] have been explained the ion irradiation induced structural modifications of polymer films. They used H, He, Ne, Ar ions in the energy range of 100-400 KeV to irradiate different polymers such as Polyethylene (PE), Polystyrene (PS), Polytetrafluoroethylene (PTFE), Polymethylmethacrylate (PMMA). The transformation from chain structure to amorphous carbonaceous material has been observed. At very low ion fluence only new bonds between chains (crosslinks) are produced in hydrocarbon polymers like PS and PE. By increasing the ion fluence, the original molecular structure is modified, with the formation of bonds between different chains (inter-chains) and within the same chain (intra-chains). At very high energy density, a very stable material is observed due to the complete overlap between ion tracks. The properties of that material are similar to that of hydrogenated amorphous carbon.
- ❖ Calcagno et al. [94] have also been reported the modifications of physical and chemical properties of polymers induced by MeV- KeV range ion irradiation. All the modifications depend on target parameters and ion energy deposition. The modifications in molecular weight distribution (pre gel region) and the polymer



solubility (gel region) can be done by low energy deposition. At high energy deposition, a new chemical system with functional groups and electronic structure is produced which is different with respect to the pristine material. The overlap of ion tracks induces a complete modification of the irradiated material.

- ❖ S. K. Park et al.[95] have been reported the investigation of high energy ion irradiated  $\pi$ -conjugated Polyaniline polymer. They used high energy ions (3-4.5 MeV)  $C^{2+}$ ,  $F^{2+}$  and  $Cl^{2+}$  to irradiated Polyaniline emeraldine based (PAN-EB) samples. The incident ion dose was varying from  $1 \times 10^{12}$  to  $1 \times 10^{16}$  ions/cm<sup>2</sup>. They observed that the  $\pi$ -conjugated pristine system changed from insulating state to carbonized conducting state based on increased conductivity,  $\sigma_{dc}$ , due to high energy ion irradiation with high ion dose. After high energy ion irradiation, the D peak and G peak became dominant which also implies the carbonization of the system.
- ❖ The formation of nanowires based on  $\pi$ -conjugated polymers by high energy ion irradiation has been studied by Satoshi Tuskuda et al. [96]. They used Polystyrene (PS), Polyaniline (PANi) and Poly (3-hexylthiophene) (P3HT) polymers to prepare thin films. The irradiation were carried out using 400 MeV  $Kr^{18+}$ , 320 MeV  $Ru^{18+}$ , 450 MeV  $Xe^{23+}$  and 500 MeV  $Au^{31+}$ . After irradiation, all samples (PS, PANi, P3HT) were adequately developed using cyclohexane, o-dichlorobenzene (oDCB) and dimethylsulfoxide (DMSO) solvents, respectively. The authors found that the size and number density of nanowires can be completely controlled by changing the ion fluence, thickness of film and molecular weight of the polymer. They also observed that for various sizes of nanowires, the characteristics optoelectronic properties are different than those from the solid state. Which is also suggesting that the nanowires are not just finely patterned analogs of the conjugated polymers.
- ❖ The alteration in morphological and electrical properties of Polypyrrole (PPY) films under the irradiation of 100 MeV  $Ag^{8+}$  ion beam have been studied by Amarjeet Kaur et al. [97]. PPY films were prepared by electrochemical polymerization technique and irradiated by 100 MeV  $Ag^{8+}$  ion beam with different ion fluences ranging from  $1 \times 10^{10}$  to  $1 \times 10^{12}$  ions/cm<sup>2</sup>. They observed the increased conductivity by two orders after irradiation which is due to the reordering of

polymer chains and generation of charge carriers in that process. The results were further supported by XRD spectra which are showing increased intensity after high energy ion irradiation.

- ❖ Study on conducting polypyrrole (PPY) polymer thin films, prepared by the electrochemical process has also reported by R. C. Ramola et al.[98]. Thin films of PPY were irradiated with 50 MeV  $\text{Li}^{3+}$  and 90 MeV  $\text{C}^{6+}$  ions. The crystallinity of the PPY films increases with increasing fluences of lithium ions. Amorphization observed at higher fluence. The energy deposition in the range 50–70KeV/ $\mu\text{m}$  leads to the formation of the conjugated system, radical-radical recombination and cross-linking. The polymer destruction occurs simultaneously along with amorphization due to irradiation with 50 MeV Li ions as deposition energy is higher than 200KeV/ $\mu\text{m}$ . But polymer destruction and simultaneous amorphization even at low fluence was observed due to carbon ions irradiations. The surface conductivity of films increases with increasing fluence of Li ions, but at higher fluences it becomes same as pristine film conductivity. It was found that carbon ions do not much affect the surface conductivity of PPY. The surface conductivity behavior depends on the surface roughness, chain breaking of PPY films.
- ❖ Poly (3-Methylthiophene) (P3MT) was synthesized by chemical oxidation polymerization method using  $\text{FeCl}_3$  and thin films were deposited over glass and Si substrates. Deposited thin films were irradiated with 60 MeV  $\text{Si}^{5+}$  ion beam at different fluences ranging from  $3.3 \times 10^{10}$  to  $3.3 \times 10^{12}$  ions/ $\text{cm}^2$ . Optical, electrical and structural properties were studied by G. B. V. S. Lakshmi et al. [99]. Dc conductivity increased by four orders after irradiation. The optical gap decreased along with the release of various gases during irradiation causes the crosslinking in P3MT. They also found a decrease in the amorphous variety which causes an increase in the conductivity of the polymer. During the irradiation, various gases also released and lead to the formation of the carbon-rich cluster along the ion path. This cluster formation increases with increasing ion fluence and makes the polymer inhomogeneous, which in turn favors the increase in band conduction. Therefore, the conductivity was found to be due to the band conduction.

- ❖ In a subsequent study, they irradiated P3MT films using 60 MeV  $C^{5+}$  swift heavy ion beam and again analyzed the structural, optical and electrical properties of irradiated films [100]. The increased conductivity by order of one along with the decreased optical bandgap after high energy ion irradiation was observed. The conduction mechanism found to be band conduction. The FTIR analysis confirmed the release of methyl group. The change in the conjugation of polymer and  $n-\pi^*$  transitions was indicated by red and blue shifts in the absorption peaks. After comparing the results with  $Si^{5+}$  ion irradiated P3MT [99], the role of  $S_e$  in the modifications of the polymers due to irradiation can understand.
- ❖ G. B. V. S. Lakshmi et al. [101] have been reported the effect of 60 MeV  $Si^{5+}$  ion beam on poly (3-octylthiophene) (P3OT) thin films. The evolution of gases was monitored using on-line quadrupole mass analysis which reveals the chain scissoring and thus chemical changes in the polymer due to ring breaking, main and side chain scissoring of the P3OT during irradiation. The bond scissoring in the localized region of polymer chains was evaluated using decreased FTIR transmission intensity with increased fluences. They also found the decreased crystallinity in irradiated films with increased fluences as well as bandgap which was estimated from UV-visible absorption spectra. Authors have explained that all the modifications are due to the change in chemical structure in ion track region.
- ❖ A. Srivastava et al. [102] have been studied the effect of 100 MeV  $Si^{8+}$  ions on polycarbonate films. They studied the changes in chemical, optical and thermal properties before as well as after irradiation. They concluded that polycarbonate shows substantial modification in its chemical, optical and thermal characteristics when, it is irradiated with swift heavy ions. The chemical modification observed by breaking of the cleavage C-O single bond of carbonate and formation of phenolic O-H bond with the phenoxy radical presumably abstracting hydrogen from the neighboring isopropyl group. They found a slight red shift in optical absorption spectra with increased ion fluences. A gradual decrease in the glass transition temperature with increase in ion fluence was also observed.
- ❖ Polymer nanowires have been prepared by high energy single particle track reactions in semiconducting cross-linked polymers [103]. The irradiation process

of cross-linking polymers with energetic ions produces nanowires by cross-linking reactions along the ion track path. The thin films of poly(9,9'-di-n-octylfluorene) (PFO), regioregular poly(3-hexylthiophene) (rrP3HT), and poly[2-methoxy-5-(2'-ethylhexyloxy)-1,4-phenylenevinylene] (MEH-PPV) were irradiated by 450 MeV Xe<sup>25+</sup> or 490 MeV Os<sup>30+</sup> particles. The irradiated films were developed directly in toluene, chlorobenzene, or chloroform for 1–30 min. The authors found that fabrication of one-dimensional nanostructures is possible by using SPNT technique for various conducting polymers along with controlled sizes. The cross-linking G value for the polymers decides the stability of these nanowires. By increasing the molecular weight of the polymers, the structural damage induced by irradiation can also be significantly diminished. The emission studies of these irradiated films exhibiting sharp and intense emission with high fluorescence quantum yield indicating the absence of any inter/intra polymer interactions in the nanowire assemblies. These nanostructures of function polymers with controlled dimensions can be useful for advanced device applications.

### **2.3. SHI irradiation of fullerene/fullerene derivatives**

The following literature survey summarizes the reported studies on high energy irradiation induced an alteration in fullerene and fullerene derivatives.

- ❖ A comparative study of the effect of SHI on fullerene C<sub>60</sub> thin films with different S<sub>e</sub> values ranging from 80 to 1270 eV/Å has been reported by Bajwa et al. [104]. The incident fluence ranges varying between 10<sup>10</sup> and 10<sup>14</sup> ions/cm<sup>2</sup>. Different ion species like O, Ni and Au were used for irradiation process. It was observed that at low fluences polymer formation take place but at higher fluences complete fragmentation of C<sub>60</sub> i.e., amorphous carbon was observed. The measured bandgap values and resistivity was also found to be decreased with fluence. The increased dc conductivity and the decreased bandgap of C<sub>60</sub> films at high fluences of SHI irradiation are related to the formation of a-C. It was also observed that for smaller S<sub>e</sub>, the maximum of the polymerization is larger. Quantitative formula describes that ion species and fluences are required for given amount of polymerization. Also, the fluences and ion species are required for complete transformation of C<sub>60</sub> to a-C. Thus, SHI irradiation caused to localized damage. The material remains non-

conducting until with increasing fluences but at some higher fluence the material becomes conducting because percolation paths open up. Further irradiation on this conducting material, however, destroys  $C_{60}$  molecules mainly by  $S_n$ , analogous to damage in metallic systems.

- ❖ An investigation on the modifications induced by SHI irradiation on fullerene  $C_{70}$  thin films has been reported by Rahul Singhal et al. [105]. Thin films of  $C_{70}$  were irradiated using 120 MeV Au ion beam with different fluences. Evaluation of radius of damaged cylindrical zones and damage cross-section revealed the complete amorphization of the carbon structure of the fullerene molecules at higher fluence. The decreased bandgap with increasing ion fluences was also observed. Increased conductivity of irradiated fullerene beyond a fluence of  $1 \times 10^{12}$  ions/cm<sup>2</sup> shows the transformation of  $C_{70}$  into a-C within each ion track. At a fluence of  $3 \times 10^{13}$  ions/cm<sup>2</sup>, the molecule is transformed into a-C.
- ❖ The ordering effect in fullerene ( $C_{60}$ ) thin films due to energetic ion impact have been reported [106]. Fullerene films (~500 nm) were deposited using the resistive heating method and irradiated with 200 MeV Au ion beam at different fluence. The improvement of vibration strength in fullerene films at low fluences was observed along with the structural ordering at low fluences. The ordering at low fluences has been explained in terms of ion-solid interaction. The ordering at low fluence is due to the less heating effect in tracks halo region with much larger radii. At the higher fluences, this ordering phenomenon is expected to vanish as the damaged core starts to overlap. Therefore, decreased intensity of vibration modes and lattice diffraction at higher fluence is observed.
- ❖ R. Singhal et al. [107] irradiated the thin films of  $C_{60}$  and  $C_{70}$  with 120 MeV Ag ion beam. By analysis of damage cross-section and radius of the damaged cylindrical zone, it was observed that  $C_{70}$  is more stable under high energy irradiation. As fullerene  $C_{60}$  has low thermal conductivity and the higher damage cross-section for  $C_{60}$  is explained using thermal spike model.  $C_{70}$  has less damage cross section compared with that of  $C_{60}$ . At a fluence of  $3 \times 10^{13}$  ions/cm<sup>2</sup>, the fullerene is completely transformed into a-C in both films ( $C_{60}$  and  $C_{70}$ ).

- ❖ A detailed study on the effect of energy loss of ions on the tuning of surface plasmon resonance (SPR) wavelength of Au nanoparticles (NPs) in fullerene C<sub>70</sub> matrix is reported by R. Singhal et al. [108]. The SPR wavelength of Au-C<sub>70</sub> nanocomposite thin films was tuned using the transformation of fullerene C<sub>70</sub> into a-C under energetic ion impact. It was observed that the tuning range of SPR wavelength increases with the increased electronic energy loss of incident ion beam. It was also observed that nuclear energy loss are less effective for SPR tuning in comparison with the electronic excitations.
- ❖ Yuta maeyoshi et al. [109] have been reported the development of organic semiconducting nanowires using high energy irradiation or single particle nanofabrication technique (SPNT). These nanowires can be used as charge carrier transport pathways in flexible and lightweight nano-electronics. The fabrication of fullerene nanowires, that is also applicable to its derivatives such as pristine C<sub>60</sub>, methanofullerenes of C<sub>61</sub> and C<sub>71</sub> (PC<sub>61</sub>BM and PC<sub>71</sub>BM), and indene C<sub>60</sub> bis-adduct (ICBA), is reported. The thin films of PC<sub>61</sub>BM, PC<sub>71</sub>BM and ICBA were drop cast on Si substrate and irradiated with 450 MeV Xe or 490 MeV Os ion beams. The number density of incident ions was  $1 \times 10^8$  to  $1 \times 10^{11}$  ions/cm<sup>2</sup>. All the irradiated films were developed using oDCB and chlorobenzene (CB) solvents. It is observed that length of nanowires and density depends on the film thickness of the film and ion fluence.

They also used these PC<sub>61</sub>BM nanowires with controlled length and density in the fabrication of P3HT:PC<sub>61</sub>BM BHJ structure based OPVs to demonstrate the applicability of these nanowires to enhanced power conversion efficiency (PCE). A high density of nanowires caused an abrupt decrease in PCE for both normal and inverted cell structures, which is showing the negative effect on the device.

- ❖ Formation of nanowires of using SPNT technique another fullerene derivative, indene C<sub>60</sub> bis-adduct (ICBA), and incorporating them into P3HT: ICBA OPV with optimized length has reported by Shotaro Suwa et al. [110]. Thin films of ICBA were irradiated using 490 MeV Os particles and developed with (CB). The PCE of OPV after incorporating optimized nanowires was found to be increased along with the increased short-circuit current density.

- ❖ Ping Zhou et al. [111] have been studied the “2+2 cycloaddition” photochemical reaction to drive the photo-polymerization of solid C<sub>60</sub>. They observed that this reaction proceed via the triplet T<sub>1</sub> state and exhibits threshold temperature which is near to the orientational ordering transformation of solid C<sub>60</sub>. 2+2 cycloaddition reaction is very well known and resulting in the covalent attachment of two otherwise van der Waals bonded molecules. When, two carbon double bonds on adjacent molecules are parallel oriented and separated by less than ~4.2 Å, this reaction is active in molecular solids. Using the photochemical assistance, an excited molecular state is formed and leads to breaking of double bonds and reform as a four-sided ring. Below the threshold, the requirement of topochemical of reactive double bond alignment on adjacent C<sub>60</sub> molecules becomes improbable and suppressing the reaction rate.
- ❖ The effect of high pressure and temperature on the structure of fullerene C<sub>60</sub> has been studied by Y. Iwasa et al. [112]. Pristine C<sub>60</sub> shown a metastable and revert to pristine C<sub>60</sub> state on reheating to 300 °C temperature at ambient pressure. All the results show the reconstruction of a structure, bonding and electronic states which is suggesting the chemical bonding between neighboring C<sub>60</sub> molecules. The existence of two phases and photo polymerized C<sub>60</sub> further suggests the presence of other metastable phases containing linked C<sub>60</sub> molecules.
- ❖ The observation reported by A. M. Rao et al. [113] are indicating the polymerization process of solid C<sub>60</sub> due to the application of visible or ultraviolet (UV) lights. Authors also investigated the effects of polymerization on vibrational modes of solid C<sub>60</sub> and found the many more lines in Raman and IR spectra of photo-transformed phase. The existence of these line indicating the icosahedral symmetry of C<sub>60</sub> molecule has been lowered supporting the proposed photo-polymerization process. The broadening of the electronic absorption bands of C<sub>60</sub> without changing their position indicates the molecular structure of the monomers was closely related to that of C<sub>60</sub> which is further supported by luminescence spectra of photo-transformed C<sub>60</sub> films. The broadening of XRD peaks indicates the disordering in the films. A slight shift of peak position towards the higher scattering angle also shows the contraction in the lattice constant due to

polymerization reactions, i.e., 2+2 cycloaddition reactions in which van der Waals bonds between C<sub>60</sub> molecules are replaced by covalent bonds.

#### 2.4. Summary of some other literature review

Sr. No.	Materials used	Modification Process used	Key Observations	Ref.
1.	P3HT (thickness ~ 10 μ m)	100 MeV Ag <sup>8+</sup> SHI irradiation	Increased conductivity by two orders. Reordering of polymer chains which may introduce polaronic defects that contribute to increased conductivity.	[114]
2.	P3HT (thickness ~ 10 μ m)	100 MeV Ag <sup>8+</sup> SHI irradiation	Structural and morphological modification observed due to the liberation of molecular fragments due to ion impact. This may cause defects, crosslink, chain scissoring or both.	[115]
3.	Polyether-sulphone and polyamide-nylon-6	50 MeV Li <sup>3+</sup> SHI irradiation	Increased intensity of XRD peaks shown the alignment of polymeric chains in a regular pattern. Decrement in the bandgap energy of irradiated polymers is due to the shift of UV-visible spectra towards higher wavelength.	[116]
4.	Polyethylene (PE) polysulphone (PSF) and polyethersulphone (PES).	2 MeV electron, 10 and 20 MeV proton, 20 and 50 MeV He <sup>+2</sup> , 220 MeV C <sup>5+</sup> ion irradiation	Change in mechanical properties of PES and PSF polymer were observed and explained using LET effects. Whereas, in the case of the aliphatic polymer of PE, LET effects is negligible. This result indicates that appearance or not of LET effects depends on aromaticity of polymer.	[117]
5.	Polymethyl methacrylate (PMMA) foils	70 MeV C <sup>5+</sup> ions	Analysis of absorption spectra, FTIR spectra, and XRD spectra show anomalous behavior with fluence, which may be due to both degradation (scission) and cross-linking of polymer chains competing simultaneously.	[118]
6.	conjugated polymer molecule orders in the solid state	Mini Review article	The physical properties of organic materials and properties of their corresponding device depends on molecular ordering and orientation. This mini-review highlights recent progress in the various techniques including optimizing solution-processes, rational chemical design, and growth of high-quality crystalline polymer micro/nanostructures for ordering conjugated polymer molecules to achieve high	[119]



			performance of devices. It is a scientific challenge to control polymer molecular ordering with the desired alignment in the solid state due to their high molecular weight, complex intermolecular interactions and easily tangled flexible chain segments in the molecular structure, which, need to overcome multiple free energy barriers associated with the self-assembly process	
7.	Polypropylene (PP), polyethylene terephthalate (PET), polycarbonate (PC) and poly(ether ether ketone) (PEEK) foils	9.6 MeV C <sup>4+</sup> and O <sup>4+</sup> ions	The irradiation of polymers with O ion leads to hydrogen release, higher changes of roughness, oxygen depletion and a shift of the UV-visible absorption edge. The changes induced by irradiation are strongly dependent on their chemical structure and ion fluence.	[120]
8.	Polyaniline (PANI)-polyvinyl alcohol (PVA)	150 keV Argon (Ar <sup>9+</sup> ) ion	The implantation process with Ar <sup>9+</sup> ions indicating a signature of scission of polymer bonds and voids formation as well. Increased dc resistivity and dielectric loss was also observed. The dc transport has revealed a decrease in localization length associated with the scission of polymer bond in the implanted polymer.	[121]
9.	poly(carbosilane)-poly(vinyl silane) (PCS-PVS), poly(methylphenylsilane)	Xe or Au ions irradiation	The formation of nanowires with radii 7-30 nm was observed. The radius of nanowires depends on used ion beam. The efficiency of the cross-linking reaction due to deposited energy along the ion tracks is responsible for the difference in size of nanowires.	[122]
10.	Poly(3-hexylthiophene-2,5-diyl) (rrP3HT) crystal	Structural and electronic properties	Decrement in the bandgap by 0.82 eV is due to the tightly packed crystal formation and an increase of 0.60 and 1.33 eV for the HOMO and LUMO dispersion, respectively. The creation of the structural organization and by a modulation of interchain spacing in the $\pi$ -	[123]

			stacking direction are responsible for electronic properties engineering of the rrP3HT crystal.	
11.	poly(3-hexylthiophene) thin film	Crystallite orientations, molecular packing disorder, hole mobility	Efficient transport occurs mostly within the observed interfacial layer and requires good interconnectivity between well-ordered aggregates. The ability to nucleate well-ordered, extended $\pi$ -stacked aggregates off the substrate-film interface, for instance, is more important for FET applications.	[124]
12.	C <sub>60</sub> , C <sub>70</sub> , [6,6]-phenyl-C <sub>61</sub> -butyric-acid-methyl-ester ([C <sub>60</sub> ]PCBM), and bis-[C <sub>60</sub> ]PCBM	First principles investigation	The intrinsic morphological difference can have significant effects on the open-circuit voltage, providing a theoretical confirmation of morphology as an important factor in organic photovoltaic.	[125]
13.	[6,6]-phenyl-C <sub>61</sub> -butyric acid methyl ester (PCBM)	Molecular ordering	The phenyl ester groups needed for solution processability create kinetic challenges for molecular ordering.	[126]
14.	P3HT and PCBM BJJ	Diffusion of PCBM in P3HT	Diffusion coefficient for disordered PCBM in P3HT is strongly dependent on the annealing temperature and weakly dependent on the PCBM concentration.	[127]
15.	Spin-coated PCBM and evaporated C <sub>60</sub> film	Photo degradation of electronic structure	Due to exposure to simulated sun light, filled and empty molecular orbitals are strongly altered, indicating that the conjugated $\pi$ -system of the C <sub>60</sub> -cage has degraded. Results emphasize the need to control the air and light exposure, during all steps of the OPV fabrication and characterization, including during the storage and transport of materials and films.	[128]

## 2.5. Motivation of thesis problem

After analysis of earlier studies mentioned above, we were able to define the thesis work in the following manner:

- ❖ Irradiation of material can alter/modify the structure and properties at nano-level with precise control on deposited electronic energy, incident ion density and target material.
- ❖ Improvement in the electrical conductivity, a possible consequence of the irradiation can be very useful for the organic devices.
- ❖ Alteration in optical, electronic and morphological properties of the conducting polymers can also improve the performance of the devices.
- ❖ No earlier study could be found on the effect of ion irradiation of P3HT-PCBM system at nanometer scale, very important for the OPVs. Therefore, investigations of the structure and properties of these two materials under ion irradiation of different energies can provide an overview on the application of these materials in devices and also in radiation prone zones or space vehicles.



**Materials &  
Methods**

### 3.1. P3HT and PCBM materials

The conjugated rr-P3HT polymer was obtained from Sycon Bombay. The regioregularity of P3HT polymer is > 99% and molecular weight is  $\sim 45000 \text{ g mol}^{-1}$ . P3HT polymer was dissolved in chlorobenzene (CB) to make solution. CB was purchased from Merck with > 99% purity. The fullerene derivative, PCBM, powder was purchased from Ossila, UK with purity 99.5%. The molecular weight of PCBM was 911 g/mol. PCBM was also dissolved in CB solvent to make solution.

### 3.2. Sample preparation technique

P3HT and PCBM thin films were prepared by spin coating technique. Spin coating technique is a low cost and relatively fast method to produce homogeneous layer. In this process, an excess amount of the solution is placed over the substrate, which, is stuck on a chuck by vacuum. The substrate is then rotated at a very high speed to spread the solvent over the substrate homogeneously by centrifugal force. The beauty of this technique is that the thickness of the deposited film can be adjusted/controlled by optimizing rotation time, rotation speed, the number of coatings and concentration of used solution. Generally heat treatment is provided to the spin coated substrates after every coating. This post spin coating heat treatment helps to obtain films with better homogenization of the composition, density and adhesion. A schematic diagram of the spin coating process is presented in **Figure 3.1** which, describes the various stages in the process.

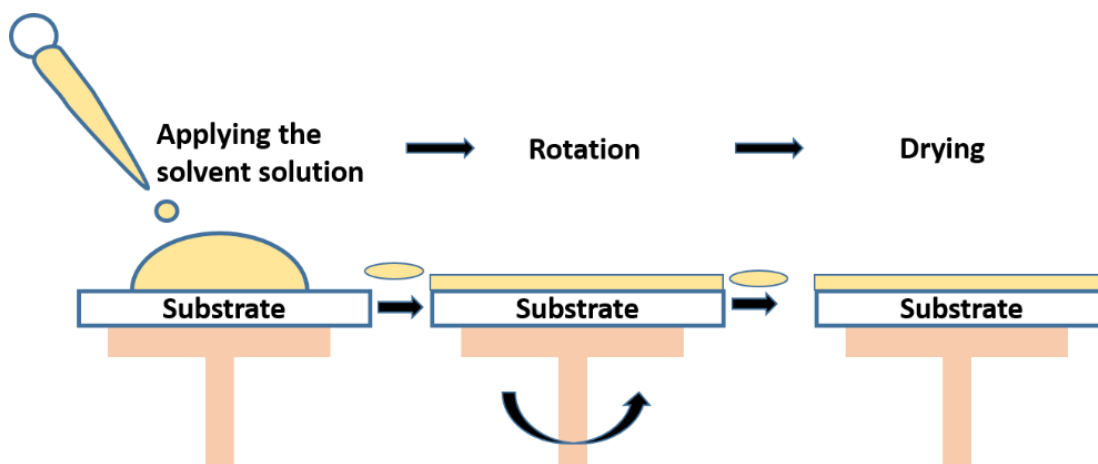


**Figure 3.1:** Schematic of spin coating process.

As received P3HT polymer was dissolved in CB solvent by stirring. The prepared solution was spin cast on the two different substrates (glass and double side polished Si) using a programmable spin coater (Apex equipments, NXG-m1) (**Figure 3.2**). The rotation speed during the deposition was 800 rpm and spin time was 50 s. Before depositing the solution over the substrates, the substrates were sequentially cleaned with soap solution, deionized water, acetone and isopropanol for 15 min each in an ultrasonic bath and then dried. After the coating process, each specimen was heated at the temperature 100 °C and held for 10 min to evaporate the residual solvent.

The PCBM thin films were also deposited by spin coating technique by adopting above mentioned process parameters. The thickness of P3HT and PCBM thin films were measured using Dektak stylus surface profiler at Inter University Accelerator Centre (IUAC), New Delhi. All the films were irradiated by high energy ions after the deposition.



**Figure 3.2:** Spin coating unit used for present deposition.

### **3.3. Ion beam techniques for engineering the properties of materials**

To engineer the properties of these thin films many techniques are used. These modification processes may bring drastic changes in the properties of the materials. Therefore, high and low energy ion beam irradiation were used, in the present study to modify the optical, structural and electrical properties of the thin films.

#### **3.3.1. Swift heavy ion irradiation**

### **Pelletron accelerator:**

In the present work, 15 UD Pelletron accelerator at IUAC, New Delhi is used for high energy ion irradiation process [129][130]. This accelerator is a Tandem Van de Graff electrostatic accelerator. In this accelerator chain of pellets is used rather than charge carrier belt. The digit 15 stands for 15 MV terminal voltage and UD stands for Unit Double. This accelerator has the capability of accelerating almost all type of ions from Proton to Uranium (except inert gases). The energy of the ion beam can be from a few MeV (million electron volts) to hundreds of MeV depending on the type of ion species. It has been installed at IUAC, New Delhi by the Electrostatic International Inc., USA. A schematic diagram of Pelletron Accelerator is presented in **Figure 3.3**. The Pelletron machine is mounted vertically in a stainless steel tank. This tank has the height of 26.5 m and diameter of 5.5 m. In the top portion of the tank, there is an ion source system consisting of a high negative potential deck, SNICS, vacuum system, power supplies and controls of the ion source required to produce and inject the negative ions into accelerating tank. A high voltage terminal which, can hold potential from 4 to 16 MV is placed in the middle of the tank. This voltage terminal is about 3.81 m in height and 1.52 m in diameter. The ceramic titanium diffusion bonded accelerating tubes are used to maintain a potential gradient from high voltage to ground, from bottom of the tank as well as at the top of the ground. The sulfur hexafluoride ( $\text{SF}_6$ ) insulating gas with high dielectric constant is filled into the tank. The pressure of gas is around 6-7 bar. This gas insulates (to prevent sparking/discharging) the high voltage terminal from the tank wall and is always maintained.

Initially, the negative ions are produced from the ion source and pre-accelerated to 250 KeV. The MC-SNICS (Multi-Cathode source of negative ions by cesium sputtering) ion source is used to generate ions. Cesium (Cs) vapor is formed by electrical heating of Cs ion source which, falls on the area enclosed between cathode (which, is kept cooled) to heat the surface of the ionizing material. Cool cathode condenses some of the cesium on the front and some Cs ionizes to  $\text{Cs}^+$  ion because of hot surface.  $\text{Cs}^+$  ions are accelerated by applying suitable voltage across the ionizer and the cathode. The  $\text{Cs}^+$  ions impinge on the target and sputter the target atoms. The sputtered material may consist of neutral atoms or positively and negatively charged ions. Neutral or positively charged atoms will take up



electron/s on passing through the condensed layer of cesium and thus produce negatively charged ions.

The dipole magnet at 90° called ‘injector magnet’ is used to analyze the ions of different masses. This injector magnet is bent in downward direction towards the terminal. The negative ions which, are passing through the accelerating tubes towards to the positive terminal, get accelerated. At the terminal, they encounter with a stripper (C-foil or N<sub>2</sub> gas stripper) and some electrons are stripped off via stripper foil and resulting yield transformed into positive ions. These ions are then repelled by the cathode voltage towards the ionizer and then are made to pass through a hole to the ground potential of the extraction electrode. After exiting from the tank, the ion beam corresponding to a particular energy and charge state is selected and bent into the horizontal plane by analyzing magnet. At the end, to divert the energetic ion beams to various beamlines for different experimental areas, the switching magnet is used. The ultra-high vacuum is maintained in the whole beam line of the accelerator. The steering magnets and quadrupole magnets are used to keep the ion beam focused and centered. The ion beam is visually monitored by glow on quartz and beam profile monitors (BPM). The ion beam current is measured using Faraday cups.

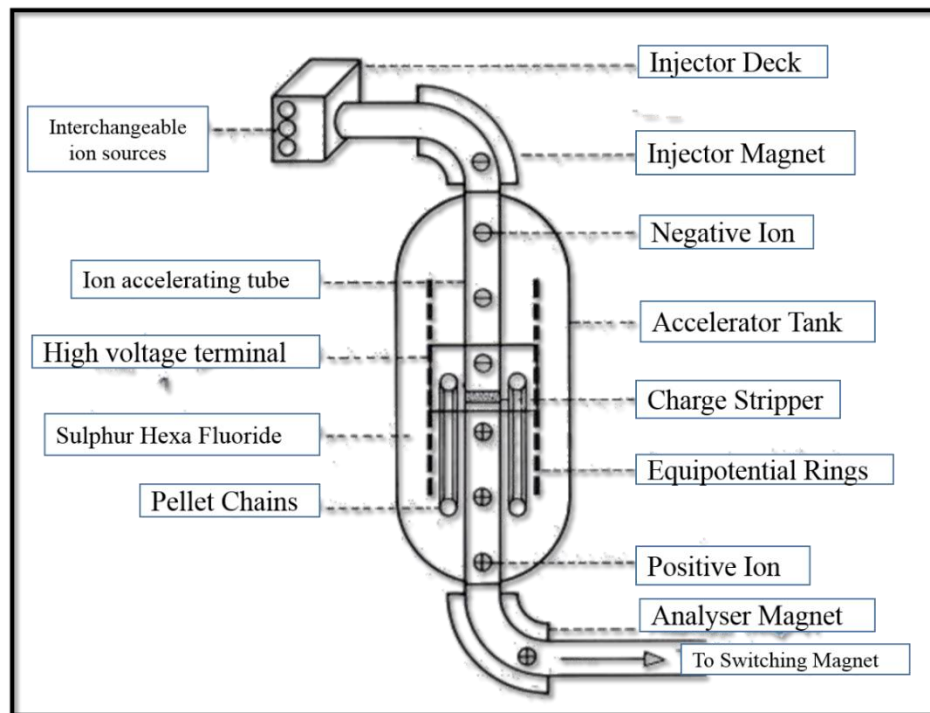


**Figure 3.3:** Schematic diagram of Pelletron accelerator at IUAC, New Delhi.

The final energy of the ions emerging from the accelerator is given as:

$$E = [E_{deck} + (1 + q)V_T] \quad (3.1)$$

Where ' $V_T$ ' is the terminal potential in 'MV', ' $q$ ' is the charge state of the ion after stripping and ' $E_{deck}$ ' is the deck potential of the MC-SNICS source.

### **Irradiation procedure:**

The material science beamline at IUAC, New Delhi situated at  $15^\circ$  angle to the right with respect to the direction of the un-switched direct beam was used for the irradiation of the thin films in the present study. Ultra-high vacuum ( $\sim 10^{-9}$  Torr) was maintained in the beam line. The vacuum level of the irradiation chamber was maintained below  $10^{-6}$  Torr using turbo molecular pump backed by a rotary pump. The irradiation chamber was made up of stainless steel and has the diameter about 68 cm. A four-sided target ladder which, is made of copper is used to mount the samples (maximum 24). This ladder is installed from the top in the irradiation chamber. The up and down motion of the ladder during the irradiation process is controlled using the stepper motor from the remote data acquisition room. A CCD camera with a light bulb is provided to view inside the irradiation chamber during the experiment. A magnetic quadrupole and a steerer is used to focus the beam on the target. The irradiation process was performed at room temperature while, keeping the beam current constant. For attaining uniform irradiation, the beam was scanned in X- and Y- directions in the maximum area of  $1 \times 1 \text{ cm}^2$  using an electromagnetic scanner. The time ' $t$ ' of rastering ion can be estimated using the following formula:

$$t = Q \left\{ \frac{f \times A \times e}{i} \right\} \quad (3.2)$$

Where, ' $Q$ ' is ionic charge state, ' $f$ ' is fluences given in ions/ $\text{cm}^2$ , ' $A$ ' is the area, ' $e$ ' shows the charge and ' $i$ ' represents the current. Using this formula, time required for particular fluence in irradiation is calculated.

### **3.3.2. Low energy ion irradiation**

Low energy ion beam irradiation facility (LEBIF) was used to modify the near surface properties of the material [131]. Ion bombardment on the target materials leads to the energy loss during their passage inside the materials and are finally stopped at a depth determined by their acceleration energy. In this region of energy, mainly elastic collisions play an important role. Ions are accelerated to energies in the range of tens of electron volts (eV) to a few MeVs. Low energy ion beam accelerator is made up with an ion source, an accelerating system and magnetic mass analyzer. Inside a conventional implanter, to form a beam of charged ions gas is injecting into the ion source. A plasma is created by ionizing the injected gas. The acceleration of atom is also obtained by ionization. To extract the ions from the source, an electrostatic field is applying under high vacuum (pressures  $< 10^{-5}$  Torr). While, the ion beam of solid materials is formed by heating the solid near the melting temperature in a microwave oven.

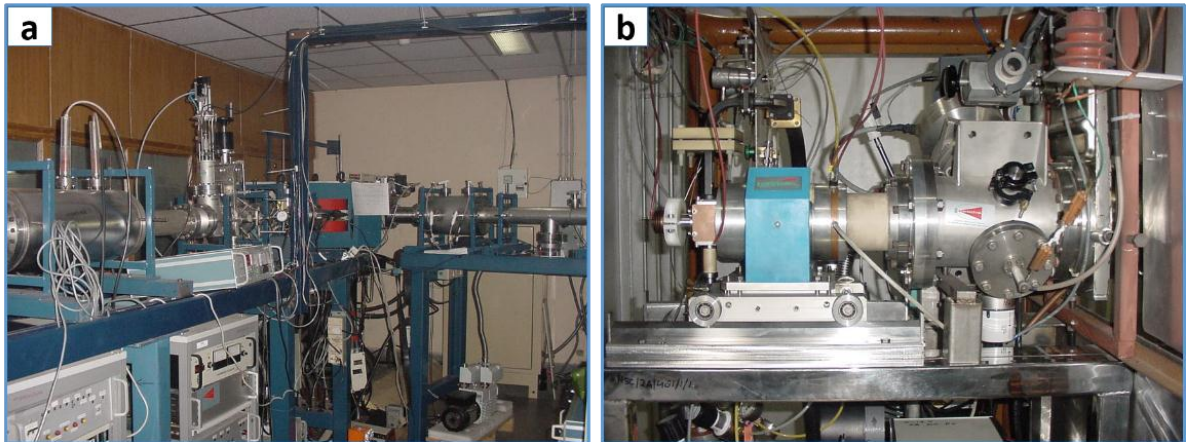


**Figure 3.4:** Image of LEBIF facility available at IUAC, New Delhi (a) and electron cyclotron resonance source (b).

Low energy ion beam facility (LEBIF) was used in the present study to irradiate thin films at low energy and high mass ions. **Figure 3.4 (a)** shows the image of LEBIF facility at IUAC, New Delhi. This facility consists of an Electron Cyclotron Resonance (ECR) ion source (**Figure 3.4 (b)**) installed on a high voltage deck. For the confinement of plasma radially and axially, permanent magnet (NdFeB) was used. A high voltage deck was utilized to place all the electronic control device and UHF transmitter (10 GHz) of the ECR source. To control these components, optical fiber communication is used in multiplexed

mode. The beam lines with their different components such as metal double slit, faraday cups, UHV scattering chamber, electrostatic quadrupole triplet lens etc., the accelerating system and the high voltage platform have been designed and developed indigenously. The ion beams extracted from the ECR source in the form of charge. The dipole magnet is used to analyze the mass and selected beam is injected into two available beam lines which, are situated at 90° and 15°. The dipole magnet which, separates the two experimental beam lines is also showing in **Figure 3.4 (a)**.

### 3.3.3. Summary of SRIM data of incident ion beams on P3HT and PCBM thin films

Present work was carried out using three different ion beam with different energy and mass of incident ions. P3HT and PCBM thin films were irradiated with 90 MeV Ni<sup>7+</sup> ions where mass of ion was 57.94 amu and 55 MeV Si<sup>4+</sup> ions having 27.97 amu mass at Material Science beam line of Pelletron accelerator, IUAC, New Delhi. The above described procedure was followed. To irradiate P3HT and PCBM films at low energy with high mass ions (1400 KeV Xe<sup>5+</sup> ions having 131.90 amu mass), irradiation was carried out using LEBIF facility at IUAC, New Delhi. The calculated value of S<sub>e</sub>, S<sub>n</sub> and range using SRIM software of different ions in P3HT and PCBM matrix is summarized in the following **Table 3.1**.

**Table 3.1:** Summary of SRIM data

		<b>P3HT (C<sub>10</sub>H<sub>14</sub>S)</b>	<b>PCBM (C<sub>72</sub>H<sub>14</sub>O<sub>2</sub>)</b>
<b>Deposition Parameters</b>	Spin Rate (rpm)	800	800
	Spin time (s)	50	50
<b>90 MeV Ni<sup>7+</sup> ions beam</b>	S <sub>e</sub> (eV/nm)	4788	7736
	S <sub>n</sub> (eV/nm)	8.390	13.19
	Range (μm)	26.89	16.59
	Current	0.2 pA	0.2 pA
<b>55 MeV Si<sup>4+</sup> ions beam</b>	S <sub>e</sub> (eV/nm)	1921	3146
	S <sub>n</sub> (eV/nm)	1.878	2.942
	Range (μm)	27.03	16.73

	Current	0.4 pA	0.4 pA
<b>1400 KeV Xe<sup>5+</sup> ion beam</b>	S <sub>e</sub> (eV/nm)	746.3	1344
	S <sub>n</sub> (eV/nm)	821.6	1366
	Range (Å)	8905	5122
	Current	100 nA	100 nA

### 3.4. Sample characterization techniques

After undergoing the irradiation process, the P3HT and PCBM thin films were characterized using the following techniques:

#### 3.4.1. X-ray diffraction (XRD)

XRD is a non-destructive, versatile analytical technique for the quantitative determination and identification of various crystalline forms. It reveals the detailed information about the structural and physical properties of material and thin films. Therefore, it finds a wide range of applications in material characterization [132]. XRD is based on the constructive interference of monochromatic X-rays and a crystalline sample. The X-rays diffracted by atoms because the wavelength of X-rays (0.5-2.5 Å) is close to the atomic size (~ 1.5 Å). The interference (constructively or destructively) of diffracted X-rays with other occur if the atoms or ions are arranged in a regular manner and depending on the path difference (**Figure 3.5**). In 1913, English physicists Sir W.H. Bragg and his son Sir W.L. Bragg developed a relationship to explain as to why the cleavage faces of crystals appear to reflect X-ray beams at certain angles of incidence (Theta,  $\theta$ ). They came up with Bragg's law [133] which, is given by **Equation 3.3**:

$$n\lambda = 2d \sin\theta \quad (3.3)$$

Where 'n' is an integer, ' $\lambda$ ' is the wavelength of incident x-rays and 'd' represents the interplanar spacing between the lattice planes.

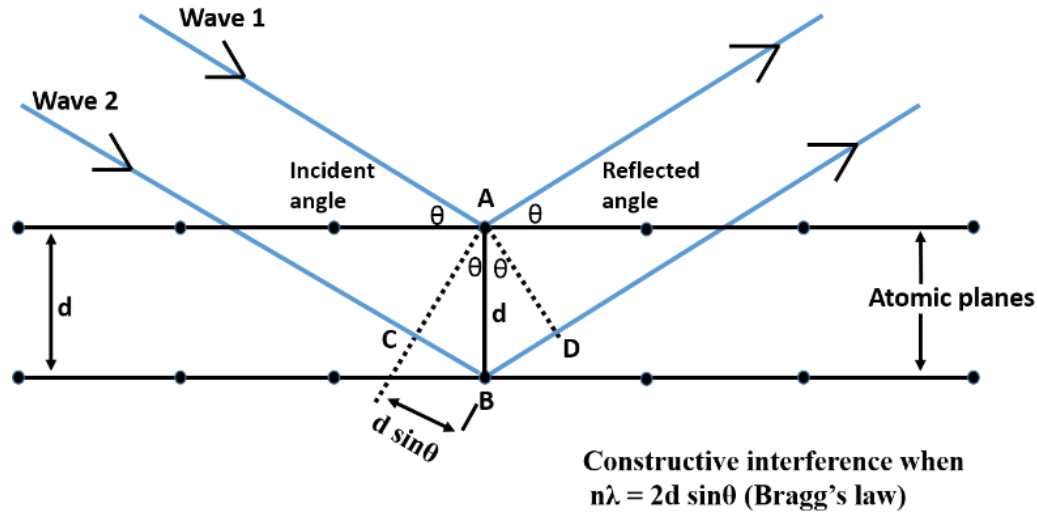


**Figure 3.5:** Schematic of diffraction pattern (Bragg's law).

**Figure 3.6** shows the conventional layout of XRD instrument. The typical XRD measurement starts with the production of X-rays. The X-ray will then be incident to the sample and a diffraction pattern is obtained. Then detector will detect this pattern and interpret the data needed for sample. It is important to have a smooth plane surface. To diffract an X-ray beam, the reflection plane must meet the incident X-ray beam at one of the specified angles of a crystal. It is necessary that the X-ray reflected from the different points on these planes reach the detector in phase. When, the number of diffracting planes are large, containing thousands of parallel planes, this condition is satisfied very accurately and hence the diffraction maxima are sharp. Therefore, when, the crystallites are so small that they contain only a few planes in phase, diffraction by these planes is no longer valid for producing sharp diffraction minima. In general, reduction in crystallite size affects the broadening of the peaks. Therefore, the broadening of the peak depends on the particle size. The particle size was determined from the broadening of X-ray diffraction peaks using the Scherrer's [134]**Equation 3.4**.

$$D = \frac{0.9 \lambda}{\beta \cos\theta} \quad (3.4)$$

Where 'D' is the crystallite size (Å), 'λ' is the X-rays wavelength, 'β' is the Full width at half maxima (FWHM) and 'θ' is the diffraction angle.

For the current work, the orientation and crystallinity of P3HT thin films irradiated with 90 MeV Ni<sup>7+</sup> ions, were characterized by Panalytical X'pert PRO X-ray diffractometer with a Cu-K<sub>α</sub> ( $\lambda = 0.154$  nm) monochromated radiation source, operating at a voltage of 40 kV and 40 mA current. XRD data were collected at a glancing angle of 3° and by varying  $2\theta$  in the range of 3-30° with a step size and exposure time of 0.02° and 1.5 s/step, respectively.

High-resolution X-ray diffraction (HR-XRD) patterns of 55 MeV Si<sup>4+</sup> irradiated P3HT thin films were measured at Elettra Synchrotron Lab, Trieste, Italy in MCX beam line at a glancing angle of 0.5°. The energy of the X-rays was 12 keV with a wavelength of 1.033 Å. The  $2\theta$  is varying in the range of 2 to 10° with a step size and exposure time of 0.01° and 1 s/step, respectively.

### 3.4.2. Fourier transform infrared spectroscopy (FTIR)

The infrared (IR) spectroscopy is the most promising characterization tool which, is based on the interaction of electromagnetic radiation and chemical substance. This technique provides the possibility of the identifying chemical bonds (functional groups), organic molecules and the molecular structure of the organic compounds without lengthy evolution methods. The IR spectroscopy technique is based on the vibrations of atoms in a molecule and provides a qualitative analysis. Every molecule consists the covalent bonds; these bonds are not rigid and can be bent or stretched. There are various type of molecular vibrations and are illustrated in **Figure 3.7**.

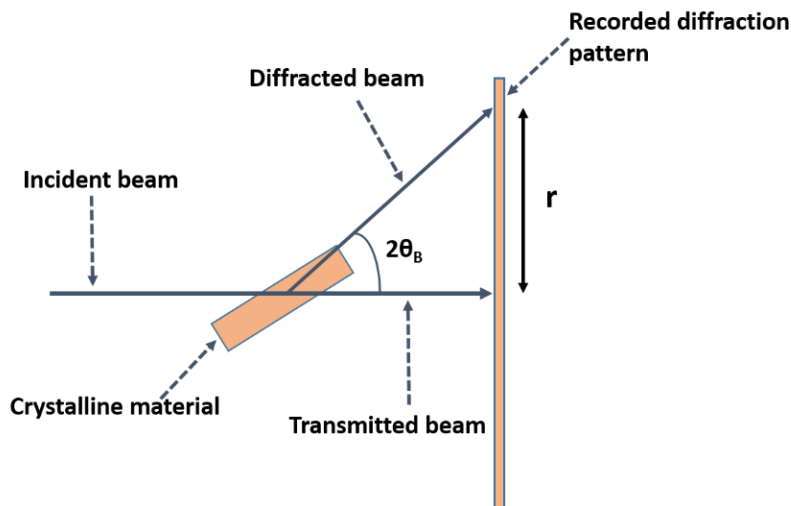


**Figure 3.6:** Conventional layout of XRD instrument.

**Figure 3.8** is showing a conventional setup of FTIR spectroscopy. When, IR irradiations are passing through the material, a part of IR radiations are absorbed by the sample and remaining part is transmitted. The wavelength of absorbed IR radiation is characteristics of stretching/ bending vibrational modes of a chemical bond. This occurs because the incident radiation induces an oscillating dipole moment in the molecule with a frequency equal to the frequency of the radiation. The secondary radiation emitted by the oscillating dipole then interact with the oscillating electric field of electromagnetic radiation resulting in an absorption on resonance. The resulting spectrum represents the molecular absorption and transmission. The resultant spectrum is the molecular fingerprint of the sample and absorption peaks are describing the frequency of vibrations between the bonds of the atom. The IR spectra cannot be similar for two different components because every material has its own unique combination of atoms. The determination of frequencies at which the samples absorbs the IR radiations allows the identifications of the chemical structure of the sample, since functional groups are known to absorb radiation at specific frequencies. The amount of present material can be estimated by the size of the peak in the spectrum.

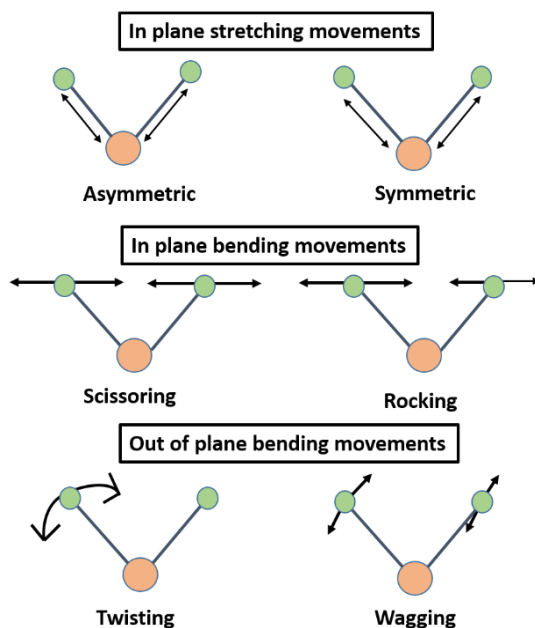


**Figure 3.7:** Different vibrational modes of a molecule.



In the present work, the FTIR spectra of pristine and irradiated thin films of P3HT and PCBM using both, 90 MeV Ni<sup>7+</sup> ions and 55 MeV Si<sup>4+</sup> ions, on double side polished silicon substrates were monitored in a FTIR spectrometer (Perkin Elmer model L1600401).

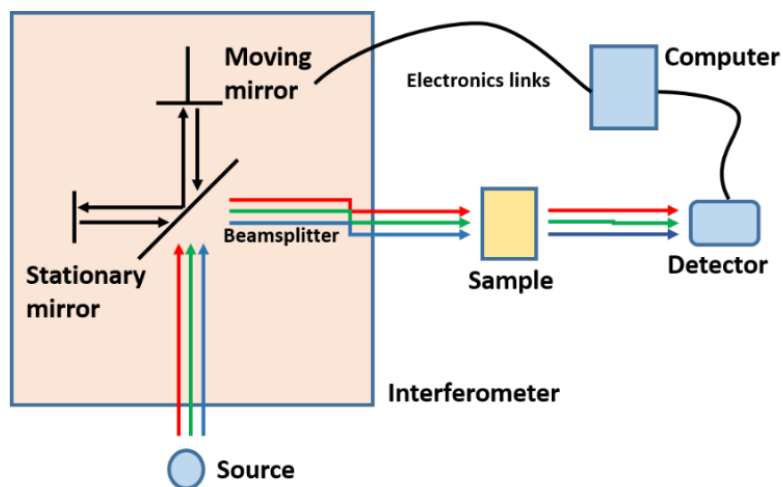


**Figure 3.8:** Block diagram of FTIR Instrumentation.

### 3.4.3. UV-visible absorption spectroscopy

UV-visible spectroscopy is one of the powerful analytical tools in the material science. When, an atom or molecule absorbs the energy, the electrons are promoted from their ground state to an excited state. The absorption of different substances between the wavelength ranges from 200-800 nm is investigated using UV-visible spectroscopy provides information about electron energy jumps between the two distinct energy levels. Ultraviolet and visible photons are energetic enough to promote valence electrons to higher energy states in molecules and materials. It provides key information about the electronic transition and hence electronic structure of the material. The absorption spectrum is commonly presented as a graph of absorbance versus wavelength. The measured spectrum is continuous because of combination of overlapping lines due to superposition of rotational and vibrational transition on the electronic transitions and makes the absorption band wider (**Figure 3.9 (a)**). The various possible electronic transition in the organic molecule are shown in **Figure 3.9 (b)**.

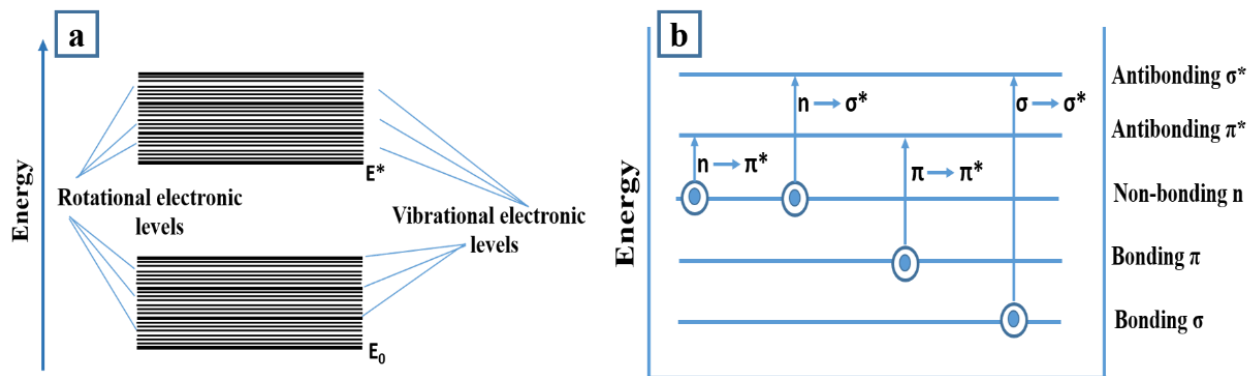


**Figure 3.9:** Diagram of electronic energy levels ( $E_0$  represents the ground state and  $E^*$  represents the excited state) (a); Energy level diagram for different electronic transitions (b).

The Beer-Lambert Law [135] described that absorbance is directly proportional to the path length in the solution, 'b', and the concentration, 'c', of the absorbing species.

$$A = -\log_{10} \left( \frac{I}{I_0} \right) = e \cdot b \cdot c \quad (3.5)$$

Where 'A' is the measured absorbance, ' $I_0$ ' is the intensity of the incident light at a given wavelength; 'I' show the transmitted intensity, 'e' is a constant of proportionality, called the molar absorptivity. **Figure 3.10** shows the schematic diagram of UV-visible spectrophotometer. In UV-visible spectroscopy, two radiation sources, deuterium lamp and tungsten halogen lamp, are used. The purpose of using two type of lamps is to cover the wavelength range from 200-800 nm of the spectrum. During the operation in the visible range, mirror M1 blocks the radiation coming from deuterium lamp and reflects the radiation coming from halogen lamp onto the source mirror M2. When, the operation is in UV range, mirror M1 allows the radiation is coming from deuterium lamp to strike source mirror M2. Radiation are reflected from the source mirror M2 through an optical filter wheel assembly. An appropriate optical filter is located in the beam path which is doing pre-filtration of the radiation before entering to the monochromator to produce the desired wavelength. The filter and radiation source will change automatically during monochromator slewing. The filtered radiation passed through the entrance slit (S1) of monochromator grating and dispersed to produce a spectrum. The selected portion of spectrum by the grating is reflecting through the exit slit (S2) to mirror M3. The slit S2 restricts the part of spectrum to a near monochromatic radiation beam and provide spectral band pass of 1 nm. The radiation is reflected from mirror M3 onto a beam splitter. This

splitter allows to pass 50 % of total radiation onto plane mirror M4 and remaining 50% radiation reflects onto plane mirror M5. Mirror M4 and M5 focus the radiation beam in the sample cell and reference cell, respectively and the beam passes through a convex lens onto the photodiode detector. The intensity of reference beam which, should have no absorption of light is denoted as 'I<sub>0</sub>' and the intensity of sample beam is defined as 'I'. If any sample does not absorb the light of a given wavelength then I=I<sub>0</sub>. However, if the sample absorbs light then I is less than I<sub>0</sub> and the ratio of I and I<sub>0</sub> is plotted on a graph as a function of wavelength. Absorption may be presented as transmittance (T = I/I<sub>0</sub>) or absorbance (A = log I<sub>0</sub>/I). If absorption is not occurring then T = 1.0 and A = 0.

The bandgap can be determined using Tauc's relation [136] for a semiconductor:

$$\alpha h\nu = A (h\nu - E_g)^n \quad (3.6)$$

Where 'α' is the absorption coefficient, 'hν' is the photon energy; 'A' denotes the density of localized state constant and 'E<sub>g</sub>' shows the energy bandgap. The index value "n" depends on the transition. For direct allowed and direct forbidden transition 'n' has the values of 1/2 and 3/2 respectively. When, transitions are indirect allowed and indirect forbidden transition, 'n' will be 2 and 3 respectively. The value of E<sub>g</sub> can obtain by extrapolation of the straight line portion of the absorption edge to the abscissa (hν).

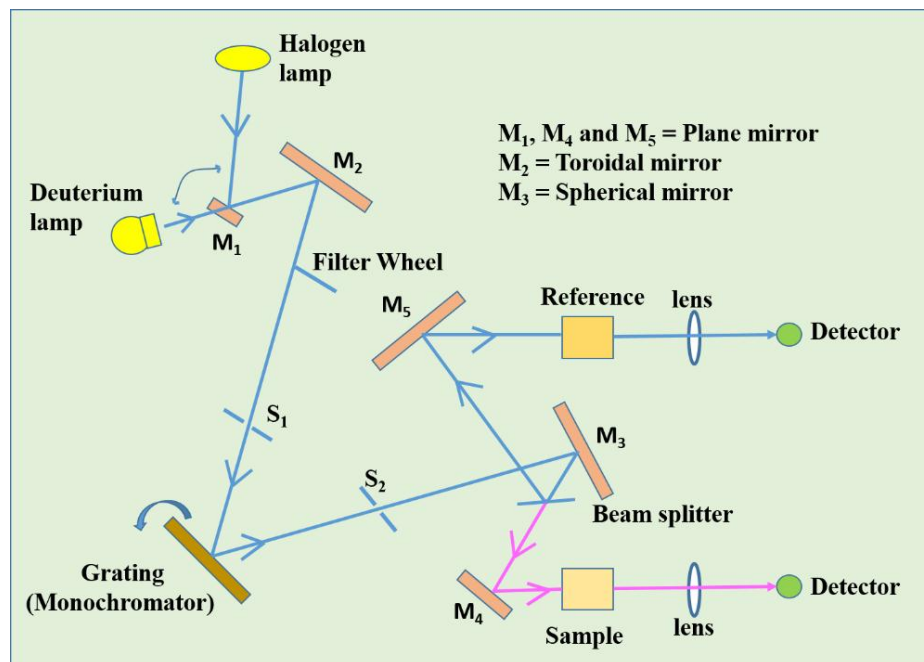


**Figure 3.10:** Schematic diagram of UV-visible spectroscopy.

In the present work, the absorption spectra of pristine and irradiated P3HT and PCBM thin films (using 90 MeV Ni<sup>7+</sup>, 55 MeV Si<sup>4+</sup> and 1400 KeV Xe<sup>5+</sup> ion beams) were obtained using a Hitachi U-3300 spectrophotometer.

### 3.4.4. Raman spectroscopy

To study the vibrational, rotational and other low-frequency modes in chemistry and condense matter physics, the Raman spectroscopy technique is used. Raman is a non-destructive technique and required no sample preparation. It can be used for both quantitative and qualitative analysis. This technique is based on the Raman Effect which was introduced by Indian Physicist, C. V. Raman in 1928 [137]. Raman Effect is the inelastic scattering of photons by molecules. The transitions between the energy states are induced by the interaction of photons with molecules and most of the photons are elastically scattered i.e. Rayleigh scattering. In Rayleigh scattering, the emitted photons and the absorbing photons have the same wavelength. The energy of incident and scattered photons are different in Raman scattering. If the scattered radiation has the energy less than the incident radiation, it is called Stokes line (Stokes radiation). While, the scattered radiation having the energy more than the incident radiation is called anti-stokes line (anti-stokes radiation) [138]. An energy level diagram of all type of scattering is showing in **Figure 3.11**.

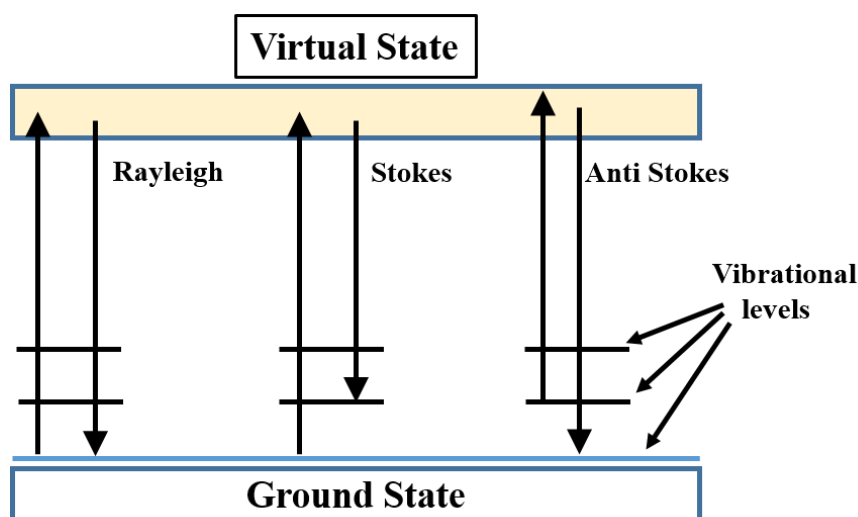


**Figure 3.11:** Energy level diagram of Rayleigh scattering, Stokes Raman scattering and Anti-stokes Raman scattering.

Excitation instigates the scattering of the radiation and enhancement or reduction in the energy of scattered radiations is associated with the spacing of vibrational energy levels in the ground state of the molecules. Therefore, the vibrational energy of the molecule can be measured by the energies of Stokes and anti-Stokes lines. Both, Stokes and anti-Stokes lines are situated at an equal distance from Rayleigh line because either vibrational quantum of energy is gained or lost. The intensity of anti-Stokes line is lesser than Stokes line because for anti-Stokes line the molecule should be in the excited state. Hence, the intense Stokes line is measured by Raman spectroscopy. A change in polarizability during molecular vibration is an essential requirement to obtain Raman spectrum of the sample.

In Raman experiment (**Figure 3.12**), a laser is used to illuminate the sample because it provides a coherent beam of monochromatic light. This incident light excites the photons and gives sufficient intensity to produce scattered photons. The exciting laser is injected into an optical microscope using a beam splitter and focused on the sample by an objective. The scattered light is collected, led to the beam-splitter and into the spectrometer. These scattered photons are separated by incident wavelength by passing through a transmission grating. The intensity of Raman signal is recorded at each wavelength using CCD detector. An almost real-time graph can be obtained using CCD detector and also it can take more data in a given time.

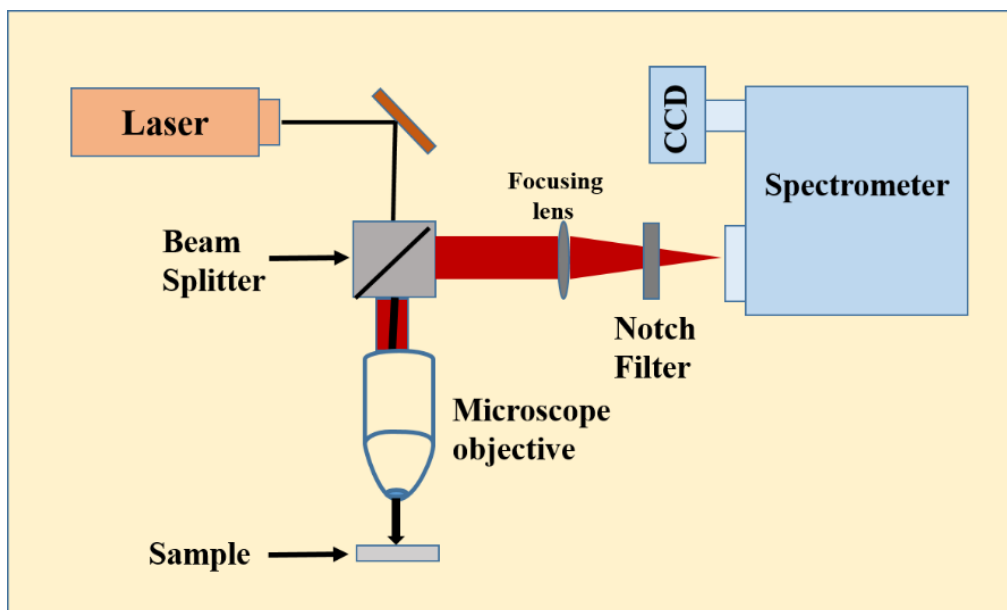


**Figure 3.12:** Block diagram of micro-Raman scattering experiment.

For the present work, the micro-Raman spectra for both pristine and 90 MeV Ni<sup>7+</sup> ion irradiated P3HT thin films were recorded in a Renishaw InVia Raman microscope by exciting with the 514 nm line of an Ar laser. A laser spot size of ~4-5 μm was used during micro-Raman measurements and by keeping power on the sample surface below 5 mW to avoid heating effects. While, for the P3HT sample irradiated using 55 MeV Si<sup>4+</sup> ion beam, Raman spectra were recorded from STR 500 confocal micro-Raman spectrometer with an excitation of 532 nm laser. The laser power on the sample surface was maintained at 0.2 mW.

The Raman spectra of PCBM thin films irradiated with 55 MeV Si<sup>4+</sup> ion beam were recorded using STR 500 confocal micro-Raman spectrometer with an excitation of 532 nm laser and power ~1 mW.

#### **3.4.5. Photoluminescence (PL):**

When, a radiation of certain frequency is incident on a molecule, it gets excited and may come back to its initial state with an emission of radiation with a lower frequency than that of the incident radiation. This mechanism is known as '*Luminescence.*' When, the emission of radiation stops as the incident light is removed, the phenomenon is called *fluorescence*. Whereas, if the emission persists longer time after removing the incident light, this phenomenon is called *phosphorescence*.

Photoluminescence (PL) is a very common emission spectroscopy characterization technique to study the properties of nanomaterial. This technique is very simple, sensitive, contact-less and non-destructive. The experimental apparatus of PL simply consists of a laser which, irradiates the sample and the emitted light or luminescence is analysed by a monochromator [139]. The incident light ionizes the filled levels of the sample caused in the raising of the electron and holes concentration in the conduction and valence bands. This raised concentration creates higher level excitons in quantum wells and higher energy levels of the band structure are increasing. Electron and holes are continuously recombining after getting a new equilibrium with incident light which is pumping the various levels of the band structure. The released energy (as photons) during the recombination is measured by the monochromator and detector. In short, in PL experiment, a single laser light is used to pumping the energy levels of the sample and the emitted light

is measured. From the frequency of emitted light, the information of energy level transitions is measured directly. An example of the slow process is shown in **Figure 3.13**.

In the present study, the emission spectra were recorded by exposing the P3HT samples (for both 90 MeV Ni<sup>7+</sup> and 55 MeV Si<sup>4+</sup> ion beam irradiated) to solid state laser with excitation wavelength 532 nm at room temperature using STR-500 Raman spectrophotometer.

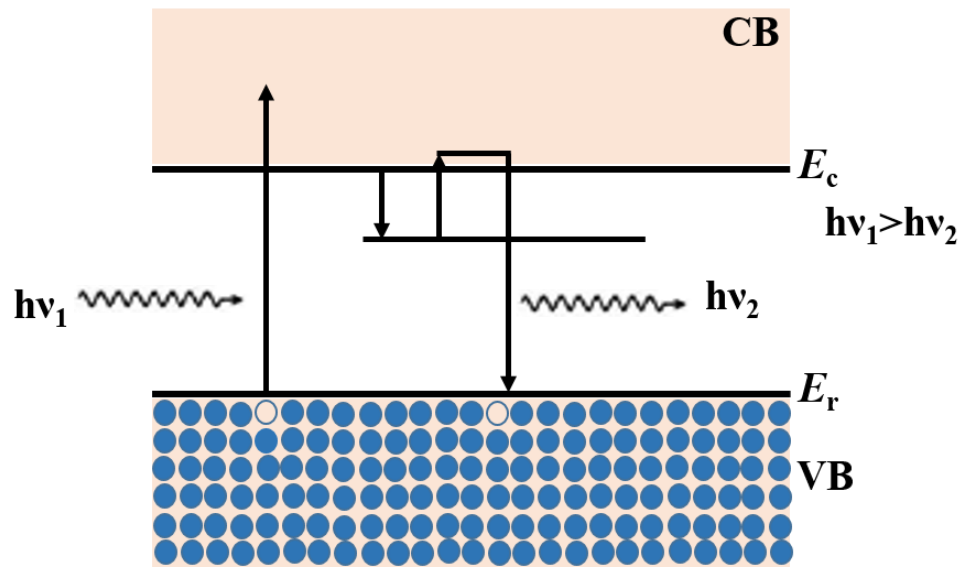


**Figure 3.13:** Schematic of Photoluminescence process.

#### 3.4.6. Atomic force microscopy (AFM)

The AFM was developed by Gerd Binnig, Calvin Quate and Christoph Gerber in 1986 [140]. The AFM works on the principle of attractive or repulsive forces between a tip and the sample. The forces measured in AFM include Van der Waals force, capillary forces, chemical bonding, electrostatic forces, magnetic forces, Casimir forces, solvation forces etc. depending on sample medium and approach distance of the tip. The Van der Waals force is the dominant force in AFM. It is also using to obtain the images of the surface at the atomic scale. When, the probe tip of AFM scanned the sample surface and distance between them remains within a few nanometer, the force between the tip and the sample cause it to deflect. This deflection is measured and correlated to the force. A block diagram of AFM setup is shown in **Figure 3.14**. AFM has a micro-scale cantilever made up of

silicon nitride or silicon. The cantilever has a sharp tip whose radius of curvature is in the order of nanometer. During the measurement, when, the probe tip comes into contact with the sample surface, a force will produce between the sample surface and probe tip. The cantilever will deflect and bend because of the force between sample and tip. This force (F) can be calculated using the following Hooke's law, where deflection of the cantilever is measured.

$$F = -kz \quad (3.7)$$

Where 'k' shows the stiffness of cantilever and 'z' denotes the distance of lever bent. A piezoelectric stage is used to mount the samples. To analyze the sample surface, probe tip is scanned laterally and deflection of the cantilever is measured as a function of position. There are three modes in which, AFM can be operated.

- a) *Contact mode*: In this mode, the probe tip is in intimate contact with the surface. When, the tip scanned across the surface and encountered with surface corrugations, the tip is deflected.
- b) *Constant force mode*: In this mode, the distance between the probe tip and sample surface is adjusted continuously to maintain a constant deflection, and therefore constant height above the surface.
- c) *Tapping mode*: In this type of mode, a stiff cantilever and sample surface brought into proximity. Then the cantilever starts to oscillate resulting in a change in the amplitude or resonant frequency of the cantilever. This change is measured during the scan. When, the cantilever oscillates, a part of tip discontinuously taps the surface of the sample. To use this mode, the cantilever should be very stiff so that cannot be stuck on the sample surface. This mode is useful for soft samples because of improved lateral resolution. The lateral forces such as drag in contact mode are virtually eliminated in tapping mode.



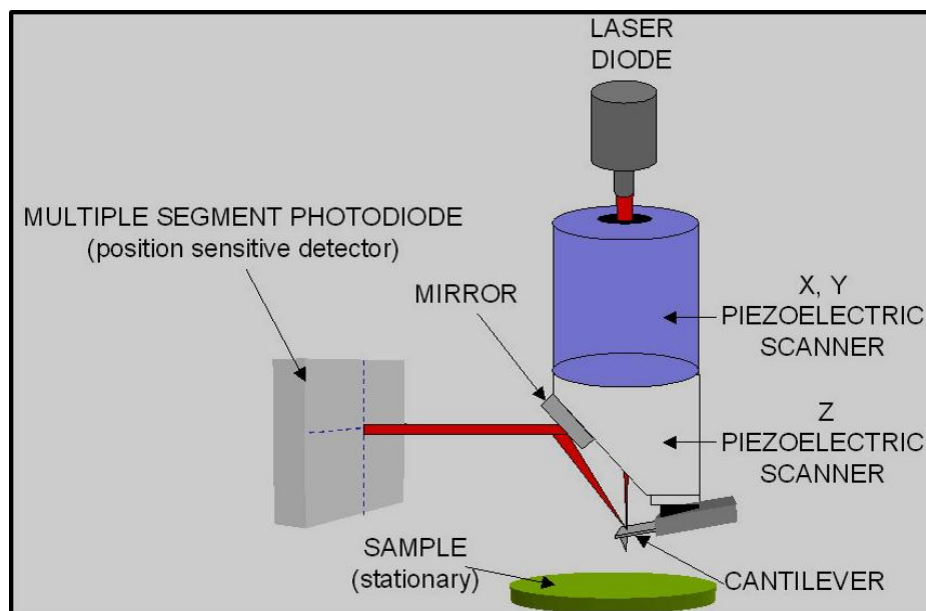


**Figure 3.14:** Block diagram of Atomic force microscopy.

The size and stiffness of the cantilever are sensitivity factors for the force measurements. The main advantage of using AFM is precision, higher resolution and less damage. AFM is also having the ability of functioning as a current, physical, chemical and biosensors [140]. Various type of surfaces such as organic, biological, insulators or conductors can image using AFM.

For the present work, the RMS roughness of pristine P3HT and PCBM thin films as well as after irradiating by both 90 MeV  $\text{Ni}^{7+}$ , 55 MeV  $\text{Si}^{4+}$  and 1400 KeV  $\text{Xe}^{5+}$  ion beams, were measured using Bruker Nano 5 AFM setup using tapping mode.

### 3.4.7. Contact angle measurement

Wetting of solid substrates by the liquid is a fundamental phenomenon having significant importance in both the technological and natural world. The solid-liquid interfacial phenomenon (wettability) is often characterized by measuring the contact angle formed between a solid surface and a liquid drop. Contact angle measurement is a sensitive and relatively simple tool to evaluate hydrophilicity or hydrophobicity of any surface. The surface heterogeneity, line tension, roughness of any surface and solid surface energy [141] can also determine using this measurement. The wetting characteristic of any solid surface

is dependent on intermolecular forces those are responsible for the contraction of the surfaces which is known as surface tension.

When, a liquid droplet put on an even solid surface as shown in **Figure 3.15**, the intersection of liquid-vapour and liquid-solid interfaces formed an angle called the contact angle ( $\theta_c$ ). The contact angle can be acquired geometrically by drawing a tangent line along the liquid-vapour interface from the contact point. The junction where solid, liquid, and vapor phases are coincide is known as the three-phase contact line. As shown in **Figure 3.15**, measured contact angle will be small if the liquid is spreading on the surface. While, a large contact angle is observed when, the liquid beads on the surface. More precisely, when,  $\theta_c$  is less than  $90^\circ$ , it indicates that surface wetting is favorable. When,  $\theta_c$  is greater than  $90^\circ$ , it indicates the spreading of fluid over a large area on the solid surface (wettability unfavorable).

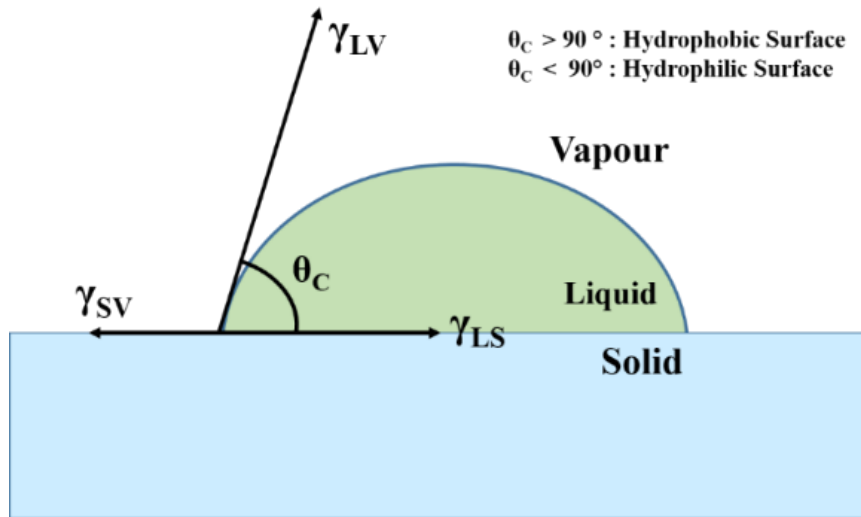


**Figure 3.15:** Illustration of contact angles formed by liquid drop on a smooth homogenous solid surface.

The contact angle described by using Young's equation. Thomas Young theoretically described that the contact angle of liquid depends on the interfacial energy (surface tension) of the liquid- vapour, solid- vapour and solid-liquid interfaces when, these phases are in thermodynamics equilibrium. By the Young's equation, with the assumptions that the drop size is small and gravity effect (which deform the droplet) is negligible [142], the contact angle between a liquid drop and solid surface can be described using **Equation 3.8:**

$$\cos \theta_c = \frac{\gamma_{SV} - \gamma_{LS}}{\gamma_{LV}} \quad (3.8)$$

Where  $\gamma_{SV}$ ,  $\gamma_{LS}$  and  $\gamma_{LV}$  are surface tension at the interface of solid-vapour, liquid- solid and liquid- vapour, respectively and  $\theta_c$  is the contact angle [143]. This model is based on the assumption of considering the surface to be flat and homogenous.

For the present work, the surface wettability of water droplets before and after irradiation of P3HT and PCBM thin films were examined using Contact angle measurement system from KRUSS drop shape analysis setup. The angle was estimated using sessile drop fitting method using the software.

### 3.4.8. X-ray photoelectron spectroscopy (XPS)

Photoelectron Spectroscopy is based on collection and energy analysis of photoelectrons emitted upon illumination of radiation onto the samples. When, X-ray radiation is using, it is called X-ray photoelectron spectroscopy (XPS). XPS was developed in the mid-1960s by Kai Siegbahn and his research group at the University of Uppsala, Sweden. In 1981, Siegbahn was awarded the Nobel Prize in physics for his work with XPS. This technique was initially known as Electron spectroscopy for chemical analysis (ESCA).

To make surface analysis by XPS, the sample is irradiated with monochromatic soft X-rays i.e. X-rays of known energy ( $h\nu$ ) and electron are ejected from the sample surface. These electrons are having the binding energy (BE)  $E_b$ , which is less than the energy of incident X-rays ( $E_b < h\nu$ ). The energy of these ejected electrons is detected. Al  $K_\alpha$  (1486.6 eV) and Mg  $K_\alpha$  (1253.6 eV) are most commonly used X-ray sources. The incident photons have limited penetration depth. These photon interacts with the atoms in the surface region and causing electrons to be emitted by the photoelectric effect. These emitted electrons having kinetic energy (KE)  $E_k$  which, can be measured in the spectrometer and is given by:

$$E_k = h\nu - E_b - \Phi_{sp} \quad (3.9)$$

Where  $\Phi_{sp}$  is work function of the spectrometer. Since, by compensating for the work function term electronically, it can be eliminated.

$$E_k = h\nu - E_b \quad (3.10)$$

$$E_b = h\nu - E_k \quad (3.11)$$

Thus, by measuring the KE of photo-electrons, **Equation 3.11** can be used to translate this energy into BE of the electrons. The BE is referred as the energy difference between initial and final state after emission of photo electron. XPS can determine the concentration of the elements present at the surface using BE information. Dissimilarity in the polarizability of compounds and chemical potential are the main cause of the chemical shift (variation in elemental BE).

**Figure 3.16** is a schematic diagram of the essential components necessary for performing XPS. An X-ray source to produce X-rays, an electronic energy analyser, a sample holder, an electron detector/multiplier and suitable electronics for readable spectrum are some components those are consist by any XPS setup [139]. Ultra high vacuum (UHV) is maintained inside the setup. Along with the BE data and elemental identification, XPS can also provide more spectral information such as spin-orbit splitting, chemical shifts, auger-chemical shifts, shake-up lines, plasmon loss lines. XPS also provide the chemical state identification, quantitative analysis, useful to determine element location or depth profiling.

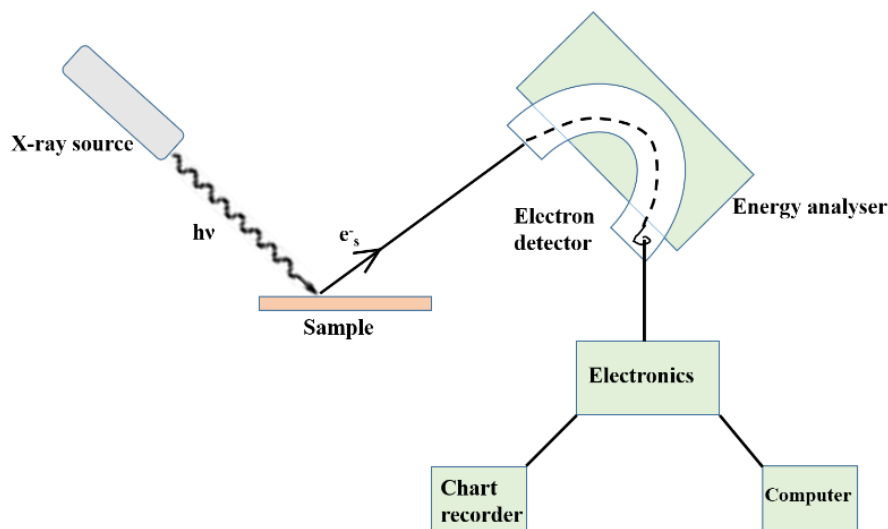


**Figure 3.16:** Schematic representation of the necessary components for XPS.

Electronic properties of P3HT thin films irradiated using 90 MeV Ni<sup>7+</sup> and 55 MeV Si<sup>4+</sup> ion beams were measured in an Omicron nanotechnology XPS system from Oxford instruments (model-ESCA+) consisting of an UHV chamber attached with a

monochromatic Al-K<sub>α</sub> radiation source of energy 1486.7 eV and a 124 mm hemispherical electron analyzer.

#### **3.4.9.DC conductivity measurement:**

DC conductivity is the form of electrical conductivity measurement that most of us are familiar with. For the conductivity measurement, two methods are possible: Two probe method and four probe method. For present work, two probe method was used. In the two probe method, the sample is simultaneously contacted in two places and conductivity is measured. In a DC conductivity measurement process, in principle current from a DC source should flow through the sample and the potential difference that develops across the sample must be measured. The resistance of the sample is measured using the Ohm's law. Further, to measure the conductivity of the sample, Ohm's law can be written as follows:

$$V = IR \quad (3.12)$$

Where 'V' is the potential difference across the sample when, the current 'I' is flowed through it. After calculating the values of resistance 'R', the resistivity of the sample can be calculated using the following formula:

$$\rho = \frac{RA}{l} \quad (3.13)$$

Where 'ρ' is the resistivity of the sample, 'l' is the length of the sample, and 'A' is the cross-sectional area of the sample. We will assume that the length and cross-sectional area of the sample is uniform and are therefore each of a single value. The conductivity (σ) of the sample is then simply the inverse of the resistivity and can be calculated as:

$$\sigma = \frac{1}{\rho} \quad (\text{unit: } \Omega^{-1}\text{m}^{-1}) \quad (3.14)$$

To study the variation of conductivity with temperature, R-T measurement is performed which described the charge transport/hopping phenomenon with the variation of temperature (both high and low temperatures). The two probe method is used to carry out the measurement. The samples were mounted on a substrate holder and the two probe connections (contacts with the sample) are made using silver paste over the thin films. A very thin copper wire is used to make probes and the distance between both probes was kept minimum and constant during the measurements to avoid the contact resistance. After

drying the silver contacts, a rough vacuum was maintained in the substrate holder. This holder was dipped into a container which was filled with liquid nitrogen ( $N_2$ ). The temperature was controlled using a temperature controller (Lakeshore temperature controller 325) during the whole measurement. The resistance was measured using Keithley's 6517-B electrometer. The whole setup is interfaced to a computer with lab-view programming for controlling and monitoring of real-time measurement. The whole setup is showing in **Figure 3.17**. The user can select sourcing mode (current/voltage), compliances, output level (sourcing amplitude) for measurements and delay in measurement. The front panel shows the real-time voltage, current, temperature, resistance values and plot between resistance and temperature which updates after each delay time.

For the present work, the dc conductivity measurement for pristine and irradiated P3HT thin films (using 90 MeV  $Ni^{7+}$  and 55 MeV  $Si^{4+}$  ion beams) in the variable temperature range was carried out by two probe method using Keithley's electrometer 6517B and Lakeshore temperature controller 325. The vacuum in the sample holder during the measurement was  $10^{-3}$  Torr.

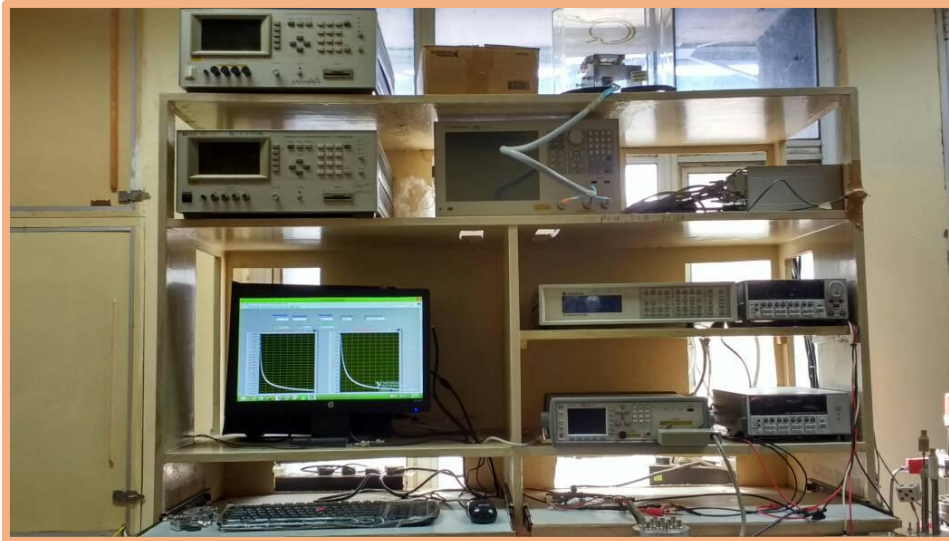


**Figure 3.17:** Image of R-T measurement setup at IUAC, New Delhi.

# **Investigations on Modifications in P3HT Thin Films with Electronic Excitation by Taking Different Mass and Energy**

#### ***4.1 Ion irradiation induced modifications of P3HT by 90 MeV Ni<sup>7+</sup> ion beam***

P3HT as a semi-crystalline polymer is efficiently used as light absorbing and hole transporting layer. In semiconducting polymeric materials, the ordering of molecules has a remarkable effect on their optoelectronic properties. The P3HT thin films can show the higher degree of molecular ordering via  $\pi$ - $\pi$  stacking of adjacent molecules [144]. This high degree of molecular ordering is an important step for enhancing the photon absorption at a longer wavelength and increased charge carrier mobility [76][145][146]. High energy ion beams are very useful tool to modify the properties of material in a controlled manner for specific applications [108][147][84][148]. Nanoscale molecular structures can also be modified by high energy ions, leading to the change in chemical, structural and optical properties. When, such energetic ions pass through the polymer film, they can transfer their energy to the molecules which, lead to the ionization and excitation of the atoms and/or molecules. These modifications in the polymer are associated with the bond cleavages and production of free radicals. These radicals are responsible for chemical transformation in polymer via chain scission, cross-linking and bond breaking/formation. High energy ion irradiation produces several intra-chain or inter-chain modifications in polymers.

Under this study, thin films of P3HT, deposited using spin coating method on glass and double side polished substrates, were irradiated by 90 MeV Ni<sup>7+</sup> ions using Pelletron accelerator available at IUAC, New Delhi. The beam was incident at normal to the film surface to carry out the irradiation process with different fluences ranging from  $1 \times 10^9$  to  $1 \times 10^{11}$  ions/cm<sup>2</sup>. The  $S_e$  and  $S_n$  for the 90 MeV Ni<sup>7+</sup> ions in P3HT matrix is 4788 eV/nm and 8.39 eV/nm, respectively. The range of Ni<sup>7+</sup> ions is 26.89  $\mu$ m calculated by SRIM 2008 programme.

#### ***4.1.1. Results and discussion***

##### ***4.1.1.1. Micro-Raman spectroscopy***

**Figure 4.1** shows the typical micro-Raman spectrum of pristine P3HT film. There are several Raman modes of P3HT (**Table 4.1**) observed in the range of 600-1800 cm<sup>-1</sup> [149][150]. The Raman bands for pristine P3HT found at 1380 and 1449 cm<sup>-1</sup> are supposed to be sensitive to  $\pi$ -electron delocalization or conjugation length of P3HT molecules [151][152]. But the peak position corresponding to C-C mode (1380 cm<sup>-1</sup>) is insensitive to



both excitation wavelength and molecular ordering [152]. So the main focus is only on C=C mode at  $1449\text{ cm}^{-1}$ .

**Figure 4.2** shows the micro-Raman spectra of pristine and ion beam irradiated P3HT films with fluences from  $1\times 10^9$  to  $1\times 10^{11}$  ions/cm<sup>2</sup>. It depicts that the intensity corresponding to C=C mode increases with an increase in fluence from  $1\times 10^9$  to  $1\times 10^{10}$  ions/cm<sup>2</sup>. With further increase in fluence upto  $1\times 10^{11}$  ions/cm<sup>2</sup>, the peak intensity is reduced with respect to the intensity of the peak at  $1\times 10^{10}$  ions/cm<sup>2</sup>. **Figure 4.3** shows the variation of FWHM with fluences (**Figure 4.3-a**), while, a variations of the peak height and the normalized areal intensity with fluences are exhibited in **Figure 4.3-b and c**, respectively. As discerned from **Figure 4.3-b and c** that the peak height and normalized areal intensity for  $1449$  and  $1380\text{ cm}^{-1}$  modes are initially enhanced with increasing ion fluence upto  $1\times 10^{10}$  ions/cm<sup>2</sup>. After  $1\times 10^{10}$  ions/cm<sup>2</sup>, when, ion fluence is increased upto  $1\times 10^{11}$  ions/cm<sup>2</sup>, the peak height and areal intensity starts decreasing. The variation of FWHM corresponding to  $1449\text{ cm}^{-1}$  peak (**Figure 4.3-a**) shows that the FWHM is decreasing upto the fluences of  $1\times 10^{10}$  ions/cm<sup>2</sup> but after that when, fluences increases at  $1\times 10^{11}$  ions/cm<sup>2</sup>, the FWHM starts increasing. This decrease in the FWHM shows the increment in the molecular ordering of P3HT corresponding to C=C mode [153].

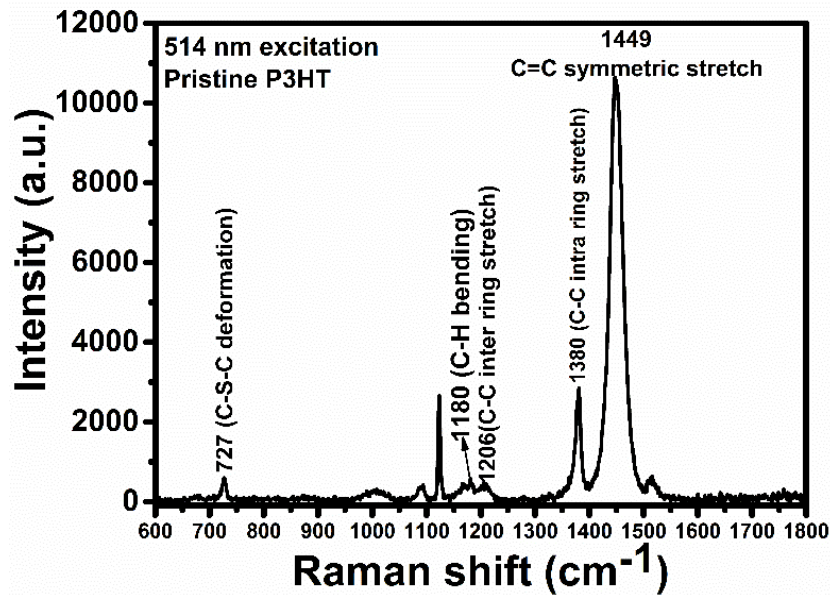


**Figure 4.1:** Raman spectrum of pristine P3HT thin film under 514 nm excitation.

**Figure 4.4** shows the change of relative areal intensity ratio of C-C mode to C=C mode ( $I_{C-C}/I_{C=C}$ ) with different fluences. The relative areal intensity ratio for the pristine films of P3HT was 0.079. The variation in the relative intensity shows that the ratio  $I_{C-C}/I_{C=C}$  initially increases up to 0.092 with the increase in fluence upto  $1 \times 10^{10}$  ions/cm<sup>2</sup>. With further increase in fluence ( $>1 \times 10^{10}$  ions/cm<sup>2</sup>), the relative ratio decreases and reaches upto 0.069. The ordered P3HT can be quantified by a narrower FWHM of C=C mode and the large intensity ratio of C-C mode with respect to the C=C mode [152][153]. These significant changes in FWHM of C=C mode and  $I_{C-C}/I_{C=C}$  ratio confirms the molecular ordering of P3HT with ion irradiation. The variation in FWHM and relative areal intensity ratio  $I_{C-C}/I_{C=C}$  with fluences is shown in **Table 4.2**.

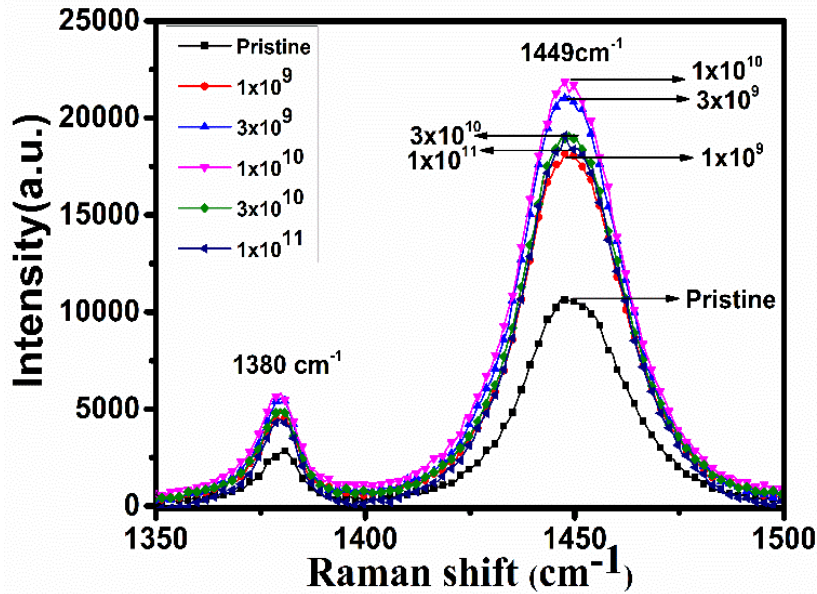


**Figure 4.2:** Raman spectra of pristine and 90 MeV Ni<sup>7+</sup> ion beam irradiated thin films of P3HT.

The molecular ordering of P3HT at lower fluence and again disordering at higher fluence can be understood by ion polymer interaction. When, high energy ion beam interacts with the target material, initially they transfer their energy to the electronic subsystem of the target material by inelastic collision within the duration of  $10^{-15}$ - $10^{-14}$  s. Subsequently, this energy is transferred to the atomic subsystem via electron-phonon (e-p) interaction, which occurs at a time scale of  $10^{-13}$ - $10^{-12}$  s. This process leads to a sharp increase in the lattice

temperature upto few thousands of Kelvin. Beyond a certain threshold value of electronic energy loss (Se), a transient molten state is formed in the material within a few nanometer range radially from the ion path. This molten state remains for a very short duration of  $10^{-12}$  -  $10^{-11}$  s and quenches rapidly at a rate of  $10^{14}$  K/s by thermal conduction. This process which is so called 'thermal spike model' [154][85] creates a modified material in the cylindrical region around the ion path. So when, the thin films of P3HT were irradiated at fluence  $1 \times 10^9$  ions/cm<sup>2</sup>, these high energy ions passes through the film, lose its energy and excite the target material. This energy is transferred within few nm cylindrical region around the ion path and creates a high-temperature zone. This region of high temperature quenches very fast i.e. within a picosecond. It has been shown in the literature [155] that during the passage of ion in material, the temperature around the ion path follow the Gaussian distribution and decreases gradiently. The temperature gradient between the track core and halo region in various type of materials is well-studied phenomenon[156][157] and ordering in fullerenes, graphene and CNT etc. due to the annealing in the halo regions have already been studied in detail using this concept. A. Biswas et al. reported the recrystallization of PVDF with remarkable molecular structural engineering by halo region annealing effect with high energy ion beam at low fluences [158]. The heating effect around the ion path is shown in **Figure 4.5**.

The annular region surrounding the core of ion path has less heating effect than core region and can be assumed as annealing causing the molecular ordering of P3HT at low fluence. All the ion tracks are well separated at low fluences. With further increase in fluence above  $1 \times 10^{10}$  ions/cm<sup>2</sup>, the ordering decreases since at higher fluences ( $>1 \times 10^{10}$  ions/cm<sup>2</sup>) more and more ions pass through the film and get overlapped enhancing the temperature of the core region to a considerable extent. Over and above the overlapping fluence, the incoming ion will find themselves in a region of track halos created by the previous ions. Here it is important to mention that compare to the area of track core, halo regions are formed in much bigger areas of the target materials.

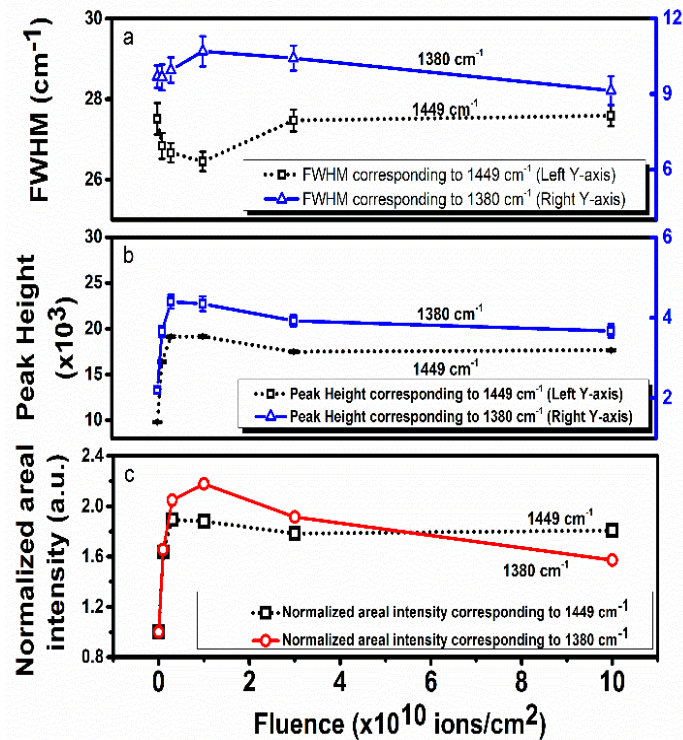


**Figure 4.3:** Variation of FWHM (a), peak height (b) and normalized intensity (c) corresponding to C=C mode (1449 cm<sup>-1</sup>) and C-C mode (1380 cm<sup>-1</sup>) with different fluences of 90 MeV Ni<sup>7+</sup> ion beam.

Track core part is generally of few nm in diameter whereas, track halo may extend upto micrometer region from the ion path depending on the material. So the ions which are coming after the overlapping fluence will create track core regions in the halo region of the previous ion. In these new track core regions, due to bond breaking, ordering of P3HT will start diminishing. Due to the high energy ion beam impact, free radicals, hydrocarbons etc. are released. The hexyl side chain may be detached during irradiation and thiophene ring is less affected by high energy ions in contrast to the side chain. So in the present case also, a small level of chain scission may also help to increase crystallinity due to increase in mobility of the chain but with increasing fluences, the liberation of gaseous fragments is also possible which, may lead to amorphization i.e. long molecular chains may be damaged but not destroyed completely due to ion impact at higher fluence and may result in disordering at higher fluences.

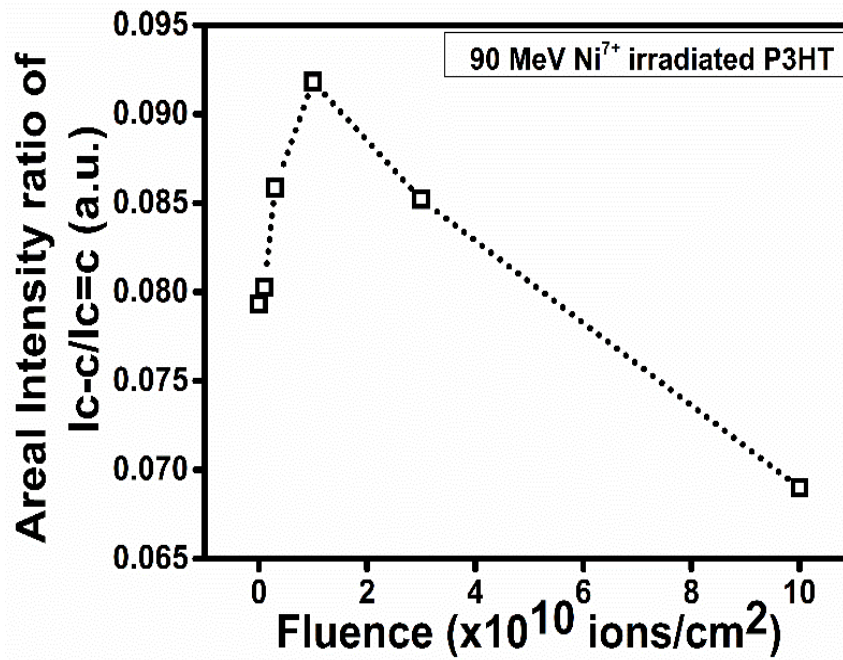


**Figure 4.4:** Represents the variation of relative areal intensity ratio of C-C mode to C=C mode ( $I_{C-C}/I_{C=C}$ ) with different fluences.

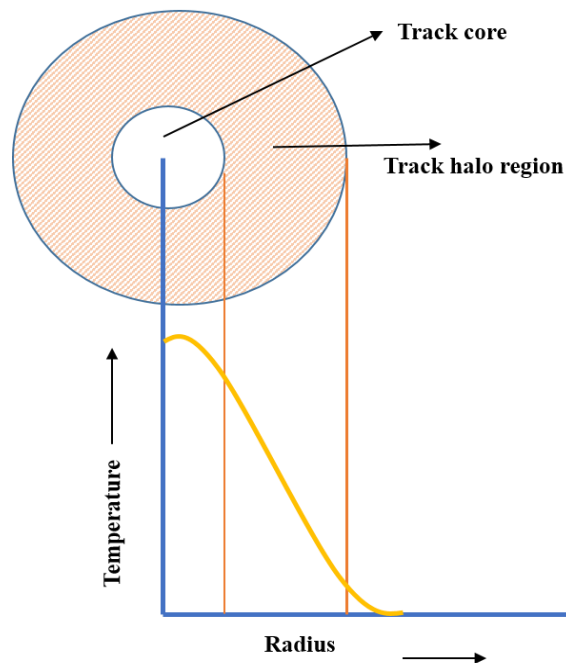


**Figure 4.5:** Schematic diagram of radial gradient of temperature around the ion path.

**Table 4.1:** Summary of modes of vibrations in pristine P3HT thin films at different wavenumbers for 514 nm excitation.

Wavenumber (cm <sup>-1</sup> )	Modes of vibration
1449 cm <sup>-1</sup>	The symmetric C=C stretching mode
1380 cm <sup>-1</sup>	The C-C intra ring stretching mode
1206 cm <sup>-1</sup>	The inter ring C-C stretching mode
1180 cm <sup>-1</sup>	The C-H bending mode with the C-C inter ring stretching mode
727 cm <sup>-1</sup>	The C-S-C deformation mode

**Table 4.2:** Summary of FWHM of C=C mode (1449 cm<sup>-1</sup>) and relative areal intensity ratio of the C-C mode to the C=C mode ( $I_{c-c}/I_{c=c}$ ) for pristine and 90 MeV Ni<sup>7+</sup> ion irradiated P3HT thin films at different fluences.

Fluence (ions/cm <sup>2</sup> )	FWHM (cm <sup>-1</sup> ) (C=C mode)	$I_{c-c} / I_{c=c}$
0	27.51	0.079
1×10 <sup>9</sup>	26.84	0.080
3×10 <sup>9</sup>	26.67	0.086
1×10 <sup>10</sup>	26.45	0.092
3×10 <sup>10</sup>	27.47	0.085
1×10 <sup>11</sup>	27.59	0.069

#### 4.1.1.2. FTIR spectroscopy

**Figure 4.6** shows the FTIR spectra of pristine and irradiated P3HT thin films which is similar as reported in the literature by other groups [114][115][102]. The observed band at 735 cm<sup>-1</sup> is corresponding to methyl rock and the band at 820 cm<sup>-1</sup> is attributed to aromatic C-H out of plane vibration which, confirms the regioregular structure of the P3HT in the present case. The polymer having each repeating unit is derived from the same isomer of the monomer is called regioregular polymer. Regio-regular polythiophenes having a uniform distribution of substituents contain Head to Tail (HT) coupling exclusively. They can acquire a planar conformation with low energy and extended  $\pi$ -conjugation (figure 1.4). The characteristic peak of thiophene has been observed at 1377 cm<sup>-1</sup> which is attributed to C-S stretching mode. It is clear from the figure that the band at 1458 cm<sup>-1</sup> is

associated with symmetric ring stretching vibrations and band at  $1510\text{ cm}^{-1}$  is associated with asymmetric C=C ring stretching vibrations.

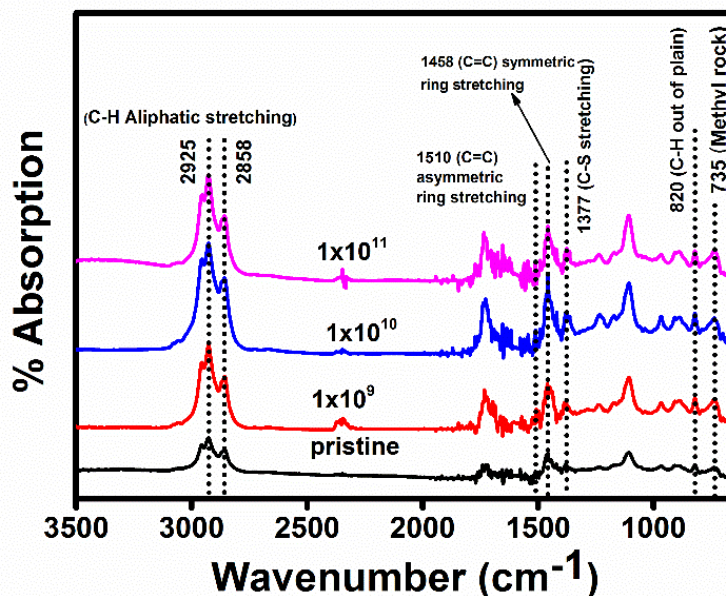


**Figure 4.6:** FTIR spectra of pristine and irradiated P3HT thin films.

The relative ratio of their intensity ( $I_{1510}/I_{1458}$ ) shows the conjugation length and for the present study this ratio increases from 0.03 to 0.8 for the  $1 \times 10^{10}$  ions/cm<sup>2</sup> fluence. The increased conjugation length due to the increased molecular ordering may also be the cause of increased conductivity [115]. The bands at  $2858\text{ cm}^{-1}$  and  $2925\text{ cm}^{-1}$  represent the C-H aliphatic stretching. As shown in **Figure 4.6**, the intensity of prominent bands is increased with increasing the incident ion fluences. The presence of all the modes of P3HT even at a fluence of  $1 \times 10^{11}$  ions/cm<sup>2</sup> confirms that the basic unit structure of P3HT molecule is not significantly altered after ion irradiation at low fluence. It has been reported for regioregular P3HT which, consists self-packing of the hexyl side chains by hydrophobic interaction, due to the ion irradiation at the fluence of  $1 \times 10^{11}$  ions/cm<sup>2</sup>, the self  $\pi$  stacking of thiophene rings between the adjacent polymer chains may lead the chain reordering [102].

#### 4.1.1.3. XRD studies

XRD patterns of pristine and irradiated P3HT thin films performed at room temperature is presented in **Figure 4.7**. The scattering peak at  $5.22^\circ$   $2\theta$  value is due to the first order reflections for the pristine and film irradiated at fluence of  $1 \times 10^{10}$  ions/cm<sup>2</sup>, corresponding to interlayer spacing 1.69 nm [159]. This observed peak corresponds to a-axis orientation, with main polymer chain parallel and side chains are perpendicular to the substrate [160]. After irradiation at a fluence of  $1 \times 10^{10}$  ions/cm<sup>2</sup>, the intensity of the peak is found to be increased which is indicating the improved crystallinity. The size of P3HT crystallite along (100) peak was calculated using Scherrer formula described in **Equation 3.4**.

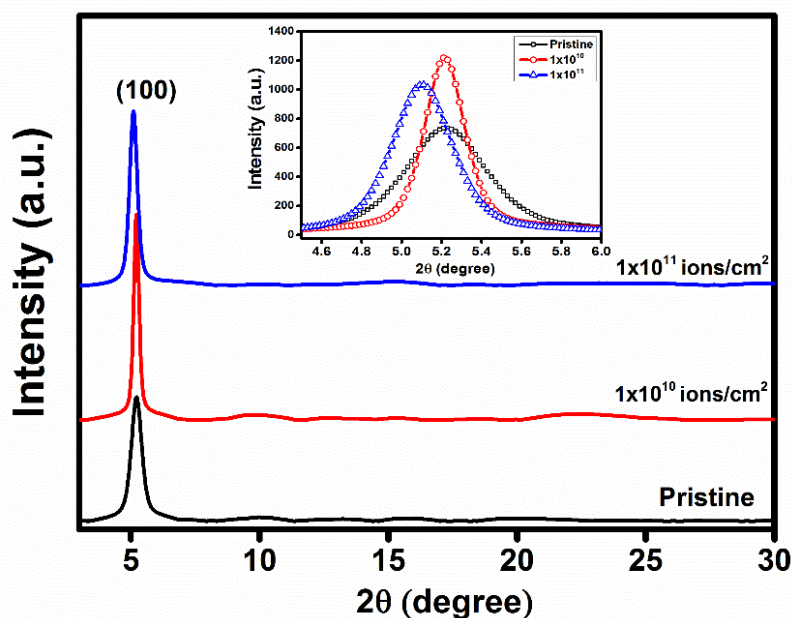


**Figure 4.7:** XRD pattern of pristine and irradiated P3HT thin films.

The statistical analysis of (100) peak reveals the decrease in the FWHM (from  $0.52^\circ$  to  $0.23^\circ$ ) at the fluence of  $1 \times 10^{10}$  ions/cm<sup>2</sup> with increase in the crystallite size (15.43 nm-34.85 nm). All the observations are summarized in **Table 4.3**. The observed increase of the P3HT crystallite size is associated with the increased ordering of the alkyl chains within the main thiophene chain. It has been reported that the structure of rr-P3HT films consists of crystallites embedded in an amorphous polymer matrix [161][162][163].

It is, thus, clear from the XRD spectra that the irradiation induces the increased polymer crystallite size with pronounced a-axis orientation. In the crystallite, the polymer molecules are well oriented and have less structural defects like chain kinks. These defects limits the



conjugation length. Therefore, larger crystallite size leads to the large conjugation length. Thus, the mean conjugation length should be large for irradiated samples [164]. The increase of the mean conjugation length upon irradiation also improves the optical absorption.

The observed intensity of the XRD peak of the film irradiated at the fluence of  $1 \times 10^{11}$  ions/cm<sup>2</sup> is found to be decreased. A small shift in the peak position from  $5.22^\circ$  to  $5.10^\circ$  corresponding to interlayer spacing 1.73 nm is also observed. The measured crystallite size at this fluence is 22.49 nm. The decreased intensity and crystallite size compared to the fluence of  $1 \times 10^{10}$  ions/cm<sup>2</sup> reveals the disordering at this fluence. But the presence of (100) peak after the irradiation at higher fluences shows that the structure of P3HT is not destroyed due to high energy ion impact. Occasionally observed shifts in the X-ray peaks might indicate a distortion of the crystal structure due to increasing strain, resulting from differences in density of the pristine and irradiated zones [165].

**Table 4.3:** XRD and XPS analysis of pristine and irradiated P3HT thin films.

Fluences (ions/cm <sup>2</sup> )	Peak Height (a.u.)	d-spacing (nm)	FWHM ( $^\circ$ )	Crystallite size (nm)	Carbon (at %)	Sulphur (at %)	C/S
0	767.35	1.69	0.52	15.43	88	12	7.33
$1 \times 10^{10}$	1261.62	1.69	0.23	34.85	89	11	8.09
$1 \times 10^{11}$	1090.93	1.73	0.35	22.49	87	13	6.69

#### 4.1.1.4. XPS analysis

**Figure 4.8** shows the XPS survey scan of pristine P3HT films exhibiting only carbon and sulphur peaks at the BEs of 285.0 eV (C 1s) and 164.4 eV (S 2p), respectively [166]. **Figure 4.9** shows the high resolution spectra of C 1s and S 2p peaks for both pristine and ion beam irradiated P3HT thin films. The existence of carbon and sulphur species after ion beam irradiation with fluences of  $1 \times 10^{10}$  and  $1 \times 10^{11}$  ions/cm<sup>2</sup> indicates the presence of thiophene units.

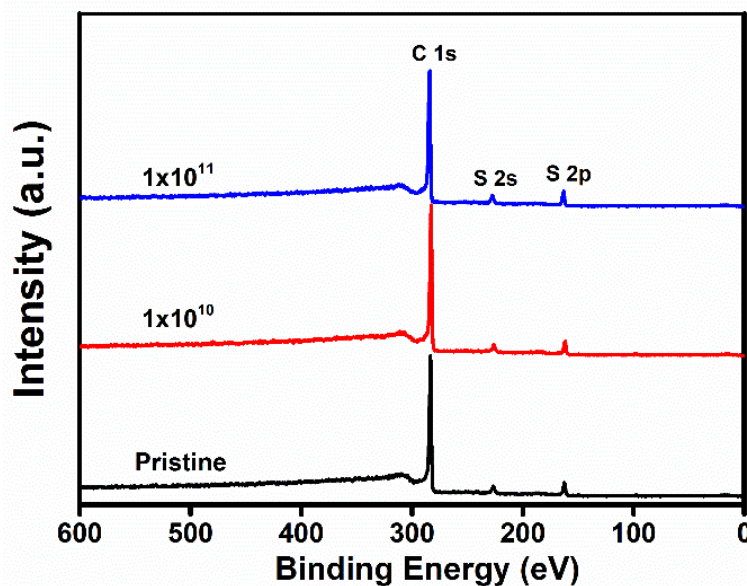


**Figure 4.8:** Typical XPS survey scan of pristine and irradiated P3HT thin films.

C1s peak resolved into two sub-peaks at 285.0 and 286.1 eV. The peak at a BE of 285.0 eV is attributed to C-C/C-H bonds, whereas, the low intensity peak at 286.1 eV corresponds to the C-S bonds [167]. Sulphur core line was found in doublet state (S 2p<sub>3/2</sub> and S 2p<sub>1/2</sub>) in consistence with the spin-orbit splitting in the expected ratio of 2:1 for the pristine film. The S 2p peak at a BE 164.4 eV has been assigned to the S-C bonding in P3HT. The C/S ratio (**Table 4.3**) increases from 7.33 to 8.09 for P3HT thin film irradiated at the fluence of  $1 \times 10^{10}$  ions/cm<sup>2</sup> but decreases to 6.69 after ion irradiation at fluence of  $1 \times 10^{11}$  ions/cm<sup>2</sup>. This decrease in C/S ratio indicates a damage occurring at the fluence of  $1 \times 10^{11}$  ions/cm<sup>2</sup>. Removal of more C atoms than S atoms from the surface region may be due to higher sputtering yield of C atoms. The absence of the shake-up peaks on the higher BE side of C 1s indicates that the  $\pi$  conjugated system is not broken into smaller conjugation length [168] in P3HT thin films after ion irradiation. For the pristine and ion irradiated P3HT thin films at a fluence of  $1 \times 10^{10}$  ions/cm<sup>2</sup>, the shape and position of both the peaks (C 1s and S 2p) are not changing much, representing that the nature of the chemical bonding of thiophene units near the films surface is not affected by irradiation [169] up to the given fluence. However, a small shift (0.4 eV) in both C1s and S 2p peak positions towards the higher BE side can be noticed at a fluence of  $1 \times 10^{11}$  ions/cm<sup>2</sup>, indicating the surface charging effect in the absence of a significant number of C atoms with respect to the

samples irradiated at a fluence of  $1 \times 10^{10}$  ions/cm<sup>2</sup> (mentioned above). That could also be the reason behind the change in shape of the S 2p peak.

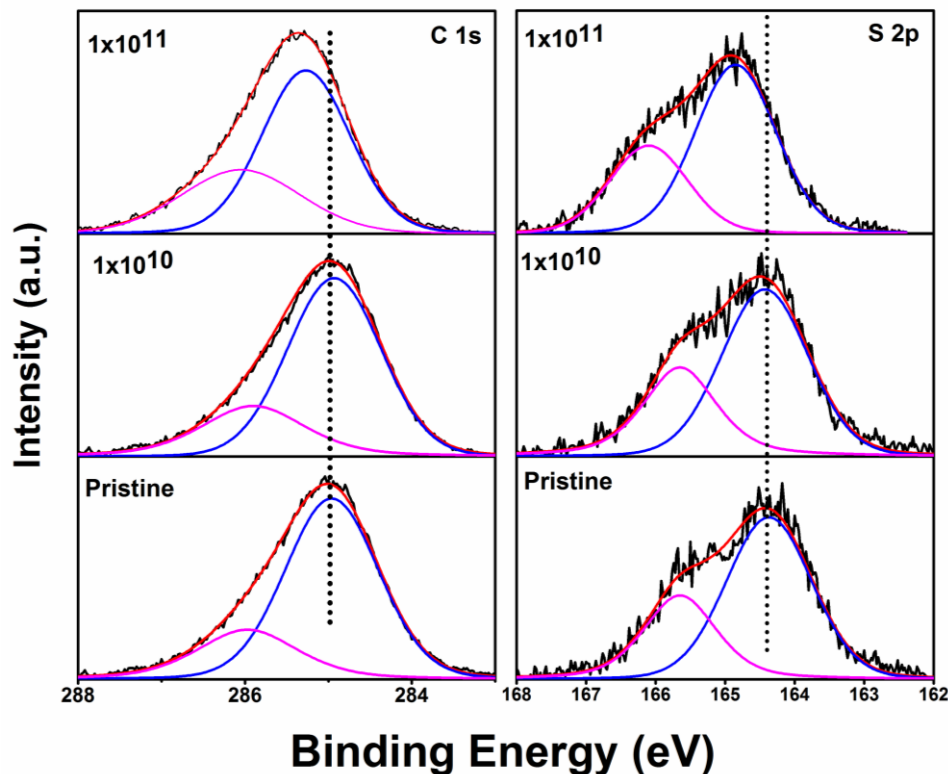


**Figure 4.9:** High resolution spectra of C 1s and S 2p of pristine and irradiated P3HT films.

#### 4.1.1.5. Optical studies

To study the optical properties, the absorption spectra have been observed of P3HT thin films deposited on glass substrate. **Figure 4.10** illustrate the UV- visible absorption spectra of pristine and irradiated films of P3HT at different fluences. In the spectra, the absorption of P3HT is shown in the visible region i.e. 400-800 nm. The two broad peaks observed at 518 nm and 551 nm, which has been attributed to the  $\pi$ - $\pi^*$  transition of the P3HT backbone [76]. One shoulder is also observed at 599 nm which is due to the inter-chain interaction of pristine P3HT thin films. The effect of high energy ion beam irradiation demonstrates the marginal increase in the intensity of absorption peak with increasing incident fluences. It can also be seen from **Figure 4.10** that even at the highest fluence ( $1 \times 10^{11}$  ions/cm<sup>2</sup>), the

absorption peaks are observed at the 518 nm, 551 nm and 599 nm, respectively i.e. no feature of absorption has vanished. The inset of **Figure 4.10** shows the Tauc plot of P3HT films. The variation in the optical bandgap of pristine and irradiated P3HT thin films has been evaluated from Tauc's relation described in **Equation 3.6**. The relation between absorption coefficient  $\alpha$ , optical bandgap  $E_g$  and the energy of incident photon  $h\nu$  are called Tauc relation [136].

The optical bandgap of the pristine P3HT thin film is 1.96 eV and for sample irradiated at a fluence of  $1 \times 10^{11}$  ions/cm<sup>2</sup>, it is about 1.94 eV. The change in the bandgap of P3HT films after ion irradiation is marginal. The variation in the bandgap of pristine and irradiated samples at different fluences is shown in **Table 4.4**.

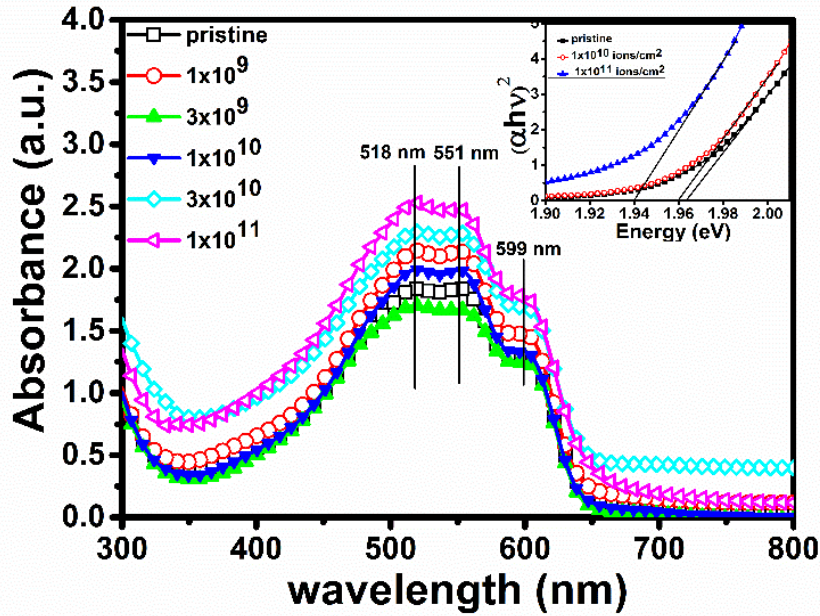


**Figure 4.10:** UV-visible absorption spectra of pristine as well as 90 MeV Ni<sup>7+</sup> ion beam irradiated thin films of P3HT. The inset shows the Tauc plot of pristine and 90 MeV Ni<sup>7+</sup> ion irradiated P3HT thin films.

**Figure 4.11 (a)** is showing the PL spectra of pristine and irradiated P3HT thin films taken at room temperature. The spectra are similar to those reported earlier [170][171]. It is observed from the PL spectra that the emission peak intensity and peak position varies with the ion fluences. The PL peak intensity increases at the fluences of  $1 \times 10^9$  and  $1 \times 10^{10}$  ions/cm<sup>2</sup> and then decreases at fluence of  $1 \times 10^{11}$  ions/cm<sup>2</sup>, but still higher than the intensity

of pristine peak. The increase in observed PL intensity is due to the increased molecular ordering by incident ions. It has also been reported [171] that polymer chains self-organizes to form aggregates in the films and explaining the correlation with the conjugation length. The detailed analysis of PL line shape based on H-aggregates consistent with  $\pi$ -stacks theory has been reported [145][172]. **Figure 4.11 (b)** shows the normalized PL spectra. It could be observed that the PL peak shifts with 0.05 eV towards lower energy after irradiation. This indicates a change in the polymer conformation. A red shift in luminescence spectra generally occurs due to the increased conjugation length favouring higher delocalization of electrons in the polymer chains. The increased conjugation length is also confirmed from the XRD and FTIR analysis in the present study.

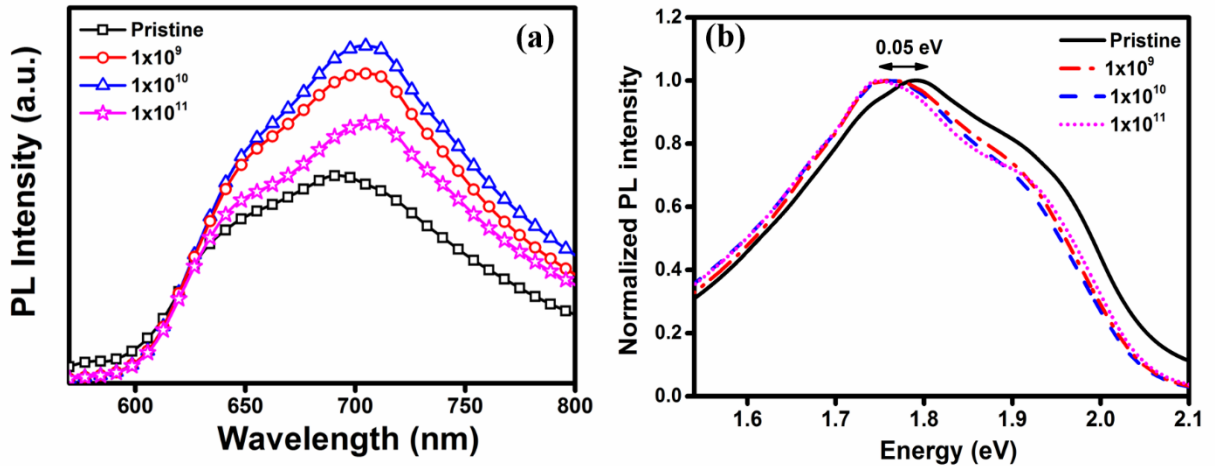


**Figure 4.11:** (a) PL spectra of pristine and 90 MeV Ni<sup>7+</sup> ion beam irradiated P3HT thin films at room temperature. (b) Normalized PL spectra of P3HT thin films.

In order to see the effect of high energy ion beam irradiation on P3HT film's color (absorption and emission spectra), the photographs are provided (**Figure 4.12**). It is clear from the photographs that there is no change in color of the films upto  $1 \times 10^{10}$  ions/cm<sup>2</sup> fluence, but at the highest fluence which is  $1 \times 10^{11}$  ions/cm<sup>2</sup>, a small variation in color has been observed.



**Figure 4.12:** Optical images of pristine and irradiated P3HT samples.

#### 4.1.1.6. Surface measurements

The physical changes in morphology of P3HT films of pristine and irradiated samples have been observed by AFM images which shown in **Figure 4.13**. The morphology displayed in **Figure 4.13** of P3HT thin films was traced by AFM tips in tapping mode over the  $1 \times 1 \mu\text{m}^2$  area. The RMS roughness of pristine films was 4.89 nm. After undergoing irradiation at  $1 \times 10^9$ ,  $3 \times 10^9$ ,  $1 \times 10^{10}$ ,  $3 \times 10^{10}$  and  $1 \times 10^{11}$  ions/cm<sup>2</sup>, the roughness becomes 4.39 nm, 2.87 nm, 3.36 nm, 3.44 nm and 3.66 nm, respectively. Thus the surface become smooth as the fluence is increased upto  $3 \times 10^9$  ions/cm<sup>2</sup>. On further increasing the fluence to  $1 \times 10^{11}$  ions/cm<sup>2</sup>, the surface becomes less smooth (3.66 nm) compared to the film which was irradiated at  $3 \times 10^9$  ions/cm<sup>2</sup> but still the surface roughness is less compared to the roughness of pristine film. So there is an overall decrease in the roughness of films with ion irradiation. The summary of variation in roughness is shown in **Table 4.4**. **Figure 4.13** also shows the change in the texture of the film after irradiation at different fluences. With increasing fluence, coarser texture with the thin hill-like feature has been observed.

**Table 4.4:** Summary of optical bandgap, RMS roughness and contact angle of pristine and 90 MeV Ni<sup>7+</sup> ion irradiated samples at different fluences.

Fluence (ions/cm <sup>2</sup> )	Bandgap (eV)	Roughness (nm)	Contact angle (°)
Pristine	1.96	4.89	100.3
$1 \times 10^9$	-	4.39	102.7
$3 \times 10^9$	-	2.87	105.5
$1 \times 10^{10}$	1.96	3.36	97.5
$3 \times 10^{10}$	-	3.44	96.2
$1 \times 10^{11}$	1.94	3.66	91.0

To study the nature (hydrophilic or hydrophobic) of pristine and irradiated P3HT thin films, wettability measurement has been performed. **Figure 4.14 (a-f)** shows the contact angle images between the water droplet and surface of pristine and 90 MeV Ni<sup>7+</sup> high energy ion beam irradiated thin films of P3HT. The angle was estimated using sessile drop fitting method using the software. From **Figure 4.14 (a)**, it can be seen that the surface of the pristine film is hydrophobic (angle > 90°) in nature because the contact angle between the water droplet and P3HT film surface is 100.3°. Initially with an increase in the fluences upto 3×10<sup>9</sup> ions/cm<sup>2</sup>, the angle between the water droplet and film surface is increased at 105.5° but after the fluence of 3×10<sup>9</sup> ions/cm<sup>2</sup>, the contact angle starts decreasing. For the highest fluence (1×10<sup>11</sup> ions/cm<sup>2</sup>) the contact angle decreases upto 91.0°. The variation in the wettability with increasing fluences has been described in **Table 4.4**.

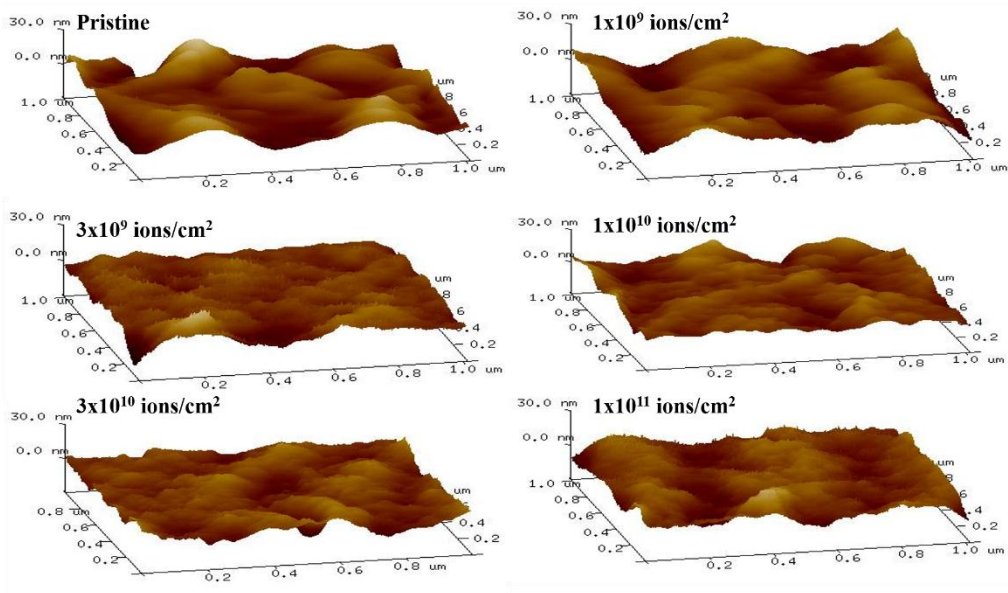


**Figure 4.13:** Three dimensional AFM micrographs of pristine and 90 MeV Ni<sup>7+</sup> irradiated P3HT thin films at different fluences.

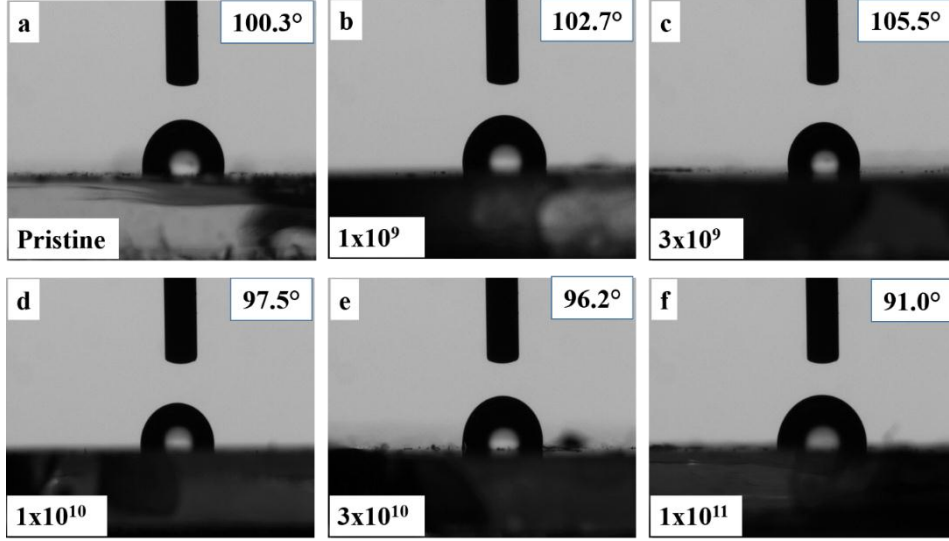


**Figure 4.14:** Contact angle measurement images of pristine and 90 MeV Ni<sup>7+</sup> ion irradiated P3HT films.

#### 4.1.1.7. DC-conductivity measurement

**Figure 4.15 and 4.16** is showing the dc conductivity ( $\sigma_{dc}$ ) variation as a function of  $1000/T$  and  $T^{-1/4}$  respectively in the temperature range of 200 to 400 K for the pristine and irradiated thin films of P3HT. The Mott's 3-dimensional variable range hopping (3D-VRH) model [173] has been used to explain the charge transport mechanism for P3HT [174][175][176][177][178]. According to the Mott's model, the dc conductivity can be written as:

$$\sigma_{dc} = \sigma_0 \exp \left\{ - \left( \frac{T_0}{T} \right)^m \right\} \quad (4.1)$$

Where ' $\sigma_0$ ' and ' $T_0$ ' are constant and ' $T$ ' is the temperature. Here  $m = \frac{1}{d+1}$ , in which, ' $d$ ' is the dimensionality. Thus for 1D, 2D and 3D hopping charge transport ' $m$ ' has values as 1/2, 1/3 and 1/4 respectively. In order to get the proper value of ' $m$ ', three different curves of  $\log \sigma_{dc}$  versus  $\left( \frac{1}{T} \right)^m$  was plotted using the values of  $m = 1/2, 1/3$  and  $1/4$ . Among all these three curves, for the value of  $m = 1/4$ , the curve resembles more to a straight line (**Figure 4.16**) and therefore  $m = 1/4$  was used in the present study for further calculations. Therefore, in the present study, the Mott's 3D VRH mechanism of  $T^{-1/4}$  type seems to be more appropriate and dc conductivity of P3HT thin films can explained using Mott's 3D VRH model which indicates that the charge transport occur by phonon assisted hopping



i.e. thermally activated jumps between the localized sites. The temperature range where **Equation 4.1** is valid should give activation energy as:

$$E_A = \frac{-d(\ln \sigma)}{d(1/K_B T)} \quad (4.2)$$

Where ‘ $K_B$ ’ is Boltzmann constant. The parameters of **Equation (4.1)** can be correlated with the following expression:

$$E_A = mK_B T_0 \left(\frac{T_0}{T}\right)^{m-1} \quad (4.3)$$

**Equation 4.3** shows that a plot of  $\log E_A$  and  $\log T$  should give a straight line with the slope of  $-(m-1)$ . The plot between  $\log E_A$  and  $\log T$  is given in **Figure 4.17** and found the behaviour of activation energy with temperature matches with a straight line with  $m= 1/4$ . This further confirms that the Mott’s 3D VRH mechanism of type  $T^{-1/4}$  explains the charge transport mechanism in pristine and irradiated P3HT thin films. Further, the various Mott’s parameters associated with charge transport have also been evaluated.  $T_0$  and  $\sigma_0$  can be described as:

$$T_0 = \frac{\lambda \alpha^3}{K_B N(E_F)} \quad (4.4)$$

And

$$\sigma_0 = e^2 R^2 \vartheta_0 N(E_F) \quad (4.5)$$

Where ‘ $T_0$ ’ is the characteristic temperature, ‘ $\lambda$ ’ is dimensionless constant  $\sim 18.1$  [179][180][181], ‘ $\alpha$ ’ is the exponential decay coefficient of the localized states which, are involved in the hopping process and is equal to the width of the thiophene monomer unit ( $\alpha^{-1} \sim 3.185 \text{ \AA}$ ) [182] since the electrons are always delocalized to the extent of  $\pi$ -orbitals on the monomer units, ‘ $N(E_F)$ ’ is the density of states at Fermi level. In **Equation 4.5**, ‘ $e$ ’ is the electronic charge, ‘ $\sigma_0$ ’ is the conductivity at infinite temperature, ‘ $\nu_0$ ’ is the phonon frequency ( $\sim 10^{13}$  Hz) and ‘ $R$ ’ is the average hopping distance between two sites. Where ‘ $R$ ’ can be calculated from:

$$R = \left\{ \frac{9}{8\pi\alpha K_B T N(E_F)} \right\}^{1/4} \quad (4.6)$$

The average hopping energy ‘ $W$ ’ can be estimated by using following formula:

$$W = \frac{3}{4\pi R^3 N(E_F)} \quad (4.7)$$

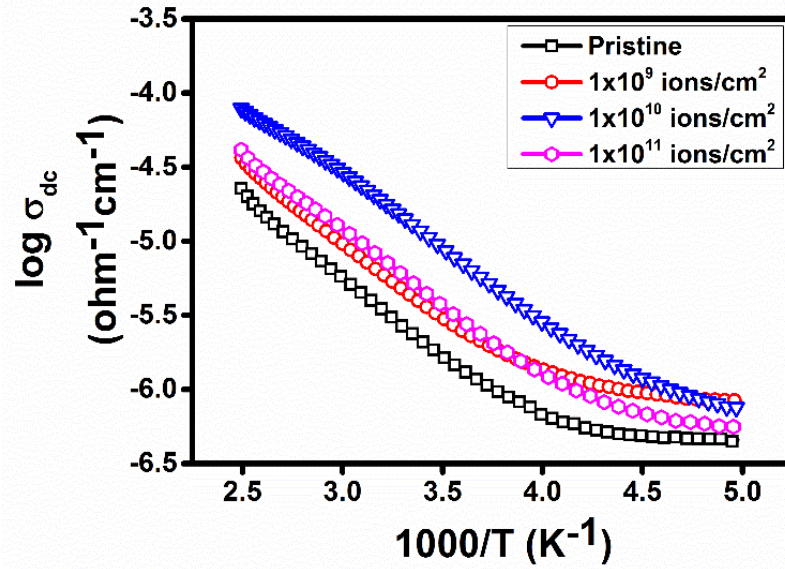


**Figure 4.15:** The plot of log of dc conductivity ( $\sigma_{dc}$ ) as a reciprocal of Temperature ( $1000/T$ ) in the range of 200-400 K for pristine and 90 MeV  $Ni^{7+}$  ion irradiated P3HT thin films.

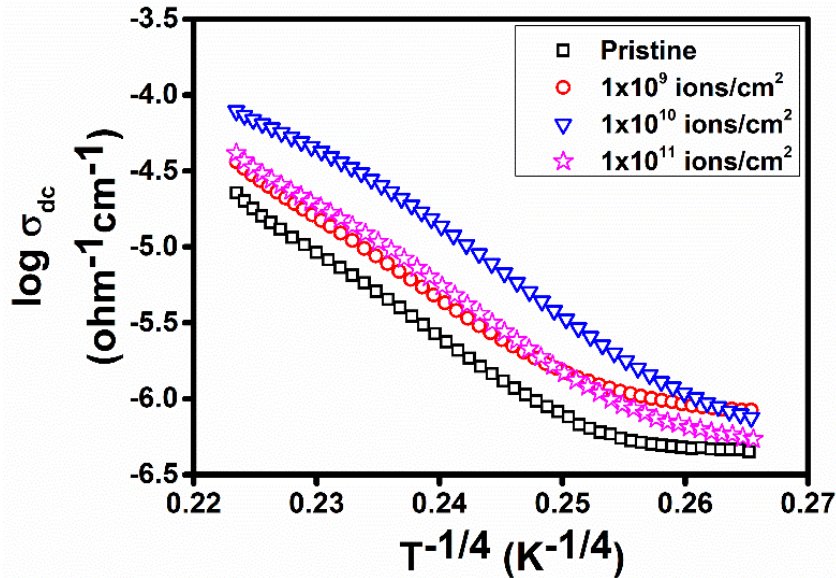


**Figure 4.16:** The log of dc conductivity ( $\sigma_{dc}$ ) plotted as a function of reciprocal of Temperature ( $T^{-1/4}$ ) in the range of 200-400 K for pristine as well as 90 MeV  $Ni^{7+}$  ion irradiated P3HT thin films.

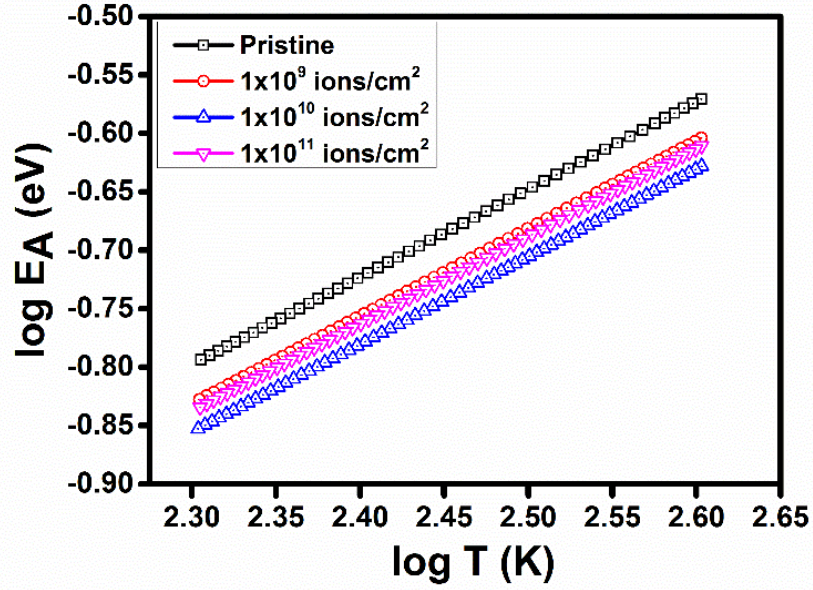


**Figure 4.17:** Plot of  $\log E_A$  versus  $\log T$  in the temperature range 200-400 K for pristine and 90 MeV  $\text{Ni}^{7+}$  ion irradiated P3HT thin films.

For the present study, the value of all Mott's parameters  $T_0$ ,  $N(E_F)$ ,  $R$ ,  $W$  at 300 K has been calculated using **Equations (4.4)-(4.7)** and summarized in **Table 4.5**. In this calculation, the density of states calculated from **Equation (4.4)** is based on the assumption that the wave function localization length remains independent of temperature and conductivity.

The results of Mott's parameters (**Table 4.5**) shows that at room temperature (300 K), the dc conductivity has been found to be increased at the fluence of  $1 \times 10^{10}$  ions/cm<sup>2</sup> and the density of states at Fermi level of pristine and irradiated thin films is  $\sim 10^{19}$  cm<sup>-3</sup>eV<sup>-1</sup> which are in good agreement with the values of previously reported [174][178][179][180][181][183][184]. The value of  $T_0$  has been estimated from the slop of  $\log \sigma_{dc}$  versus  $T^{-1/4}$  and found to decrease with increase in the conductivity (**Table 4.5**). The calculated results for the present study fulfil the Mott's requirement that  $\alpha R \gg 1$  and  $W \gg K_B T$  for the conductivity by hopping to distant sites. This further indicates that three-dimensional variable range hopping is dominated for pristine as well as irradiated samples for the conduction.

**Table 4.5:** Summary of Mott's parameters at room temperature (300 K) for pristine and irradiated thin films.

Fluences (ions/cm <sup>2</sup> )	Conductivity $\sigma_{dc}$ (Ohm <sup>-1</sup> cm <sup>-1</sup> ) at 300 K	E <sub>A</sub> (eV) At 300 K	T <sub>0</sub> (K)	N(E <sub>F</sub> ) (cm <sup>-3</sup> eV <sup>-1</sup> )	R (Å)	W (eV)	$\alpha R$
Pristine	2.48×10 <sup>-6</sup>	0.215	3.65×10 <sup>8</sup>	1.8×10 <sup>19</sup>	39.8	0.211	12.5
1×10 <sup>9</sup>	4.40×10 <sup>-6</sup>	0.200	2.77×10 <sup>8</sup>	2.3×10 <sup>19</sup>	37.2	0.202	11.7
1×10 <sup>10</sup>	1.35×10 <sup>-5</sup>	0.189	2.21×10 <sup>8</sup>	2.9×10 <sup>19</sup>	35.0	0.190	10.9
1×10 <sup>11</sup>	4.88×10 <sup>-6</sup>	0.197	2.60×10 <sup>8</sup>	2.5×10 <sup>19</sup>	36.5	0.196	11.5

#### 4.2 Effect of high energy ions on the different properties of P3HT thin films by 55 MeV Si<sup>4+</sup> ion beam

P3HT is a promising donor material in various organic electronic devices, therefore fundamental studies on structure property correlation with regard to charge transport, optical and mechanical properties, morphology, etc. have been analyzed in details earlier [172][174][171][153]. P3HT is a semi-crystalline polymer consisting of a  $\pi$ - conjugated backbone with thiophene monomer unit and alkyl side chains. The crystallinity of conjugated polymer is due to the formation of multiple helices or chain folding. The polymer backbone provides the advantage for the functional properties such as anisotropic charge transport with characteristic absorption in the low-energy part of the spectrum [185][186]. The charge transport depends upon the extent of  $\pi$ - conjugation along the backbone and also on intermolecular chain interaction along with the morphology. Impingement of SHI can produce the collective excitation followed by a large excited volume surrounding the ion path. This excitation can rotate the backbone bonds and different conformations may be acquired. Moreover, after cooling, the regular section of chains may pack together and regions of crystallinity are formed [85]. In the present section, the effect of 55 MeV Si<sup>4+</sup> swift heavy ion beam bombardment on P3HT thin films in order to evaluate the changes in the structure of the thin film in nanometer level in a different beam parameter and the subsequent effect on the transport and other properties. The incident ions have almost half of the electronic energy loss in comparison to the previous section.

Thin films of P3HT, deposited using spin coating method on glass and double side polished substrates and then irradiated by 55 MeV Si<sup>4+</sup> ions at IUAC, New Delhi. The beam was incidence at normal to the film surface to carry out the irradiation process with different fluences ranging from  $1 \times 10^{10}$  to  $1 \times 10^{12}$  ions/cm<sup>2</sup>. The S<sub>e</sub> and S<sub>n</sub> for the 55 MeV Si<sup>4+</sup> ions in P3HT matrix is 1921 eV/nm and 1.878 eV/nm, respectively. The range of Si<sup>4+</sup> ions in P3HT matrix is 27.03 μm calculated by SRIM 2008 software.

## 4.2.1. Results and discussion

### 4.2.1.1. Micro-Raman analysis

To analyse the structural alteration, micro-Raman analysis have been performed on the P3HT thin films. **Figure 4.18** represents the micro-Raman spectra of the pristine P3HT thin film at 532 nm excitation. The observed spectrum of P3HT confirms the presence of intensive Raman bands in the range of 500-2000 cm<sup>-1</sup>. The Raman band observed at 725 cm<sup>-1</sup> and 1186 cm<sup>-1</sup> are assigned to C-S-C ring deformation and C-H bending, respectively [153][149]. The band at 1208 cm<sup>-1</sup> is related to C-C inter-ring stretching. The bands at the position of 1380 cm<sup>-1</sup> and 1448 cm<sup>-1</sup> are corresponding to C-C skeletal stretching and C=C symmetric ring stretching, respectively.

To observe the effect of energetic ions on structural properties of P3HT thin films, we analyze the regions from 1350 to 1500 cm<sup>-1</sup> (**Figure 4.19**) as this region is supposed to be sensitive to π-electron delocalization or conjugation length of P3HT molecules [152]. The Lorentzian function was used for fitting the peak around 1448 cm<sup>-1</sup>. For the P3HT films irradiated at the fluences of  $1 \times 10^{10}$  and  $1 \times 10^{11}$  ions/cm<sup>2</sup>, an increase in the intensity corresponding to 1448 cm<sup>-1</sup> band is observed which, indicates an ordering in the polymer matrix. A modified material is created in cylindrical region around the ion path when, high energy ion beam interacts with the target material, according to the Thermal Spike model [85][154]. There is less heating effect in the annular region which surrounds the core of the ion path. The ordering due to this less heating effect is very well known phenomena and is responsible for the molecular ordering of P3HT at low fluences in the present study also. However, a significant decrease in the peak intensity is observed when, the films are irradiated with a fluence of  $1 \times 10^{12}$  ions/cm<sup>2</sup>. At high fluence, more ions pass through the

polymer film increasing the overlapping of the core region. Ordering of P3HT will start diminishing in track core regions, due to bond breaking at higher fluences.

**Figure 4.20** summarizes the variation of FWHM and relative intensity ratio ( $I_{c-c}/I_{c=c}$ ) with incident ion fluences. The decrease in the FWHM and increment in the relative intensity ratio ( $I_{c-c}/I_{c=c}$ ) (up to  $1 \times 10^{11}$  ions/cm<sup>2</sup> fluence) described the increased molecular ordering and enhanced effective conjugation length along polymer backbone [153][149][187][188]. It has been reported using Raman simulation that the intensity ratio ( $I_{c-c}/I_{c=c}$ ) increases with increasing chain length without any significant change in the peak position. Also, the enhancement in the relative C – C mode intensity might be relevant to the electron-phonon coupling of this mode and responsible for increased charge transfer from C = C bonds [153].

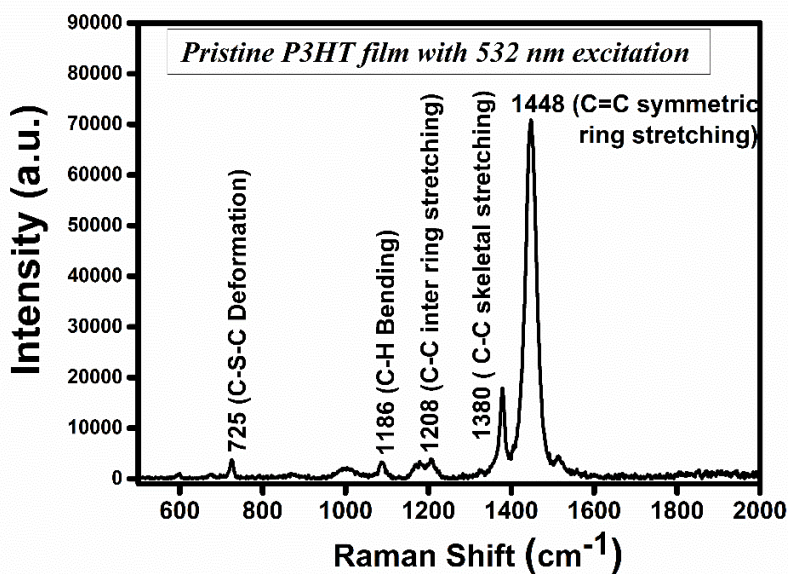


**Figure 4.18:** Raman spectrum of Pristine P3HT thin film confirming the presence of all Raman active modes of P3HT.

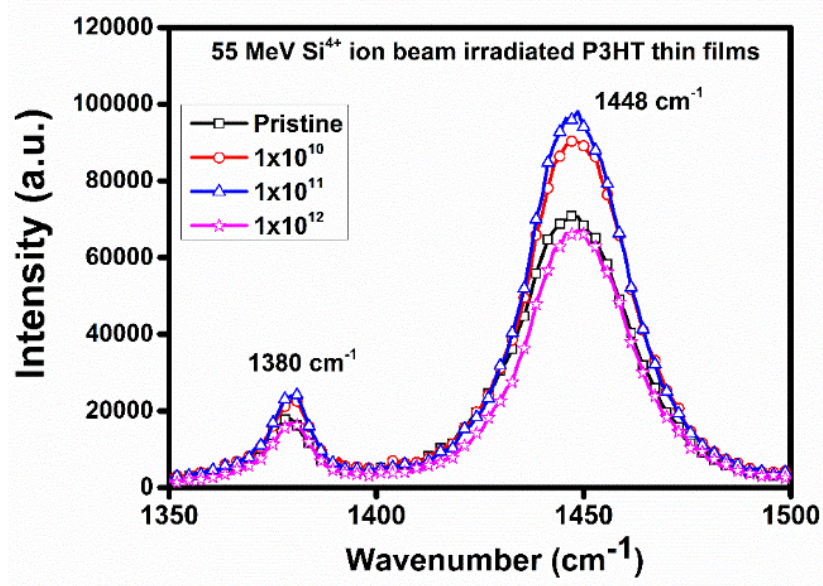


**Figure 4.19:** Raman spectra of 1380  $\text{cm}^{-1}$  and 1448  $\text{cm}^{-1}$  vibrational peaks for pristine and irradiated P3HT thin films.

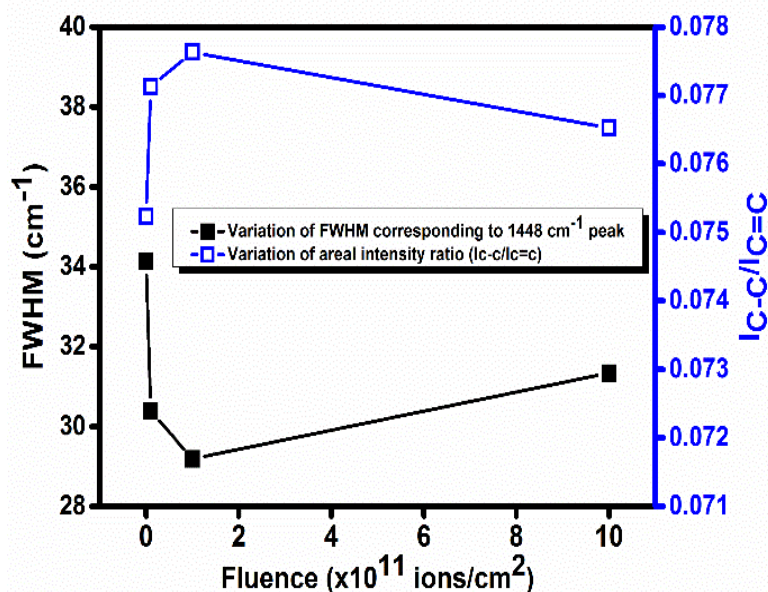


**Figure 4.20.** Variation of FWHM and relative intensity ratio ( $I_{c-c}/I_{c=c}$ ) corresponding to 1448  $\text{cm}^{-1}$  peak for pristine and irradiated P3HT films.

#### 4.2.1.2. FTIR studies

**Figure 4.21** shows the FTIR spectra of both pristine and irradiated P3HT thin films at different fluences of  $1 \times 10^{10}$ ,  $1 \times 10^{11}$  and  $1 \times 10^{12}$  ions/ $\text{cm}^2$ . In **Figure 4.21**, the entire FTIR spectra are vertically shifted for clarity. Pristine P3HT spectra showed FTIR characteristic

features similar to those reported earlier [174][189]. The FTIR band observed at  $735\text{ cm}^{-1}$  is corresponding to methyl rock. The band observed at  $821\text{ cm}^{-1}$  confirmed the presence for aromatic C-H out of plain vibrations and is the characteristic of (3-hexylthiophene-2,5-diyl). The band at  $1380\text{ cm}^{-1}$  corresponds to the carbon-to-sulphur (C-S) single bond stretching vibrations. The two bands observed at  $1460\text{ cm}^{-1}$  and  $1508\text{ cm}^{-1}$  are related to carbon-to-carbon double bond (C=C) symmetric ring stretching and C=C asymmetric ring stretching vibrations respectively. The spectra further show the C-H aliphatic stretching at  $2857$  and  $2923\text{ cm}^{-1}$ . The band observed at  $821\text{ cm}^{-1}$  indicates the structure of P3HT is rr-P3HT chains.

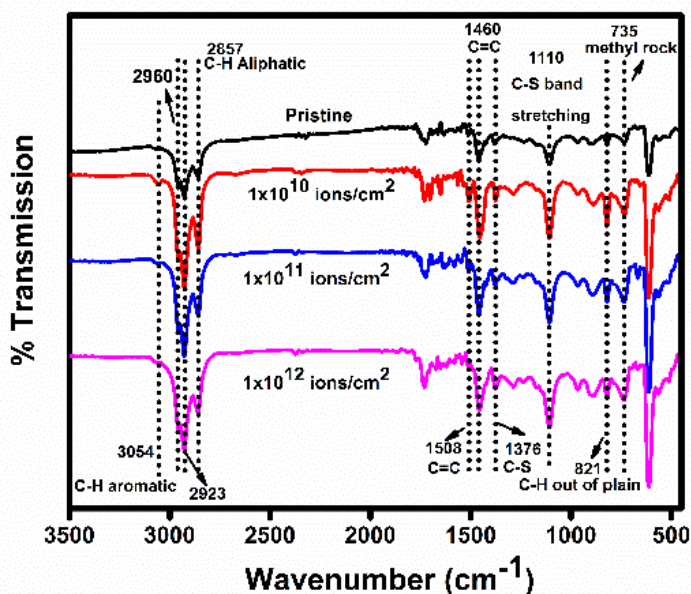


**Figure 4.21:** FTIR spectra of as deposited as well as irradiated thin films of P3HT.

It can also be seen from **Figure 4.21** that FTIR spectra of P3HT irradiated at the fluences of  $1 \times 10^{10}$  and  $1 \times 10^{11}$  ions/cm<sup>2</sup> are different from that of the pristine counterpart. The intensities of the characteristic IR bands are significantly increased. To analyze the effect on structural modification, mainly the ratio of two peaks ( $I_{1508}/I_{1460}$ ) is used. The relationship between intensity ratios with the effective or average conjugation length has been reported [186][190]. The intensity ratio,  $I_{1508}/I_{1460}$ , can be used to analyze the conjugation length of P3HT which is increased from 0.08 to 0.14 for the sample irradiated



at  $1 \times 10^{11}$  ions/cm<sup>2</sup> fluence. Larger conjugation length and better ordering of polymer matrix are indicated after the irradiation [171]. The IR spectrum of P3HT film, irradiated at  $1 \times 10^{12}$  ions/cm<sup>2</sup> fluence, is also showing all the features of P3HT and none of the peaks of the pristine materials disappeared, showing slight change in structure produced by large energy density deposition during irradiation. A small feature at  $3054 \text{ cm}^{-1}$  is observed and the intensity of which increased after the irradiation by the ions. This band is related to aromatic C-H stretching and the increase in its intensity signifies better ordering of the polymer structure [171]. This change in the intensity anticipates that high energy density deposited along the ion path in host polymer during the irradiation. After irradiation with the high energy ions, the deposited energy may be responsible for the induced modifications. The irradiation process at low fluences induced the enhanced crystallinity along with the conjugation length because of the less heating effect in the halo region of the ion path. But with increased fluences, the overlapping of ion tracks increases which, further increases the bond breaking or chain scissoring provoking structural deformation [85]. Therefore, the increased intensity of C=C ring stretching bands (**Figure 4.21**) and the absorption band at  $3054 \text{ cm}^{-1}$  provides confirmation of the better ordering of the polymer after the irradiation by energetic ions.

#### 4.2.1.3. HR-XRD analysis

The HR-XRD pattern (using X-ray source 12 keV with a wavelength of 0.1033 nm) of spin coated pristine P3HT thin film (~ 300 nm) is presented in **Figure 4.22 (a & b)** showing the presence of diffraction peaks at  $2\theta = 3.6^\circ$ ,  $7.1^\circ$  and  $10.7^\circ$  which are assigned to first order (100), second order (200) and third order (300) reflections, respectively. The Bragg angles ( $2\theta$ ) in the present study differ with those reported earlier [191] since a different wavelength ( $\lambda=0.15418 \text{ nm}$ , Cu  $K\alpha$ ) of the X-rays were used in the earlier studies and according to Bragg's law ( $n\lambda = 2d \sin\theta$ ), the angle ( $\theta$ ) will change if the wavelength of incident X-rays changes, for the same d-spacing value (d). All the well-defined diffraction peaks are attributed to a coherent ordering, self-organized lamellar structure with an interlayer spacing. This interlayer spacing is originated by polymer main chains which are stacked parallel and separated by regions of alkyl side-chains [192][193][164]. The d-spacing values for the most intense peak, presented in **Table 4.6** are found to be in the

range of 1.64 to 1.69 nm for pristine and irradiated thin films. The observed d-spacing values are in good agreement with those of earlier reports [168][194]. It can be concluded that most intense ( $2\theta = 3.6^\circ$ ) peak (**Figure 4.22 (a)**) originating from polymer crystallite corresponds to the a-axis orientation (100) pointing the direction of the alkyl chains i.e. main polymer chains are parallel and alkyl side chains are perpendicular to the substrate (**Figure 4.23**) [195][196]. **Figure 4.22** shows the enhancement of the intensity of XRD peaks of the samples after high energy ion irradiation and retains their position (upto  $1 \times 10^{11}$  ions/cm<sup>2</sup> fluence). Furthermore, the crystallite size or mean diameter can also be determined using Scherrer's formula described in **Equation 3.4** [194][197].

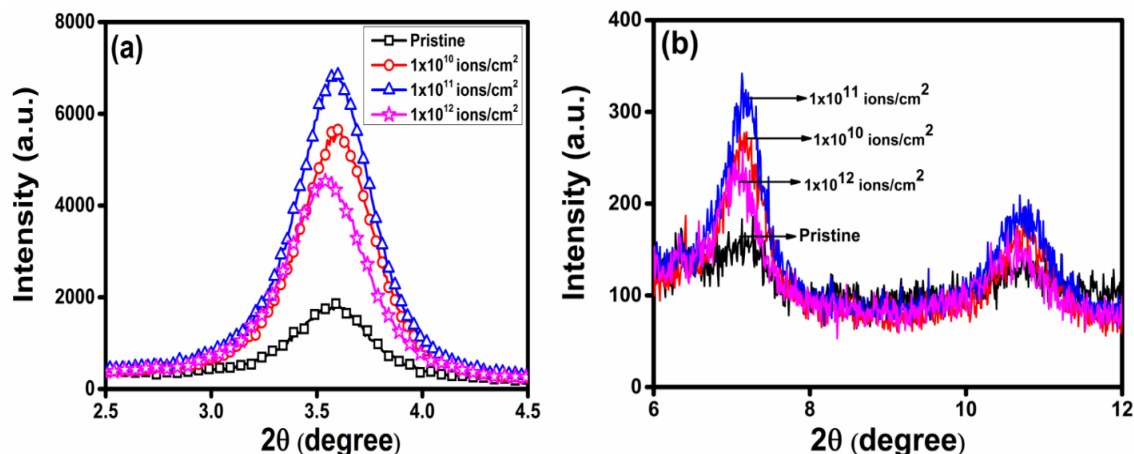


**Figure 4.22:** HR-XRD patterns of P3HT thin films for different peaks before and after irradiation with 55 MeV Si<sup>4+</sup> ion beam.

The mean crystallite diameter, (summarized in **Table 4.6**), show an increase in crystallite size along (100) peak with irradiation upto the fluence of  $1 \times 10^{11}$  ions/cm<sup>2</sup>. This increase in the crystallite size indicates towards the increased ordering of alkyl side chains associated with the main thiophene chains and also suggests that high energy ion irradiation at low fluences (up to  $1 \times 10^{11}$  ions/cm<sup>2</sup>) could improve the overall crystallinity of P3HT thin films remarkably. The polymer molecules within the crystallites are very well oriented and have less structural defects which, limit the length of conjugation. Therefore, the mean conjugation length in the crystallite is larger in SHI irradiated samples having large crystallite size [164]. Upon SHI irradiation, high energy produces a large excited volume due to collective excitation which, causes bond breaking and/or cross-linking depending

on the incident energy. Closely packed regions by crosslinking, chain folding or by single/multiple helices formation are formed by the increased density of polymer due to irradiation. This contributes to the production of large crystalline regions in polymer films and the increased crystallinity [198]. However, At the highest fluence,  $1 \times 10^{12}$  ions/cm<sup>2</sup>, the diffraction pattern (**Figure 4.22**) shows the decreased intensity and slight shift towards the lower  $2\theta$  value, which indicates the structural distortion at this fluence due to increasing strain produced from the density differences of the pristine and irradiated zones [165] or change in interplanar spacing. Thus, an optimum fluence is necessary to produce highly crystalline P3HT.

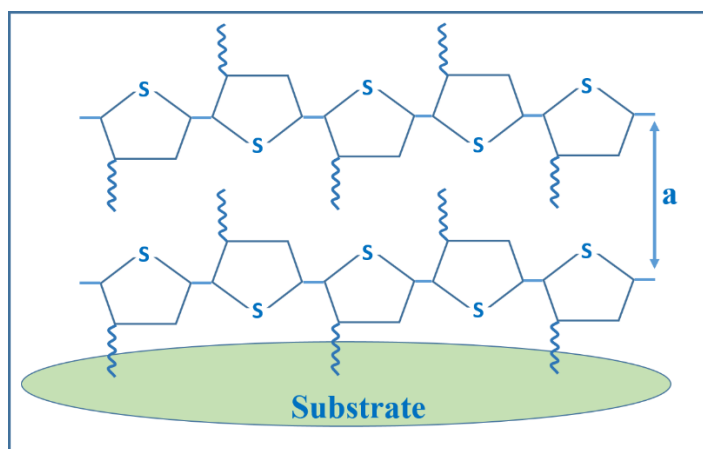


**Figure 4.23:** Schematic of possible a-axis orientation (main polymer chains are parallel and alkyl side chains are perpendicular to the substrate) of the thiophene crystallites with respect to the substrate.

**Table 4.6:** Summary of different parameters calculated using HR-XRD spectra for pristine and irradiated thin films of P3HT.

Peak Position ( $2\theta$ )	Fluence (ions/cm <sup>2</sup> )	Peak height	d-spacing (nm)	FWHM (°)	Crystallite Size (nm)
3.6	0	1411.70	16.4	0.43	12.41
	$1 \times 10^{10}$	4865.15	16.4	0.42	12.52
	$1 \times 10^{11}$	5917.46	16.4	0.41	13.02
	$1 \times 10^{12}$	3863.72	16.9	0.44	12.12

#### 4.2.1.4. XPS analysis

**Figure 4.24** shows the high resolution spectra of C 1s and S 2p peaks for both pristine as well as irradiated P3HT thin films. Two sub peaks at 285.0 and 286.1 eV of C1s peaks is observed which are attributed to C-C/C-H bonds and C-S bonds, respectively [167]. Similarly, Sulphur core line was found in doublet state (S 2p<sub>3/2</sub> and S p<sub>1/2</sub>) in consistence with the spin-orbit splitting in the ratio of 2:1 for the pristine film. The peak situated at 164.4 eV is assigned to S-C bonding in P3HT film. After irradiation at different fluences such as  $1 \times 10^{10}$ ,  $1 \times 10^{11}$  and  $1 \times 10^{12}$  ions/cm<sup>2</sup>, both peaks of carbon and sulphur species are existing which is indicating the presence of thiophene units even after irradiation at highest fluence ( $1 \times 10^{10}$  ions/cm<sup>2</sup>).

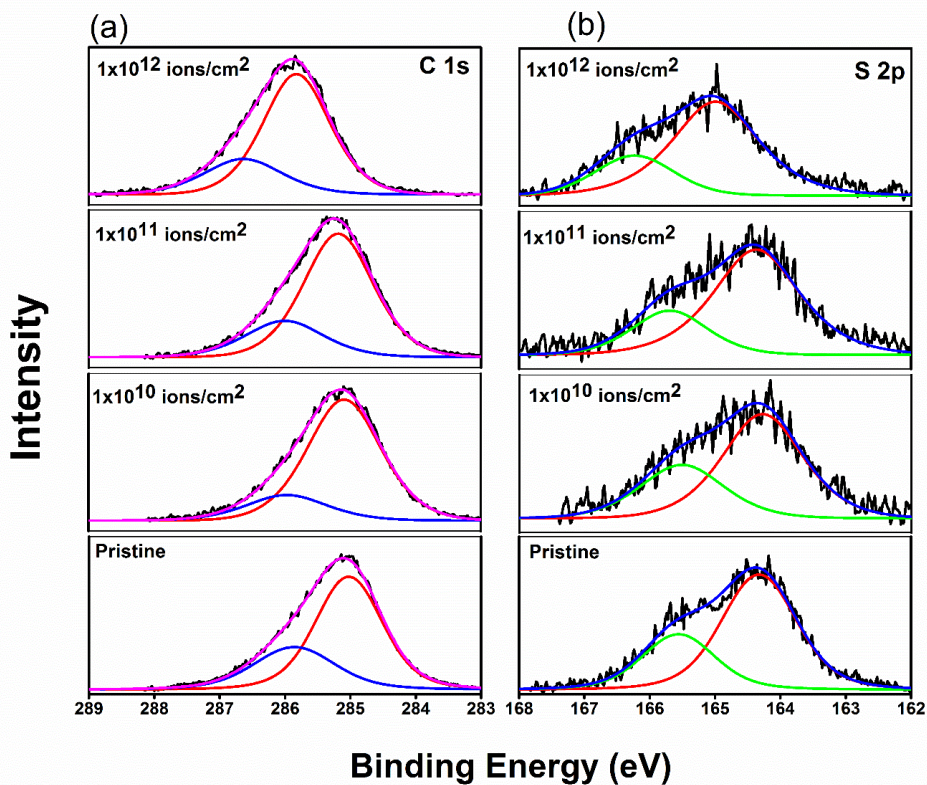


**Figure 4.24:** High resolution spectra of C 1s and S 2p of pristine and irradiated P3HT films.

The confirmation regarding sustainability of conjugated system after irradiation i.e.  $\pi$ -conjugated system is not broken into smaller conjugation length is observed by the absence of the shake-up peaks on the higher binding energy side of C 1s spectra [168]. The shape and position of both peaks (C 1s & S 2p) is not changing upto the fluence of  $1 \times 10^{10}$  ions/cm<sup>2</sup> indicating that chemical bonding of thiophene units are not affecting by irradiation. After that at the fluence of  $1 \times 10^{11}$  ions/cm<sup>2</sup>, a slight shifting in peak position is observed for the both peaks. While, at the highest fluence,  $1 \times 10^{12}$  ions/cm<sup>2</sup>, a shift of 0.8 eV for the C 1s peak and 0.6 eV shift for the S 2p peak towards the higher BE side is observed. This shift in the BE position suggesting the charging effect due to the lack of C atoms near the surface.

#### 4.2.1.5. Optical studies

The absorption properties of P3HT thin films have been analyzed using UV-visible absorption spectra. As shown in **Figure 4.25**, the spectra of pristine and irradiated films at different fluences ranging from  $1 \times 10^{10}$  ions/cm<sup>2</sup> to  $1 \times 10^{12}$  ions/cm<sup>2</sup> consisting the two broad peaks observed at 518 nm and 550 nm are corresponding to  $\pi$ - $\pi^*$  transition of the P3HT backbone [76]. Due to the inter-chain interaction of P3HT thin films, one shoulder is observed at 600 nm which depict the higher crystallization of inter-chain interaction in semiconducting polymer [199]. The enhanced absorption intensity has been observed after the irradiation upto the fluence of  $1 \times 10^{11}$  ions/cm<sup>2</sup>, while, at highest fluence ( $1 \times 10^{12}$  ions/cm<sup>2</sup>) the intensity of the absorption spectra is found to be reduced. Further, the bandgap for pristine as well as irradiated samples was calculated using Tauc's relation (**Equation 3.6**) and observed (**inset of Figure 4.25**) a slight variation after ion irradiation. The variation in bandgap with incident ion fluence is summarized in **Table 4.7**. For pristine sample, bandgap measured at 1.92 eV while, at highest fluence ( $1 \times 10^{12}$  ions/cm<sup>2</sup>) it reduces at 1.89 eV.

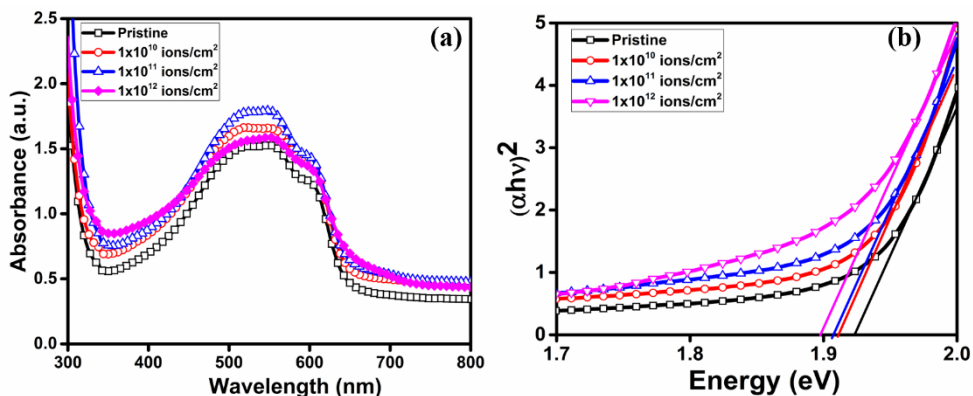


**Figure 4.25:** Optical absorption spectra of pristine and irradiated P3HT thin films (a). The bandgap variation with different fluences (b).

**Figure 4.26** is showing the PL emission spectra of P3HT thin films at room temperature and found as similar with earlier reports [171]. The variation in emission peak intensity with the ion fluences is observed. The enhancement in the PL peak intensity is observed upto the fluence of  $1 \times 10^{11}$  ions/cm<sup>2</sup> and then decreases at fluence of  $1 \times 10^{12}$  ions/cm<sup>2</sup>, but still higher than the intensity of pristine peak. The increase in observed PL band intensity is due to the increased molecular ordering by incident ions. It has been reported [171] that polymer chains self-organizes to form aggregates in the films. The detailed analysis of PL line shape based on H-aggregates consisting with  $\pi$ -stacks theory has been reported [172].

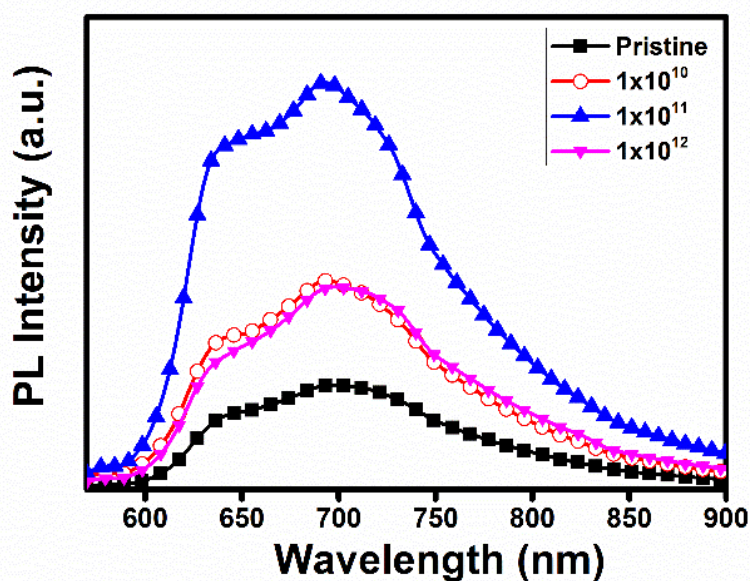


**Figure 4.26.** Emission spectra of pristine and irradiated P3HT thin films.

#### 4.2.1.6. Surface measurements

Modifications of the surface produced by high energy ion impingement have been analyzed by atomic force micrographs. **Figure 4.27** shows the 3D images of pristine and irradiated P3HT thin films. The variation in the surface RMS roughness after the ion beam irradiation indicated the surface properties is also dependent on the incident ions. The variation of roughness with incident ion fluences has been summarized in **Table 4.7**. It has been observed that the roughness increased upto the fluence of  $1 \times 10^{11}$  ions/cm<sup>2</sup> which is due to the ion irradiation induced sputtering at the surface. This increase in surface roughness is considered to be an effect of polymer self-organization and phase separation [200]. However, the decrease of roughness at highest fluence ( $1 \times 10^{12}$  ions/cm<sup>2</sup>) is due to the formation of the overlapping ion tracks and the merger of the modified impressions.

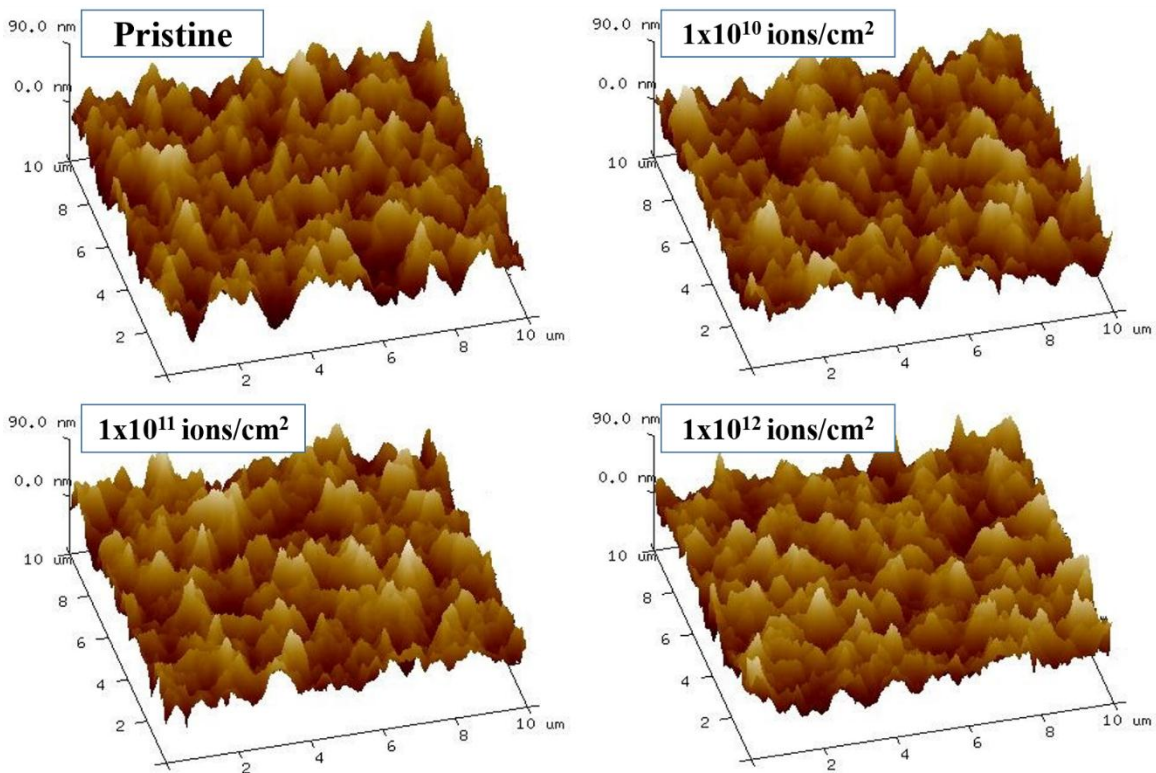


**Figure 4.27:** Three dimensional AFM micrographs of pristine and 55 MeV Si<sup>4+</sup> ion beam irradiated P3HT thin films.

Contact angle measurement is a powerful tool to characterize the wettability of any polymer surface and can be described using Young's equation. The topographical change

due to the incidence of energetic ions is analyzed using contact angle measurement. **Figure 4.28** shows the wettability variation with the incident ion fluences. It has been reported [142] that the surface of any material is not flat ideally i.e. it is having some roughness. The impingement of energetic ions on the thin films surface can alter/modify the area of contact with droplet which, further results in the alteration/modification in the interaction of water molecule with the surface of the thin film. Therefore, to include the surface roughness factor, Wenzel introduced roughness term in the Young's equation [142] and describe that with increasing the surface roughness, the hydrophobicity of the surface becomes more hydrophobic and hydrophilic surface becomes more hydrophilic. So, the wettability of any surface is altered with the change in the roughness. **Table 4.7** summarizing the contact angle variation with fluences along with the roughness of the film surface. In the present study also, it is observed that similar to the surface roughness, the contact angle is also increasing upto the fluence of  $1 \times 10^{11}$  ions/cm<sup>2</sup> to 104.23° and decreased to 102.78° at the highest fluence ( $1 \times 10^{12}$  ions/cm<sup>2</sup>). From AFM studies it is clear that the roughness of the film enhances upto this fluence and after that it decreases which is also supporting the fact i.e. when, the roughness increases the hydrophobic surface becomes more hydrophobic.

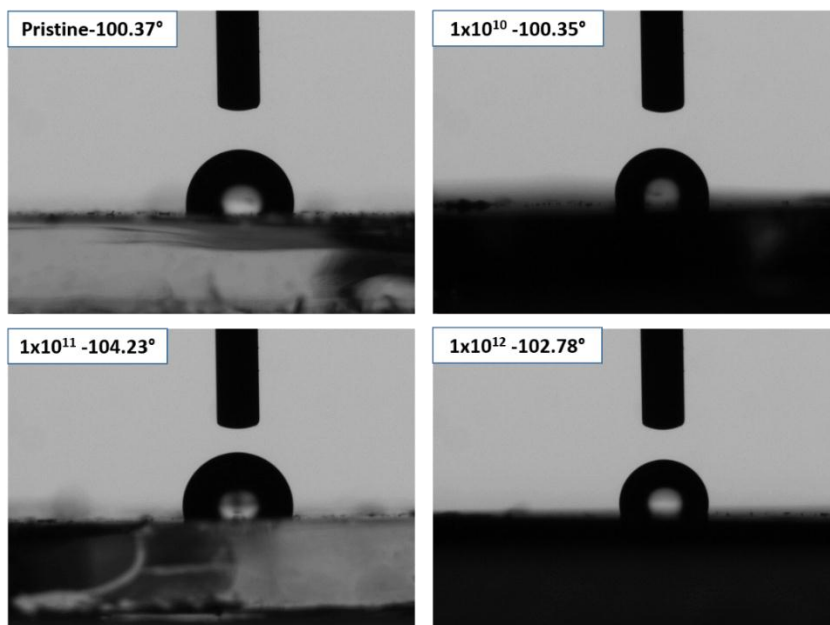


**Figure 4.28:** Snapshots of contact angle measurement of pristine and irradiated P3HT thin films.



**Table 4.7:** Summary of different parameters of irradiated P3HT thin films.

<b>Fluence (ions/cm<sup>2</sup>)</b>	<b>Bandgap (eV)</b>	<b>Roughness (nm)</b>	<b>Contact angle (degree)</b>
Pristine	1.92	17.3	100.37
1×10 <sup>10</sup>	1.91	17.5	100.35
1×10 <sup>11</sup>	1.90	18.5	104.23
1×10 <sup>12</sup>	1.89	17.2	102.78

#### 4.2.1.7. Electrical conductivity

DC conductivity measurement is performed using two probe method to measure the effect of irradiation and subsequently improved crystallinity. It is observed that conductivity is increased after irradiation with energetic ions. **Table 4.8** shows that the room temperature (300 K) dc conductivity increases with incident ions up to the fluence of 1×10<sup>11</sup> ions/cm<sup>2</sup>. This enhancement in the conductivity may be ascribed to the better ordering of polymer chains by displacement of atoms leading to closely packed chains after high energy ion irradiation. Due to the high energy ion irradiation, the molecular ordering takes place which may include either or both rotational and translational rearrangements of the polymer. During the entire structural transformation, the fundamental lamellar unit remains undamaged. There may also be a possibility of the production of defects during the chain reordering. Reordering of polymer chains at lower fluences may give rise to a large number of polaronic defects. The increased ordering shows more delocalized  $\pi$  bands associated with better conductivity. A higher value of electrical conductivity after the irradiation may be related to the increased delocalization of  $\pi$ -electron and consequently the crystallinity leading to lower scattering of charge carriers [180][201]. But at further higher fluence (1×10<sup>12</sup> ions/cm<sup>2</sup>), the conductivity of the polymers is reduced due to increasing disorder by creating more defects.

Generally, the dc conductivity of any conjugated polymers consists of three components  $\sigma_B$ ,  $\sigma_H$  and  $\sigma_T$  [101]:

$$\sigma_{dc} = \sigma_B + \sigma_H + \sigma_T \quad (4.8)$$

In **Equation 4.8**, ' $\sigma_B$ ' describe the conductivity due to the intra-chain transport of charge carriers and can be explained with band conduction mechanism. This type of conductivity generally observed at high temperature. The second term ' $\sigma_H$ ' showed the conductivity due to hopping of charge carriers between polymer chains (inter-chain transport) and observed at intermediated temperature. The last type of conductivity ' $\sigma_T$ ' is due to the thermally activated tunneling and observed at low temperature. In the present study, the conductivity due to hopping of charge carriers between the polymer chains contributes more in the conduction mechanism. But in the lower temperature region, the conductivity becomes independent with temperature and the charge transport mechanism can be attributed to the tunneling between the polymer chains [202].

**Figure 4.39 (a) and (b)** show the variation of DC conductivity as a function of temperature ( $1000/T$  and  $T^{-1/4}$ ) in the temperature range of 230-350 K for the pristine as well as irradiated P3HT thin films. The conductivity data plotted against  $1000/T$  and  $T^{-1/4}$  manifests that the phonon-assisted hopping or thermally initiated jumps between the localized states are responsible for the carrier transport [173]. Therefore, Mott's 3D-VRH model is adopted to explain the temperature variation of dc conductivity in the present study. According to this model, DC conductivity ( $\sigma_{dc}$ ) can be expressed as **Equation 4.1**.

The plot of  $\log \sigma_{dc}$  versus  $(T^{-1})^m$  showed a straight line with  $m=1/4$  and also has a linearity factor of 0.99, which confirms the Mott's 3D VRH mechanism for  $T^{-1/4}$  type (where  $m$  has value  $1/4$ ) is more appropriate [203] to explain the conduction mechanism. The temperature region where **Equation 4.1** is valid should give [174][173] the activation energy as **Equation 4.2 & 4.3**, where **Equation 4.3** reveals that a plot of  $\log (E_A)$  versus  $\log T$  should have a straight line slope with  $-(m-1)$ .

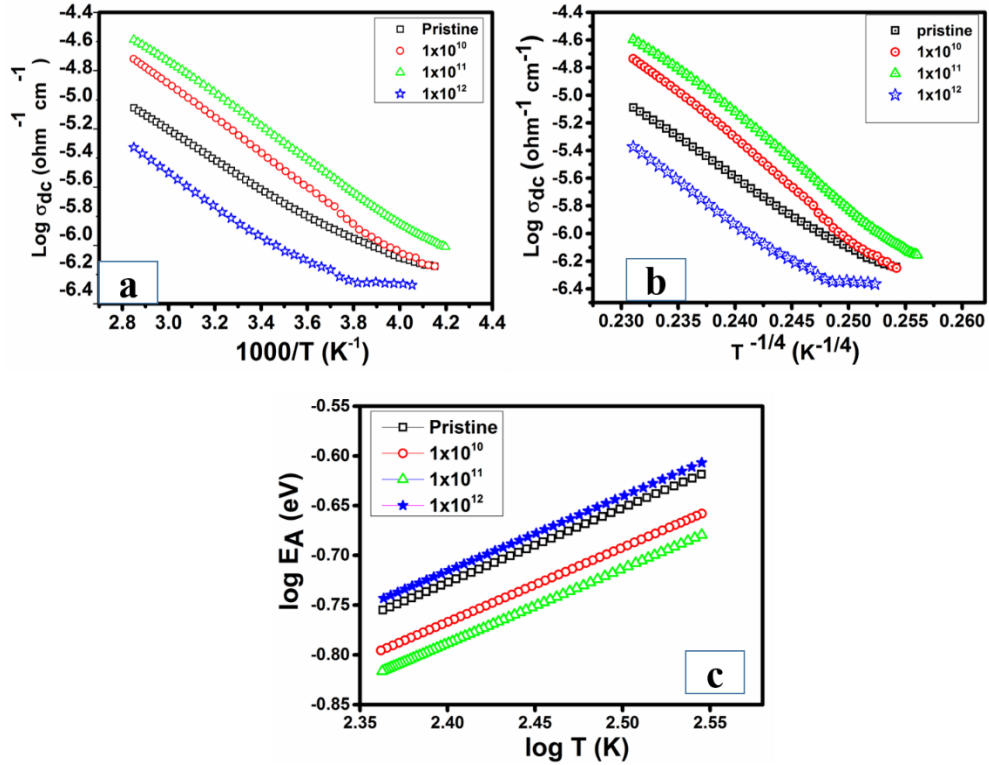


**Figure 4.29:** The plot of dc conductivity ( $\sigma_{dc}$ ) as a function of (a) reciprocal of temperature,  $1000/T$ ; (b)  $T^{-1/4}$  in the range of 230-350 K and (c) plot of log activation energy ( $E_A$ ) versus log temperature ( $T$ ) of pristine and irradiated P3HT thin films.

It can also be seen from **Figure 4.29** (c) that the activation energy is showing decrement with decreasing temperature. In the present case also, the variation of  $\log E_A$  with  $\log T$  (**Figure 4.29** (c)) shows the straight line with the value of  $m=1/4$  which may satisfy the variation of activation energy with temperature. This further supports the applicability of Mott's 3D VRH mechanism of type  $T^{-1/4}$  for the explanation of charge transport [173][174].

The effect of irradiation on different Mott's parameters such as characteristic temperature ( $T_0$ ), density of state at Fermi level [ $N(E_F)$ ], average hopping distance ( $R$ ), average hopping energy ( $W$ ) at room temperature associated with the transportation of charge have also been calculated using **Equation 4.4 to 4.7** and are presented in **Table 4.8**. All the parameters are in good agreement with previous reports [183][204][205].  $T_0$  obtained from the slop of  $\log \sigma_{dc}$  versus  $T^{-1/4}$  decreases with increase in fluences. These results are consistent with the requirement of the Mott's parameters that are  $\alpha R \gg 1$  and  $W \gg K_B T$  for the conductivity by hopping to distant sites. The temperature dependent

activation energy and calculated Mott's parameters indicate that the conduction mechanism for irradiated samples can be described successfully using 3D VRH model.

**Table 4.8:** Details of calculated Mott's parameters for pristine and 55 MeV Si<sup>4+</sup> ion beam irradiated P3HT thin films.

Fluences (ions/cm <sup>2</sup> )	Conductivity (ohm <sup>-1</sup> cm <sup>-1</sup> ) At 300 K	T <sub>0</sub> (K) (×10 <sup>8</sup> )	Activation Energy (eV) At 300 K	N(E <sub>f</sub> ) (cm <sup>-3</sup> eV <sup>-1</sup> ) (×10 <sup>19</sup> )	R (Å)	W (eV)	αR
0	2.48 × 10 <sup>-6</sup>	3.63	0.211	1.79	39.6	0.215	12.4
1×10 <sup>10</sup>	4.74 × 10 <sup>-6</sup>	2.52	0.195	2.58	36.1	0.197	11.3
1×10 <sup>11</sup>	7.33 × 10 <sup>-6</sup>	2.07	0.186	3.14	34.4	0.187	10.8
1×10 <sup>12</sup>	1.12 × 10 <sup>-6</sup>	4.06	0.220	1.6	40.8	0.293	12.8

### 4.3 Study of P3HT thin films under exposure of 1400 KeV Xe<sup>5+</sup> ions

Based on the results of two different ion beam (55 MeV Si<sup>4+</sup> and 90 MeV Ni<sup>7+</sup>) irradiation on P3HT thin films, Xe<sup>5+</sup> ion beam with 1400 KeV energy was used to analyse the effect of high mass ions with high incident ion fluences and low electronic and nuclear energy losses. Hence thin films were deposited using spin coating method over glass substrates. The thickness of the films was ~300 nm measured by Dektak Stylus surface profiler at IUAC, New Delhi. Thin films were irradiated by 1400 KeV Xe<sup>5+</sup> ions using Pelletron accelerator. The beam was incidence at normal to the film surface to carry out the irradiation process with different fluences, 1×10<sup>12</sup>, 1×10<sup>13</sup> and 1×10<sup>14</sup> ions/cm<sup>2</sup>. The S<sub>e</sub> and S<sub>n</sub> for the Xe<sup>5+</sup> ions in P3HT matrix is 746.3 eV/nm and 821.6 eV/nm, respectively. The range of Xe<sup>5+</sup> ions is 8905 Å calculated by SRIM 2008 software.

#### 4.3.1. Results and discussion

##### 4.3.1.1. Micro-Raman analysis

The Raman spectra for the pristine P3HT thin films is similar to **Figure 4.18** which, confirms the presence of all Raman active bands of P3HT. To analyse the effect of low energy ions on structural properties, range between 1350 to 1500 cm<sup>-1</sup> was chosen as the Raman peaks in this range is sensitive to π-electron delocalization or conjugation length

of P3HT molecules [151][152]. **Figure 4.30 (a)** is presenting the zoom image of two Raman active modes (situated at 1380 and 1448  $\text{cm}^{-1}$ ) for pristine and irradiated P3HT thin films to observe the irradiation effect. It can be observed from the **Figure 4.30 (a)** that the Raman intensity corresponding to C=C mode (1448  $\text{cm}^{-1}$ ) is decreasing with increasing incident ion fluences. The variation in the calculated FWHM corresponding to C=C mode (1448  $\text{cm}^{-1}$ ) is showing in **Figure 4.30 (b)** and found to be increased with incident fluences.

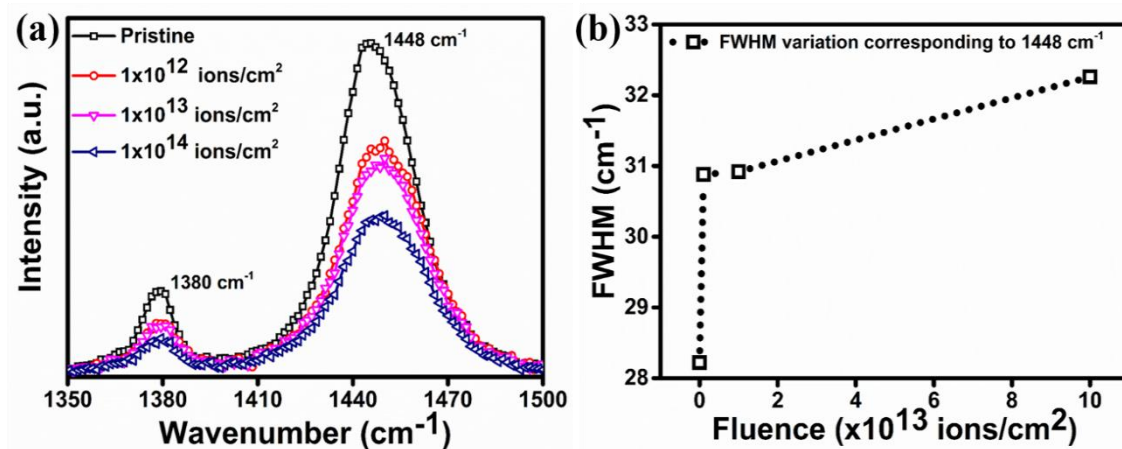


**Figure 4.30:** (a) Raman Spectra of pristine and irradiated P3HT thin films. (b) Variation of FWHM with incident fluences corresponding to 1448  $\text{cm}^{-1}$  Raman band.

This increment in the FWHM is not supporting the increased molecular ordering because for molecular ordering the FWHM of C=C mode should be decreased. Therefore, the reduced intensity and increased FWHM describing the damage is producing while, thin films were subjected to high mass ions with high fluences of incident ions. As high mass ions incident on target material, it will produce more damage to material as the interaction of ions with target will be large.

#### 4.3.1.2. UV-visible absorption spectroscopy

The absorption spectra for pristine and irradiated P3HT thin films is showing in the **Figure 4.31 (a)**. The spectra for the pristine films is showing the presence of all features as reported earlier [76]. While, for the film irradiated at the fluence of  $1 \times 10^{12}$  ions/ $\text{cm}^2$  the absorption peaks are less intense and slightly shifted toward lower wavelength. When,

the incident fluence is increased upto  $1 \times 10^{13}$  ions/cm<sup>2</sup>, the absorption features are started to be faded and large shift towards the lower wavelength was observed.

At the highest fluence ( $1 \times 10^{14}$  ions/cm<sup>2</sup>), it is observed that all the absorption features are vanished. Therefore, when, calculating the bandgap (**Figure 4.31 (b)**) for these films using Tauc's relation (**Equation 3.6**), it was observed that bandgap is also increasing after the irradiation (from 1.95 to 2.12 eV for the highest fluence at  $1 \times 10^{13}$  ions/cm<sup>2</sup>) with Xe<sup>5+</sup> ions of 1400 KeV energy. Hence, it is further concluded that irradiation of P3HT thin films with high mass ions at high fluences can produce damage.

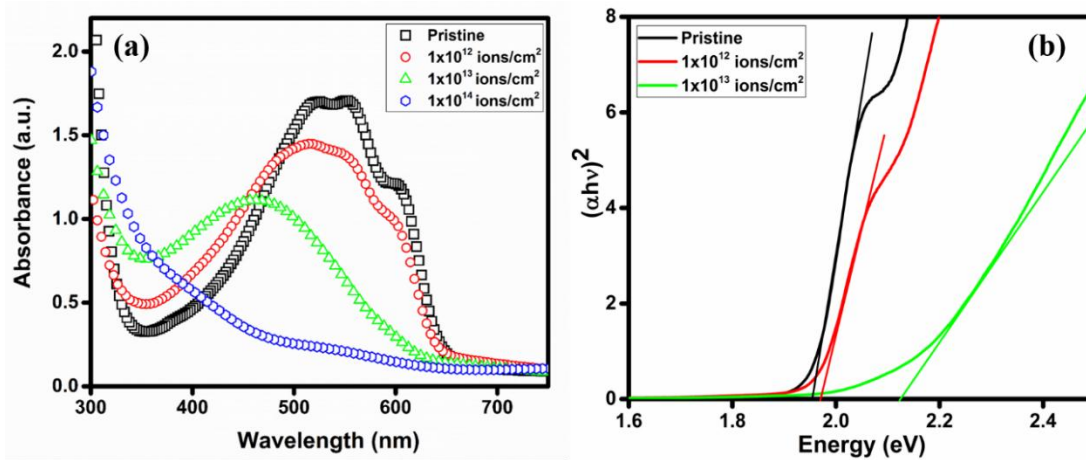


**Figure 4.31:** (a) Absorption spectra of pristine and irradiated P3HT thin films. (b) Tauc plot for determining the bandgap values of pristine and irradiated samples.

#### 4.3.1.3. Surface measurements

**Figure 4.32** show AFM images for pristine and irradiated P3HT thin films. AFM micrographs shows the surface texture is also dependent on the incident ion fluences. For the pristine thin film, small hill like features are observed while, at the highest fluence ( $1 \times 10^{14}$  ions/cm<sup>2</sup>) thin wire like structure are formed. Further, the RMS surface roughness for the pristine sample was observed to be  $\sim 8.22$  nm. It increases and attains a maximum RMS value of  $\sim 8.69$  nm for the film irradiated at  $1 \times 10^{12}$  ions/cm<sup>2</sup>. Further increase in incident ion fluence leads to a slight reduction in RMS roughness to  $\sim 7.81$  nm and 6.98 nm for the fluences of  $1 \times 10^{13}$  and  $1 \times 10^{14}$  ions/cm<sup>2</sup>. **Table 4.9** shows the surface roughness variation with incident fluence and found the variation in RMS value is very low.

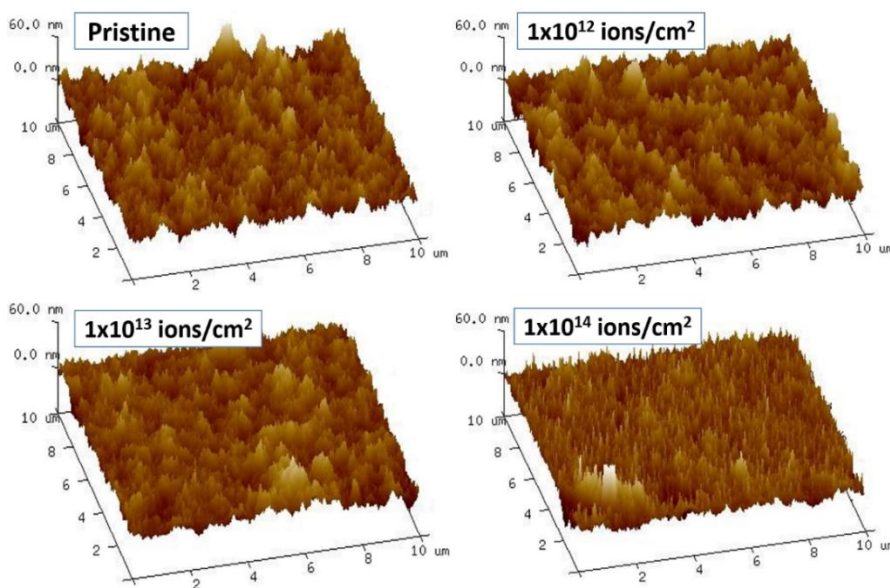


**Figure 4.32:** Images of AFM micrographs for pristine and irradiated P3HT thin films.

**Table 4.9:** Summary of roughness variation of irradiated P3HT thin films.

Fluence (ions/cm <sup>2</sup> )	Roughness (nm)
0	8.22
1×10 <sup>12</sup>	8.69
1×10 <sup>13</sup>	7.81
1×10 <sup>14</sup>	6.98

#### 4.4. Summary

In this chapter, the ion irradiation study of P3HT thin films is presented. Thin films of P3HT (thickness ~300 nm) were deposited using spin coating method and irradiated using three different ion beams (Ni<sup>7+</sup>, Si<sup>4+</sup> and Xe<sup>5+</sup>) at different fluences. The molecular ordering along with the increased crystallite size and conjugation length is observed with high energy ion beams at low fluences, while, at higher fluences ordering phenomenon starts to diminish due to bond breaking. While, using high mass ions with low energy (Xe<sup>5+</sup>), the structural damage is observed with increasing incident ion density.





# **Investigations on Modifications in PCBM Thin Films with Electronic Excitation by Taking Different Mass and Energy**

## ***5.1 Electronic excitation induced modifications of optical and morphological properties of PCBM thin films under 90 MeV Ni<sup>7+</sup> ion irradiation***

The other material PCBM acts as an acceptor and charge carrier transporting material [78][79]. PCBM was synthesized in 1995 by Hummelen et al. [206] and now is extensively utilized for OSC because of its good solubility in different organic solvents, higher electron mobility, high thermal stability and higher electron affinity [78][207]. Several attempts have been done to improve the performance of OPVs and device stability using different perturbations such as using different concentration of PCBM material, using different solvents, annealing etc. The SHI irradiations is a beneficial tool to customize the properties of fullerene [208][209][108][210] as well as fullerene derivatives so that it can be used at nano/atomic scale. The modifications produced by SHI such as fabrication of conducting nanowires, alteration of optical properties, structural changes and many others are very much interesting. Hence, many studies show that the properties of fullerene molecules and its derivatives can be altered using energetic ion irradiation.

Under this study, thin films of PCBM, deposited using spin coating method on glass and double side polished substrates, were irradiated by 90 MeV Ni<sup>7+</sup> ions using Pelletron accelerator. CB was used as a solvent for PCBM solution. The beam was incidence at normal to the film surface to carry out the irradiation process with different fluences ranging from  $1 \times 10^9$  to  $1 \times 10^{11}$  ions/cm<sup>2</sup>. The  $S_e$  and  $S_n$  for the 90 MeV Ni<sup>7+</sup> ions in PCBM matrix is 7736 eV/nm and 13.19 eV/nm, respectively. The range of Ni<sup>7+</sup> ions is 16.59  $\mu\text{m}$  calculated by SRIM 2008 software.

### ***5.1.1. Results and discussion***

#### ***5.1.1.1. UV-visible absorption spectroscopy***

**Figure 5.1** shows the absorption spectra of pristine and 90 MeV Ni<sup>7+</sup> irradiated thin films of PCBM on glass substrate. The incident fluences were  $1 \times 10^9$ ,  $3 \times 10^9$ ,  $1 \times 10^{10}$ ,  $3 \times 10^{10}$  and  $1 \times 10^{11}$  ions/cm<sup>2</sup>. The absorption spectrum of PCBM thin film is showing the absorption in the ultraviolet region (<400 nm wavelength) which is similar to the parent C<sub>60</sub> molecule. The absorption peak of PCBM films was found at 335 nm in the form of intense peak which, arises due to interband transition among the  $\pi$  orbitals. A tail was also observed in the absorption spectra of pristine and irradiated thin films which is extending to 700 nm.

This tail is not due to light scattering or some other experimental facts. The absorption peak at 335 nm was found to be present even after irradiation at highest fluences ( $1 \times 10^{11}$  ions/cm<sup>2</sup>) which gives some indications that the lamellar structure of PCBM molecule is not destroyed due to high energy irradiation. **Figure 5.2** shows the graph between  $(\alpha h\nu)^{1/2}$  and  $h\nu$  (photon energy) which depict the variation in optical bandgap of PCBM thin films after irradiation. The optical bandgap (energy gap) between the HOMO and the LUMO, was evaluated using following Tauc's relation (**Equation 3.6**) [211][212][136].

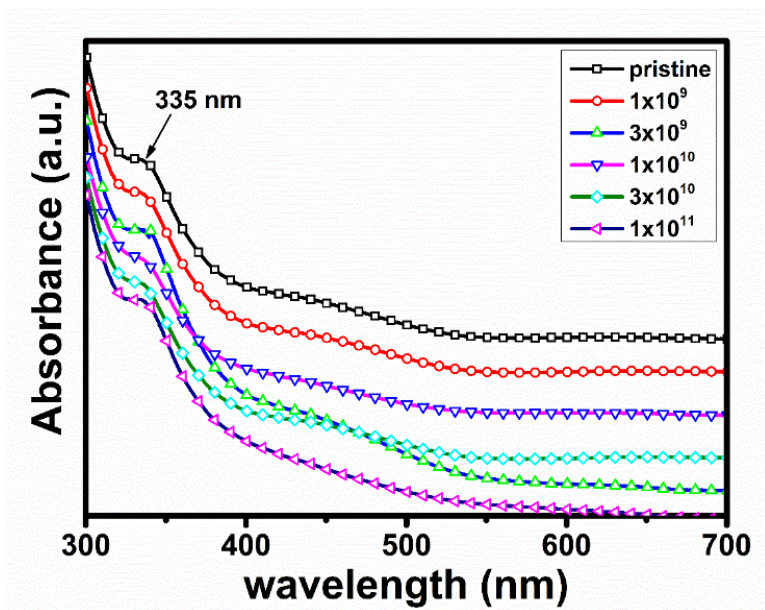


**Figure 5.1:** UV-visible absorption spectra of pristine and 90 MeV Ni<sup>7+</sup> ion beam irradiated PCBM thin films.

From **Figure 5.2**, the measured optical bandgap of pristine film is 2.1 eV. At a fluence of  $1 \times 10^{10}$  ion/cm<sup>2</sup>, the bandgap is decreased to 2.0 eV. After irradiation of thin films at highest fluence ( $1 \times 10^{11}$  ion/cm<sup>2</sup>), the energy gap is evaluated to be 1.8 eV. The effect of high energy ion beam on the optical bandgap of PCBM thin films is summarized in **Table 5.1**. This decrease in bandgap might be due to the modification of the HOMO or the LUMO molecular levels of PCBM molecules. High energy ions deposit kinetic energy along the ion trajectory. This energy is sufficient to produce the high density radicals in the host materials due to gelation resulting via cross-linking reactions which, leads to the polymerization reaction of PCBM molecules [109]. Many groups have reported the

polymerization in fullerene and its derivatives under different perturbations and explained with the help of 2 + 2 cycloaddition reaction in which, two carbon double bonds on adjacent C<sub>60</sub> molecules (which are parallel oriented) are broken and reform as single bond between the molecules [113][111][112][213]. These polymerization reactions results in the modifications of molecular orbitals of PCBM.

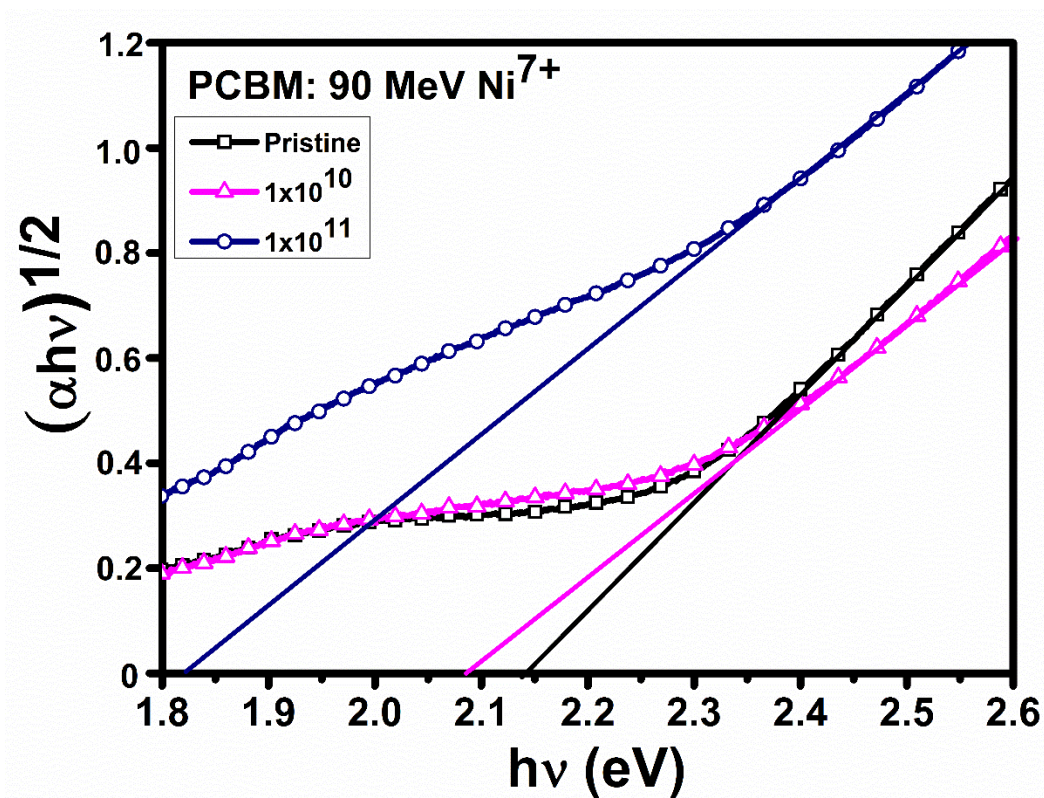


**Figure 5.2:** Variation in optical bandgap of pristine and irradiated PCBM films.

**Table 5.1:** Summary of variation in optical bandgap.

Fluences (ions/cm <sup>2</sup> )	Bandgap (eV)
Pristine	2.1
1×10 <sup>10</sup>	2.0
1×10 <sup>11</sup>	1.8

### 5.1.1.2. FTIR spectroscopy

The chemical composition of pristine and irradiated thin films of PCBM were observed by FTIR spectroscopy. **Figure 5.3** shows the measured FTIR spectra of pristine and 90 MeV Ni<sup>7+</sup> swift heavy ions irradiated thin films of PCBM on double sided silicon substrate at different fluences. It clearly reveals the presence of parent C<sub>60</sub> molecules (612 cm<sup>-1</sup> and 1436 cm<sup>-1</sup>) and Carbon–Hydrogen (C-H) single bond bending (739 cm<sup>-1</sup>). Carbon–Oxygen (C-O) single bond (1107 cm<sup>-1</sup>) vibration and Carbon-to-Oxygen (C=O) double bond stretching mode (1733 cm<sup>-1</sup>) were also observed by FTIR spectra.

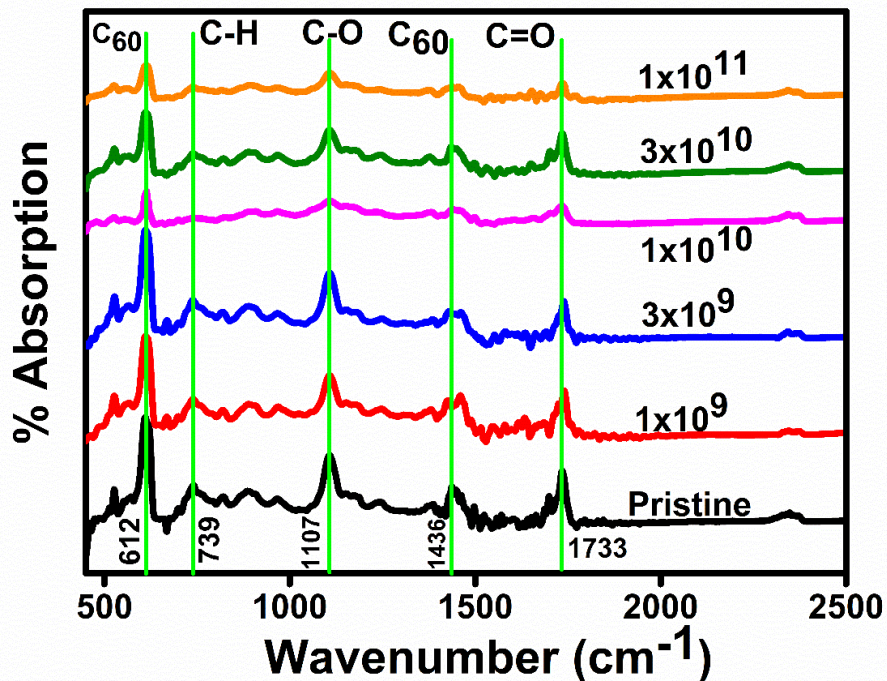


**Figure 5.3:** The measured FTIR spectra of pristine and irradiated PCBM thin films.

**Figure 5.4** shows the decrease in the intensity of peaks (C<sub>60</sub>, C-O, C=O) with the increase in the irradiation fluence. From the **Figure 5.4**, it is depicted that with ion irradiation at highest fluence (1×10<sup>11</sup> ions/cm<sup>2</sup>), the band intensity corresponding to different vibration is decreased in a fraction with respect to the intensity of pristine film bands. The considerable decrease in the intensity of C-O bond and C=O bond indicates that the side chain of butyric acid methyl ester and phenyl ring were also affected due to high energy ion irradiation but structure is not completely destroyed. The abrupt decrease in the

intensity of C<sub>60</sub> cage in comparison with the other peaks is observed. It may be due to the effective chain reaction due to polymerization which was induced by high energy ion irradiation. The electronic excitation, induced by the high energy ions, produces radicals in C<sub>60</sub> molecules. These radicals initiates the cycloaddition reactions in fullerene molecule which leads to the chain reaction and polymerization in PCBM [113][111][112][213].

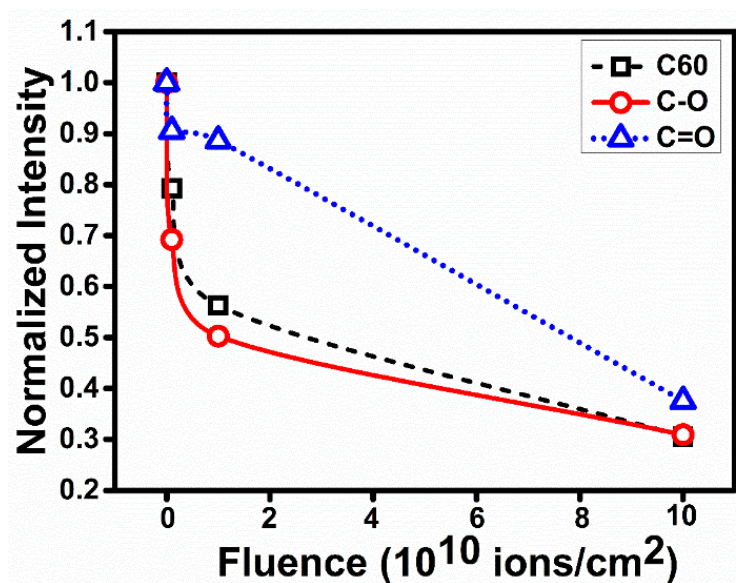


**Figure 5.4:** Variation of FTIR peak intensity of pristine and irradiated PCBM thin films.

### 5.1.1.3. Surface analysis

The surface morphology of pristine and ion irradiated PCBM thin films on double sided silicon substrate was examined by AFM in tapping mode and is shown in **Figure 5.5**. It is clear from the figure that the surface morphology of PCBM thin films also considerable affected by the high energy ion irradiation. The films irradiated with increasing fluences shows that surface roughness is increased from 0.9 nm to 5.0 nm for the fluence  $1 \times 10^{10}$  ions/cm<sup>2</sup>. After that, at the fluence of  $3 \times 10^{10}$  ions/cm<sup>2</sup> roughness was decreased to 0.8 nm and at highest fluence ( $1 \times 10^{11}$  ions/cm<sup>2</sup>), the roughness was minimum at a value of 1.4 nm. After irradiation at a fluence of  $1 \times 10^{10}$  ions/cm<sup>2</sup>, the energy loss of incoming ions over  $1 \times 1 \text{ cm}^2$  area of film is sufficient to releases the stress in the film and surface of film starts to become smooth after this fluence. The RMS roughness of pristine and irradiated thin films are listed in **Table 5.2**. The rougher surface might be an advantage for increasing

contact area of active layer with top metal contact in OSC devices which can increase the short circuit current density [214] and in this respect, film irradiated at a fluence of  $1 \times 10^{10}$  ions/cm<sup>2</sup> shows optimum results. It has also been reported that for OPV devices morphology is also very important. The PCBM in the blend of P3HT: PCBM for organic solar cells devices can affect the efficiency because of morphology.

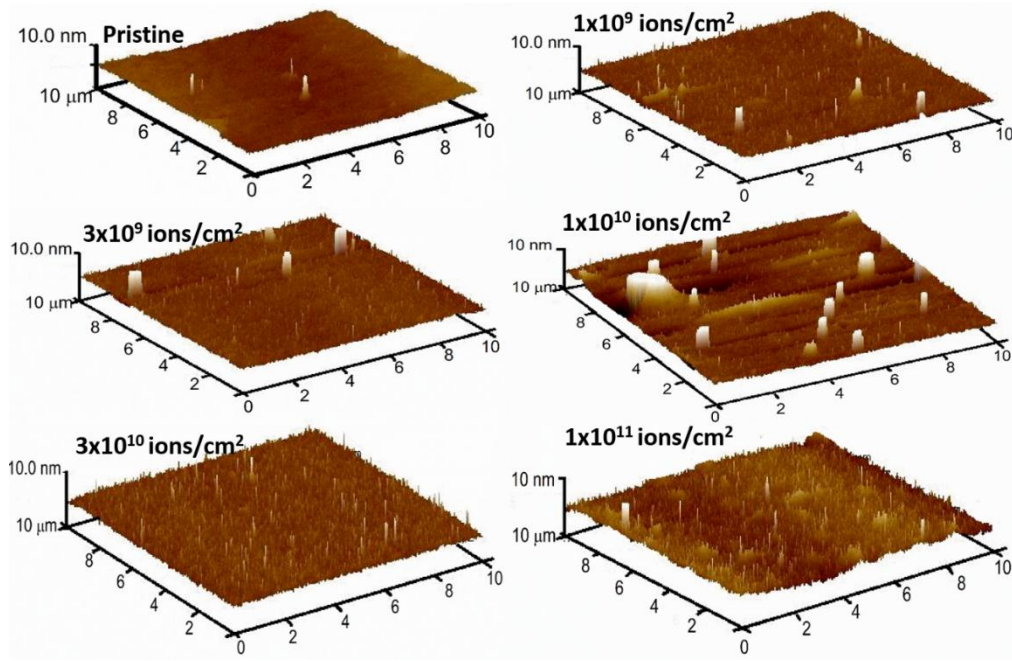


**Figure 5.5:** Three dimensional AFM micrographs of pristine and irradiated thin films of PCBM.

**Table 5.2:** Summary of measured roughness of pristine and irradiated PCBM thin films.

Fluences (ions/cm <sup>2</sup> )	Roughness (nm)
Pristine	0.9
$1 \times 10^9$	1.1
$3 \times 10^9$	1.2
$1 \times 10^{10}$	5.0
$3 \times 10^{10}$	0.8
$1 \times 10^{11}$	1.4

## 5.2 Influence of high energy ion (55 MeV Si<sup>4+</sup>) irradiation on fullerene derivative (PCBM) thin films

In order to investigate the impact of high energy, 55 MeV Si<sup>4+</sup> ion beam have been used to irradiate the thin films of PCBM and analyzed using different characterization techniques before irradiation as well as after irradiation. The optical, structural and morphological modifications due to high energy deposition have been studied and observed that the SHI irradiation induced polymerization reactions may causes to the alteration in the properties. This study is also given a glimpse over the applicability of PCBM material in high radiation zones such as in space.

Thin films of PCBM, deposited using spin coating method on glass and double side polished substrates and then irradiated by 55 MeV Si<sup>4+</sup> ions. The beam was incidence at normal to the film surface to carry out the irradiation process with different fluences ranging from  $1 \times 10^{10}$  to  $1 \times 10^{12}$  ions/cm<sup>2</sup>. The S<sub>e</sub> and S<sub>n</sub> for the 55 MeV Si<sup>4+</sup> ions in PCBM matrix is 3146 eV/nm and 2.942 eV/nm, respectively. The range of Si<sup>4+</sup> ions is 16.73 μm calculated by SRIM 2008 software.

### 5.2.1. Results and discussion

#### 5.2.1.1. UV-visible absorption spectroscopy

The optical absorption properties of PCBM thin films have been studied using UV–visible absorption spectra. **Figure 5.6** shows the UV–visible absorption spectra of pristine as well as irradiated PCBM thin films at different fluences in the wavelength range of 300–800 nm. Due to the inter band transition among the π orbitals, a small absorption peak at 335 nm (ultra-violet region) arises, shown in **Figure 5.6**. The existence of less intense peak (335 nm) at the highest fluence of  $1 \times 10^{12}$  ions/cm<sup>2</sup> with respect to the pristine peak represents the sustainability of the structure of PCBM molecules after high energy deposition. The inset of **Figure 5.6** shows the Tauc's plot of pristine and irradiated PCBM thin films [136][212][211]. Tauc's plot is used to analyse the effect of irradiation on optical bandgap at the fluences of  $1 \times 10^{10}$  ions/cm<sup>2</sup> and  $1 \times 10^{11}$  ions/cm<sup>2</sup>. The bandgap at the highest fluence of  $1 \times 10^{12}$  ions/cm<sup>2</sup> could not be measured as at the highest fluence, the edge of absorption spectrum is not in the bandgap range which might be due to the more damage produced at this fluence and amorphization takes place. For the pristine PCBM film, the



indirect bandgap calculated from Tauc's plot is 2.1 eV. This optical bandgap is decreased up to 1.8 eV at the fluence of  $1 \times 10^{11}$  ions/cm<sup>2</sup> which is same ( $\sim 1.8$  eV) as previously reported [215] bandgap at this fluence and it decreased to 1.7 eV at the fluence of  $1 \times 10^{10}$  ions/cm<sup>2</sup>. The variation of bandgap has been listed in **Table 5.3**.

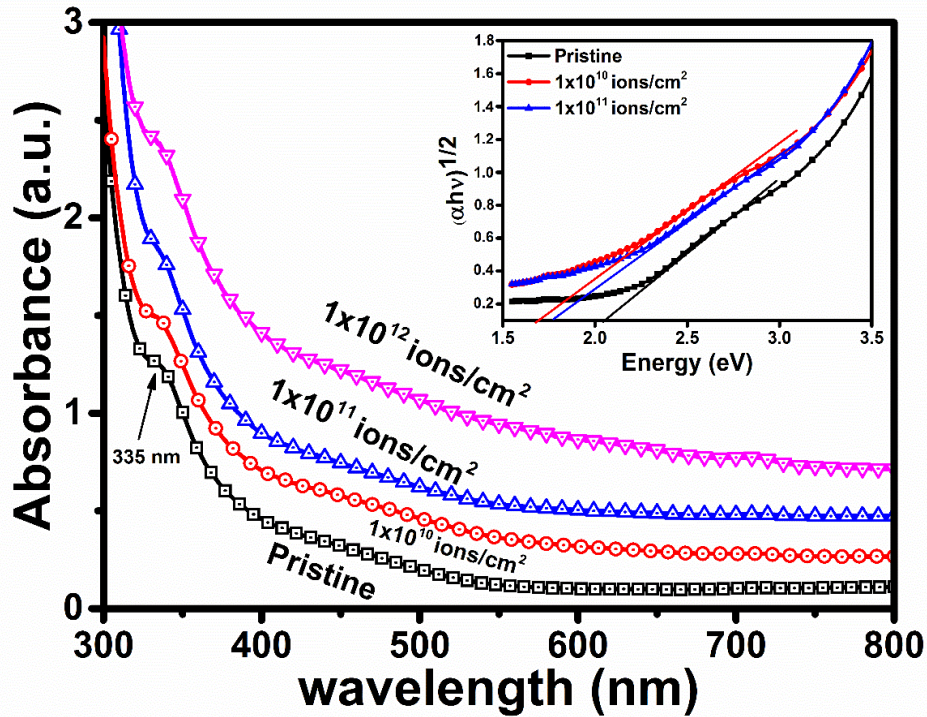


**Figure 5.6:** UV-visible absorption spectra of pristine and irradiated PCBM thin films. The inset shows the Tauc's plot of pristine and irradiated thin films at fluences of  $1 \times 10^{10}$  ions/cm<sup>2</sup> and  $1 \times 10^{11}$  ions/cm<sup>2</sup>.

This decrease in the optical bandgap at low fluences is presumably due to the result of polymerization reactions which are generated by high density radical [109]. At the higher fluences, such as  $1 \times 10^{11}$  ions/cm<sup>2</sup>, these polymerization reactions may also be affected due to increased energy deposition with increased incident fluences, which might be the cause of greater decrease in bandgap at lower fluences. These high-density radicals are produced due to the high energy deposition of incident ions. The polymerization reactions in fullerene is believed to be of 2+2 cycloaddition reaction (**Figure 5.7 (a) and (b)**). When,

two double bonds of fullerene molecules face each other, it forms covalent bond between fullerene molecules which is rectangular in appearance [104][113][111][112][213]. These polymerization reactions induced by deposited energy leads to the molecular orbital modifications of PCBM films. At the higher fluence i.e.  $1 \times 10^{12}$  ions/cm<sup>2</sup> the polymerization may not be possible as the irradiations events overlap with each other which cause the amorphization. Due to multiple events at each place, the absorption intensity increased.

**Table 5.3:** Summary of variation in the optical bandgap, surface RMS roughness and contact angle of pristine and 55 MeV Si<sup>4+</sup> ion beam irradiated PCBM thin films.

Fluences (ions/cm <sup>2</sup> )	Bandgap (eV)	Roughness (nm)	Contact Angle (°)
Pristine	2.1	0.9	88.2
$1 \times 10^{10}$	1.7	-	-
$1 \times 10^{11}$	1.8	1.6	90.3
$1 \times 10^{12}$	-	2.3	92.4

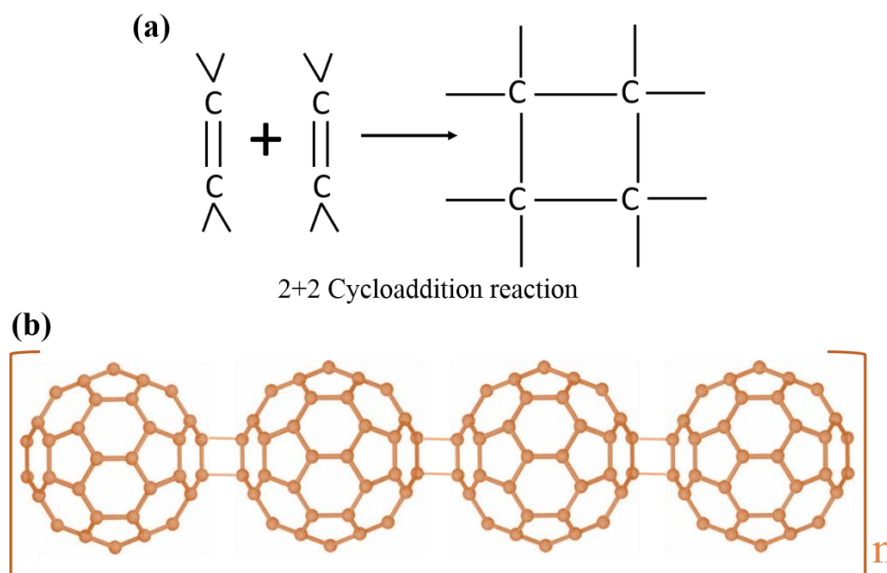


**Figure 5.7:** (a) Schematic of “2+2 cycloaddition” reaction of adjacent molecules where carbon double bonds faces each other. (b) Schematic of the expected polymerized fullerene molecules.

### 5.2.1.2. FTIR spectroscopy

The modifications in chemical compositions of IR active modes of PCBM thin films were investigated using FTIR spectroscopy. **Figure 5.8** is showing the IR spectra on silicon substrate of PCBM thin films before irradiation as well as after irradiation. The observed band at  $1733\text{ cm}^{-1}$  in **Figure 5.8** is corresponding to carbon-to-oxygen (C=O) double bond stretching mode. The carbon-oxygen (C–O) single bond vibration mode at  $1107\text{ cm}^{-1}$  and carbon- hydrogen (C–H) single bond bending mode at  $739\text{ cm}^{-1}$  were also found to be presented by FTIR spectra. The observed band at  $612\text{ cm}^{-1}$  and  $1436\text{ cm}^{-1}$  in **Figure 5.8** confirms the existence of parent molecule  $\text{C}_{60}$ . After irradiation, the decrease in the intensity of IR absorption spectra showing the degradation of the PCBM. The variation in the normalized areal peak intensity was also calculated using different IR bands and described in **Figure 5.9**. It has been observed from the **Figure 5.9** that the areal intensity corresponding to the  $612\text{ cm}^{-1}$  and  $1107\text{ cm}^{-1}$  peaks which are attributed to the  $\text{C}_{60}$  and C–O bands of PCBM thin films decreases with increased fluences.

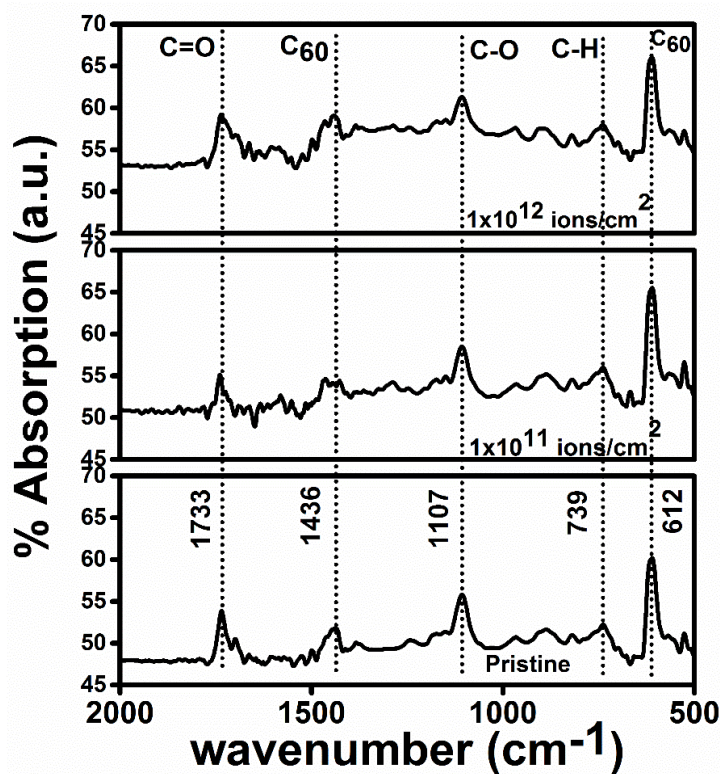


**Figure 5.8:** The measured FTIR spectra of pristine and irradiated PCBM thin films.

The measured variation of the normalized areal intensity with incident ion fluences confirmed that the parent molecule  $C_{60}$  and side chains are also affected by high energy ion beam irradiation as incident ion deposited its energy and produced damage in the target material. The splitting of the IR band at  $1436\text{ cm}^{-1}$  which is corresponding to the fullerene  $C_{60}$  molecule was observed after irradiation at the higher two fluences ( $1 \times 10^{11}$  and  $1 \times 10^{12}$  ions/cm<sup>2</sup>). Energetic ions produce radicals after high energy deposition, these radicals are responsible for the cycloaddition reactions that converts two intramolecular  $sp^2$  double bonds in two intermolecular  $sp^3$  single bonds in fullerene molecules and polymerization of fullerene molecules occur at low fluences. The abrupt and large decrease in the normalized areal intensity of the peaks corresponding to  $C_{60}$  and C–O bands at the highest fluence ( $1 \times 10^{12}$  ions/cm<sup>2</sup>) indicates the initiated damage by high energy ions which is due to the multiple events of ion irradiation as discussed earlier. This damage produced by energetic ions leads to the amorphization in the PCBM film.

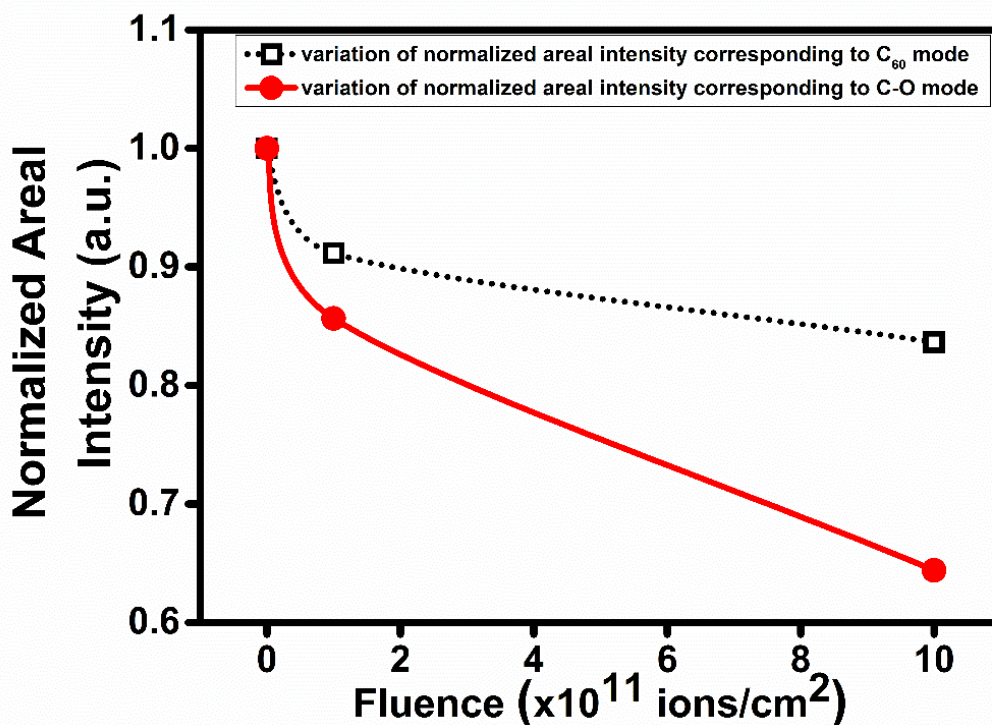


**Figure 5.9:** Normalized areal intensity variation of FTIR peak for pristine and irradiated PCBM thin films.

### 5.2.1.3. Micro-Raman analysis

Raman spectroscopy technique is a very efficient tool to analyse the structural changes induced by high energy ion irradiation in the host matrix. PCBM is somewhat different from fullerene  $C_{60}$  as the side chain in the PCBM grafted onto  $C_{60}$  molecule which, brings the advantages that PCBM is more soluble in common organic solvents in contrast to  $C_{60}$ . A less number of studies have been published on Raman analysis of PCBM [216][217][218][219]. **Figure 5.10** depicts the Raman spectra of as-deposited PCBM film along with ion beam irradiated thin films of PCBM at different fluences. There are three Raman vibration modes corresponding to the wavenumber of  $1428\text{ cm}^{-1}$ ,  $1462\text{ cm}^{-1}$  and  $1568\text{ cm}^{-1}$  for the pristine PCBM thin film. Among these three bands, the most intense band located at  $1462\text{ cm}^{-1}$  is corresponding to  $A_g(2)$  “pentagonal pinch mode” analogous to that of  $C_{60}$  molecule.

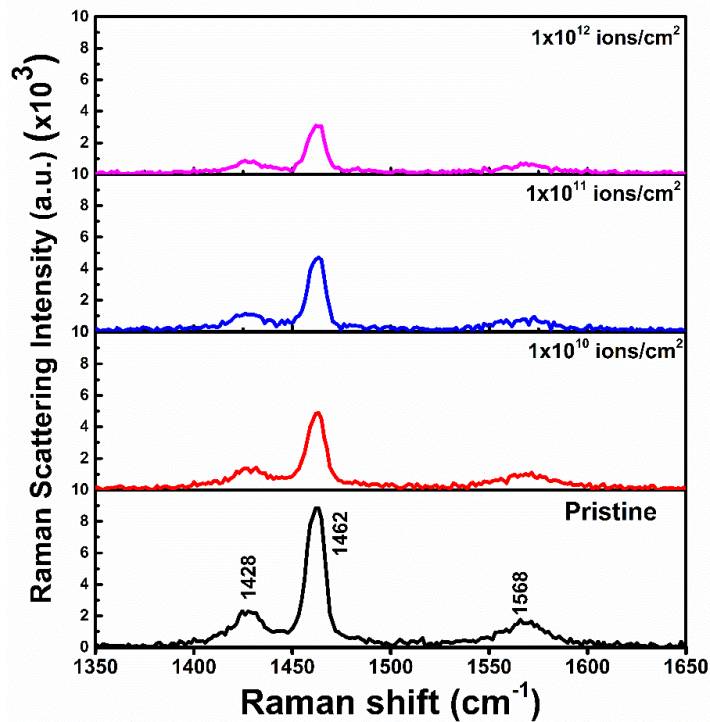


**Figure 5.10:** Raman spectra of pristine and 55 MeV  $Si^{4+}$  ion beam irradiated thin films of PCBM.

These Raman-active vibrational modes showing the progressive decrement in the intensity as the incident ion fluence increases, but it is not faded entirely even after

irradiating at higher fluence. The energy deposition by high energy ions results in the splitting of the PCBM molecules which is further confirmed by decreased intensity of Raman peaks with incident high energy ions. At high fluences, the energy deposited is large, so the number of breaking molecule will be large. But PCBM is not completely amorphized at highest fluence ( $1 \times 10^{12}$  ions/cm<sup>2</sup>) due to the overlap of ion tracks because of the small electronic energy loss (3146 eV/nm) of 55 MeV Si<sup>4+</sup> ion beam in PCBM film. The subsided intensity of Raman peaks can be concluded by Thermal Spike Model. This model explains that when, energetic ions are incident on the target film, they transfer their energy by electron-phonon coupling to the material in  $10^{-13}$ – $10^{-12}$  s. Due to the energy transferred to the material, the lattice temperature increases up to  $\sim 10^4$  K. After a certain threshold of electronic energy loss, a molten state is formed within the nanometre region for a very short duration of  $10^{-12}$ – $10^{-11}$  s. This molten state then quenches with the very fast rate of  $10^{14}$  K/s by thermal conduction. This rapid quenching results in the modified material within the cylindrical region [154][85]. To observe the damage trend, the variation of normalized areal intensity with incident fluences for all peaks is showing in **Figure 5.11** and confirms that more damage is produced at higher fluence due to overlapping effect.

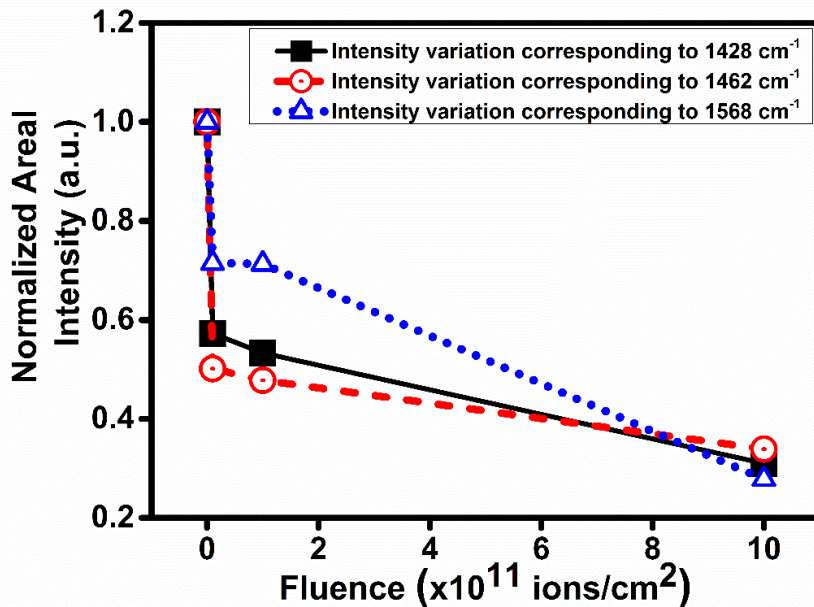


**Figure 5.11:** Curve between the normalized areal intensity of three Raman modes (1428 cm<sup>-1</sup>, 1462 cm<sup>-1</sup>, 1568 cm<sup>-1</sup>) with different fluences of 55 MeV Si<sup>4+</sup> ions.

#### 5.2.1.4. Surface analysis

To study the surface morphological modification, AFM has been performed. **Figure 5.12 (a)** represents the 2D AFM micrographs of PCBM thin films before as well as after irradiation. The AFM images were obtained in tapping mode on a double side polished silicon substrates. The measured RMS roughness of as-deposited film, as well as post-irradiated thin film, has been summarized in **Table 5.3**. It has been investigated that, the roughness of PCBM film before the irradiation (pristine) was 0.9 nm. When, the incident ion fluence was increased at  $1 \times 10^{11}$  ions/cm<sup>2</sup>, the film's surface roughness was found to be increased to 1.6 nm which is further increased up to 2.3 nm for the fluence of  $1 \times 10^{12}$  ions/cm<sup>2</sup>. The incident ions created the ion tracks into the film and produce the ion beam irradiation induced sputtering which causes the increased surface roughness.

To analyze the surface modifications due to ion impact, further, the contact angle between the films surface and the water droplet has been measured for pristine as well as irradiated PCBM thin films. The contact angle generally described by using Young's equation and quantifies the wetting property of a solid surface using liquid drop. The Young's theory has been described in section 3.4.7 in detail. **Figure 5.12 (b)** shows the snapshot of the contact angle measurements of PCBM thin films. For pristine film, the measured angle between water droplet and PCBM film surface is 88.2° which, shows the hydrophilic nature (<90°) of the pristine PCBM thin film. When, thin films were irradiated with high energy ion beam, it affected the surface of the film and the angle between the water droplet and PCBM film surface increased to 90.3° and 92.4° for the fluences of  $1 \times 10^{11}$  and  $1 \times 10^{12}$  ions/cm<sup>2</sup>, respectively. This small increase in contact angle after high energy ion irradiation depict that there is a slight change in the wettability of the film due to high energy ions. The variation of contact angle with incident ion fluences has been summarized in **Table 5.3**.

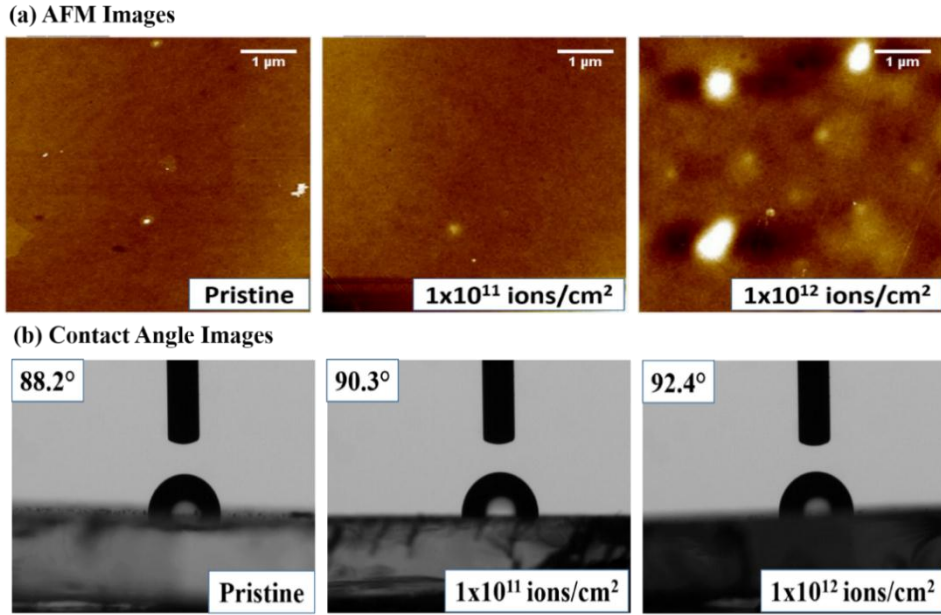


**Figure 5.12:** (a) Two-dimensional (2D) AFM height images and (b) Contact angle images of a water droplet with pristine and ion irradiated PCBM films at the fluences of  $1 \times 10^{11}$  ions/cm<sup>2</sup> and  $1 \times 10^{12}$  ions/cm<sup>2</sup>.

### 5.3 Study of fullerene derivative (PCBM) thin films under exposure of 1400 KeV Xe<sup>5+</sup> ions

After analyzing the effect of two different ion beam (55 MeV Si<sup>4+</sup> and 90 MeV Ni<sup>7+</sup>) on PCBM thin films, Xe<sup>5+</sup> ion beam with 1400 KeV energy was used to analyze the effect of high mass ions with high fluences. While, the value of  $S_e$  and  $S_n$  are almost equal but less than the value for other two ion beams (55 MeV Si<sup>4+</sup> and 90 MeV Ni<sup>7+</sup>). Hence, thin films of PCBM were deposited using spin coating method over glass and double side polished substrates. The thickness of the deposited films was measured using Dektak Stylus surface profiler and was around to be 100 nm. These thin films were then subjected to irradiation with 1400 KeV energy of Xe<sup>5+</sup> ion beam. Fluences,  $1 \times 10^{12}$ ,  $1 \times 10^{13}$  and  $1 \times 10^{14}$  ions/cm<sup>2</sup>, were used for irradiation process. The  $S_e$  and  $S_n$  for Xe<sup>5+</sup> ion in PCBM matrix is 1344 eV/nm and 1366 eV/nm, respectively. The range of Xe<sup>5+</sup> ions is 5122 Å calculated by SRIM 2008 software.

#### 5.3.1. Results and discussion:



### 5.3.1.1. Micro-Raman spectroscopy

**Figure 5.13** represents the Raman spectra of as deposited and ion beam irradiated PCBM thin films. Studies of PCBM based on Raman analysis are very less reported [216][217][218][219]. There are three Raman active vibration mode corresponding to 1428, 1462 and 1568  $\text{cm}^{-1}$  wavenumber are observed in the Raman spectra for the pristine PCBM film. The most intense band (1462  $\text{cm}^{-1}$ ) is corresponding to  $A_g(2)$  “pentagonal pinch mode” which is analogous to that of  $C_{60}$  molecule. After the irradiation with high mass ions ( $\text{Xe}^{5+}$ ) at high fluence and low energy, the intensity of Raman modes is decreasing. On the other hand, all the band started destroyed at the fluence of  $1 \times 10^{13}$  ions/ $\text{cm}^2$ . These bands started to merge and two peaks are appearing after the irradiation with the fluence of  $1 \times 10^{13}$  ions/ $\text{cm}^2$ . While, at the highest fluence,  $1 \times 10^{14}$  ions/ $\text{cm}^2$ , all bands are merged and two broad bands around at 1435  $\text{cm}^{-1}$  and 1564  $\text{cm}^{-1}$  start evolving. These two broad bands may be the characteristic D and G bands of a-C. Hence, it is observed that the irradiation with high mass ions with low energy are destroying the structure of the PCBM material.

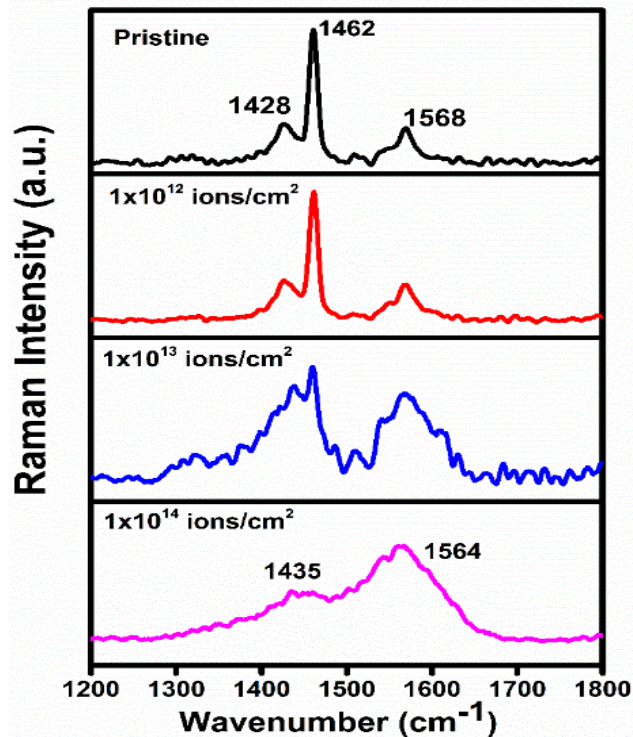


**Figure 5.13:** Raman Spectra of pristine and irradiated PCBM thin films.

### 5.3.1.2. UV-visible absorption spectroscopy

To investigate the effect of high mass ions on optical absorption properties, UV-visible absorption measurement have been done. **Figure 5.14** showing the absorption spectra of pristine and irradiated PCBM thin films. The absorption spectra of pristine films is showing a small peak around 335 nm which is due to the inter band transition among  $\pi$ -orbitals. After the irradiation at the fluence of  $1 \times 10^{12}$  ions/cm<sup>2</sup>, the absorption feature is faded. Further increasing the incident fluences upto  $1 \times 10^{13}$  and  $1 \times 10^{14}$  ions/cm<sup>2</sup>, the absorption features has vanished which is indicating the produced structural damage after irradiation.

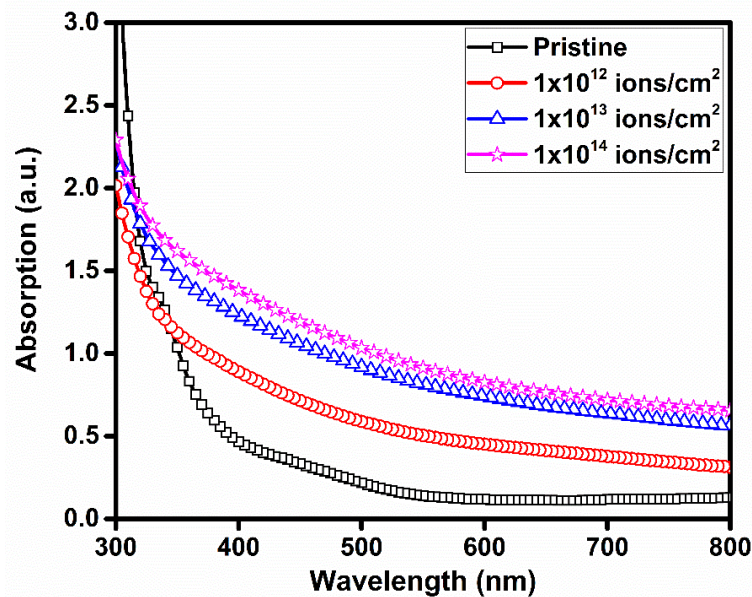


**Figure 5.14:** Absorption spectra of pristine and irradiated PCBM thin films.

### 5.3.1.3. Surface analysis

The modifications produced by irradiation has been observed using AFM microscopy. **Figure 5.15** represents the AFM images of pristine and irradiated PCBM thin films. The measured RMS roughness for the pristine sample was 0.9 nm. When, the film was irradiated at the highest fluence,  $1 \times 10^{14}$  ions/cm<sup>2</sup>, surface roughness increased and attains its maximum value of 1.42 nm. When, the energetic ions incident on the target surface, it will lead to the ion beam induced sputtering which causes the increased surface roughness.

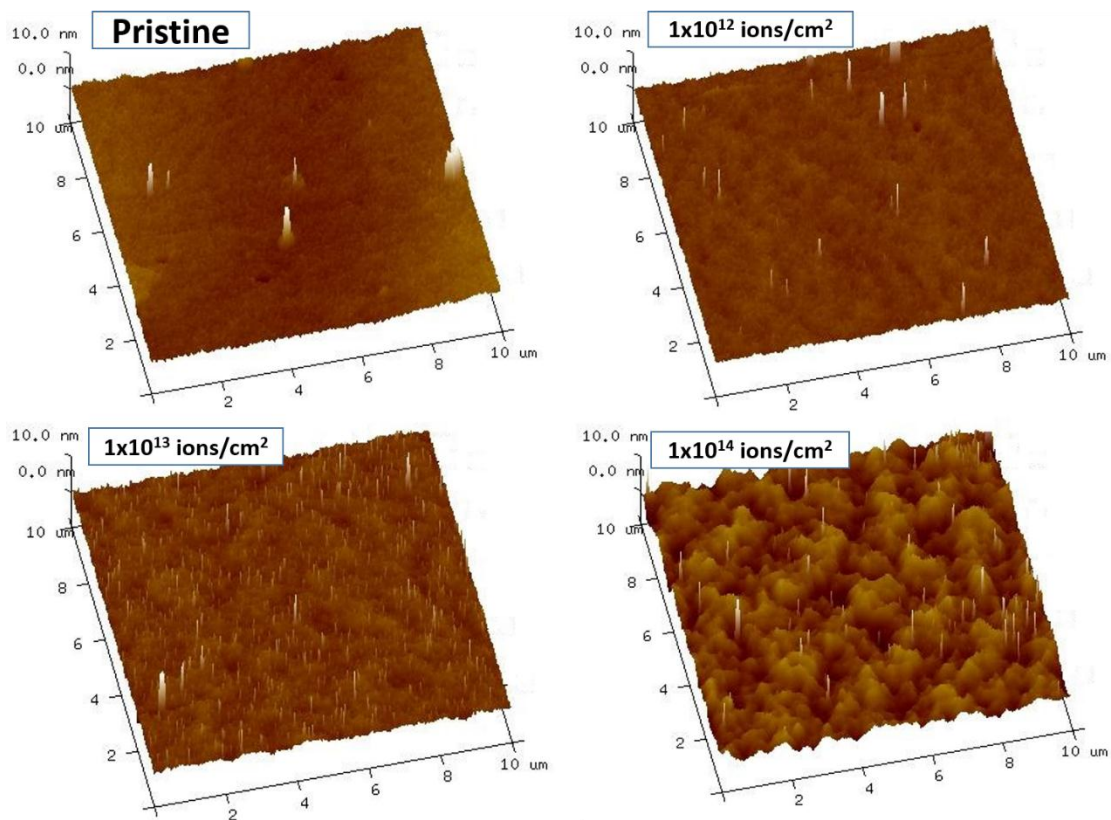


**Figure 5.15:** Three dimensional AFM micrographs of pristine and irradiated PCBM thin films.

#### 5.4. Summary

In this chapter, the ion irradiation study of fullerene derivative (PCBM) thin films is presented. Thin films of PCBM were deposited using spin coating method with the thickness  $\sim 100$  nm and irradiated using three different ion beams ( $\text{Ni}^{7+}$ ,  $\text{Si}^{4+}$  and  $\text{Xe}^{5+}$ ) with different electronic energy losses. The optical analysis shows the decrease in bandgap after irradiation with high energy ion beams. FTIR and Raman band intensity are also found to be decreased due to energy deposited cycloaddition reactions. While, using high mass ion beam ( $\text{Xe}^{5+}$ ), all structural features found to be vanished.



**Conclusion  
&  
Future Aspects**

## 6.1. Conclusions

The thesis summarizes the investigation carried out on the effect of ion beam irradiation (90 MeV Ni<sup>7+</sup>, 55 MeV Si<sup>4+</sup> and 1400 KeV Xe<sup>5+</sup> SHI) on the different properties of P3HT and PCBM thin films (thickness ~ 300 nm and 100 nm, respectively) prepared by spin coating on glass and double side polished silicon substrates. The following conclusions could be drawn from the study:

- ✚ Irradiation from both ion beams (90 MeV Ni<sup>7+</sup> and 55 MeV Si<sup>4+</sup>) resulted in the enhancement in the room temperature dc conductivity for the optimized fluence  $1 \times 10^{10}$  ions/cm<sup>2</sup> for 90 MeV Ni<sup>7+</sup> ions and  $1 \times 10^{11}$  ions/cm<sup>2</sup> for 55 MeV Si<sup>4+</sup> ions.
- ✚ The variation of dc conductivity in P3HT thin films with temperature is measured using two probe method and hopping of charge carriers between the polymer chains contributes more in conduction mechanism is observed in the present study. But in lower temperature region, the conductivity becomes independent with temperature and charge transport mechanism can be attributed to the tunneling between polymer chains.
- ✚ The changed/increased conductivity was due to the increased mobility of charge carriers, organization and delocalization length of  $\pi$  electron. The increased conductivity is ascribed to the better ordering of polymer chains by displacement of chains leading to the closely packed chains after irradiation with highly energetic ions.
- ✚ The increased ordering, crystallinity and conjugation length of P3HT favoring higher delocalization of electrons in polymer chains. Therefore, more delocalized  $\pi$  bands associated with better conductivity at low fluences which is further supported by FTIR studies, XRD studies, optical spectra and Raman spectra.
- ✚ The molecular ordering of P3HT at lower fluences and again disordering at higher fluence were also confirmed from the decreased FWHM and increased intensity ratio in Raman spectra. The optimized fluence where maximum enhancement in the intensity obtained, was  $1 \times 10^{10}$  ions/cm<sup>2</sup> for 90 MeV Ni<sup>7+</sup> ions and  $1 \times 10^{11}$  ions/cm<sup>2</sup> for 55 MeV Si<sup>4+</sup> ions. While, irradiation using 1400 KeV Xe<sup>5+</sup> ions producing damage from the initial fluence ( $1 \times 10^{12}$  ions/cm<sup>2</sup>).
- ✚ FTIR spectroscopy analysis confirms the enhanced intensity of IR active modes after irradiation along with the enhanced relative intensity ratio which is also confirms the

increased conjugation length for both (90 MeV Ni<sup>7+</sup> and 55 MeV Si<sup>4+</sup>) SHI irradiation within the optimized fluences.

- ✚ The increased crystallinity upto optimized ion fluences for both ion beams was obtained. The crystallite size was increased from 15.43 to 34.85 nm along the (100) peak of P3HT after the 90 MeV Ni<sup>7+</sup> ion irradiation. While, for the 55 MeV Si<sup>4+</sup> ion beam, crystallite size was found to increase from 12.41 to 13.02 nm. This enhancement is concluded to be due to the increased ordering of the alkyl chains within main thiophene chain. Also, the conjugation length within the crystallite is larger because of well orientation and less structural defects.
- ✚ XPS analysis of high resolution peaks (C and S) of P3HT confirms the  $\pi$ -conjugated system is not broken into smaller conjugation length and the nature of chemical bonding of thiophene units near the film surface is not much affected after irradiation from both ion beams upto optimized fluence.
- ✚ Slight enhancement in the absorption peak intensity and slight variation in the bandgap was obtained after irradiating P3HT thin films using both, 90 MeV Ni<sup>7+</sup> and 55 MeV Si<sup>4+</sup>, ion beams. The increased peak intensity of emission spectra and slight red shift also indicating change in the polymer conformation and increased conjugation length upto optimized fluence for both incident ion beam.
- ✚ The optical bandgap using absorption spectra of PCBM thin films were demonstrated to be tunable by using SHI irradiation. Bandgap was found to be decreased from 2.1 to 1.8 eV (at  $1 \times 10^{11}$  ions/cm<sup>2</sup>) when, PCBM films were irradiated by 90 MeV Ni<sup>7+</sup> and 55 MeV Si<sup>4+</sup> ions. This decrement in the bandgap is concluded to be due to the 2+2 cycloaddition polymerization reaction of PCBM molecules.
- ✚ The structural damage at higher fluences is also observed by FTIR and Raman studies. The measured surface RMS roughness was also increased after irradiation which might be favorable to increase the short circuit current density by increasing the contact area between top electrode and active layer.
- ✚ Irradiation of P3HT and PCBM thin films using high mass ion (Xe<sup>5+</sup>) with low energy (1400 KeV) is producing damages in the material. Therefore, optimized energy of incident ion, mass of the used ion species and incident ion fluences are most important parameters to get rid from large damage of material.

## **6.2. Future scope of this work**

- ✚ The modifications produced by high energy ions in the properties of P3HT-PCBM bilayer structure may be studied to investigate the device performance.
- ✚ The analysis of the effect of these energetic ions on blend structure of P3HT-PCBM may also be studied as blend will be used in device.
- ✚ The optimization of parameters and stability of films are also required to use this study in devices.
- ✚ A study including other conducting polymer such as PTB7, PCTDTBT etc. under SHI irradiation impact may also be studied.



## References:

- [1] J.M.G. Cowie, *Polymers: Chemistry and Physics of Modern Materials*, Nelson Thomes Ltd, 2002.
- [2] Chanda M., *Introduction to Polymer Science and Chemistry*, CRC Press, USA, 2006.
- [3] J.M.G. Cowie, *Polymers: Chemistry and Physics of Modern Materials*, third, Glasgow, 1991.
- [4] D. bloor Tony Blythe, *Electrical Properties of polymers*, Second, Cambridge university press, 2005.
- [5] F.W. Billmeyer, *Metrology, documentary standards, and color specifications for fluorescent materials*, *Color Res. Appl.* 19 (1994) 413–425. doi:10.1002/col.5080190602.
- [6] V.R. (Vasant R.. Gowariker, N. V. Viswanathan, J. Sreedhar, *Polymer science*, Wiley, 1986.
- [7] G.S. Misra, *Introductory polymer chemistry*, J. Wiley & Sons, 1993.
- [8] H. Shirakawa, E.J. Louis, A.G. MacDiarmid, C.K. Chiang, A.J. Heeger, *Synthesis of electrically conducting organic polymers: halogen derivatives of polyacetylene, (CH)<sub>x</sub>*, *J. Chem. Soc. Chem. Commun.* (1977) 578. doi:10.1039/c39770000578.
- [9] A.J. Heeger, Nobel Lecture: *Semiconducting and metallic polymers: The fourth generation of polymeric materials*, *Rev. Mod. Phys.* 73 (2001) 681–700. doi:10.1103/RevModPhys.73.681.
- [10] A.G. MacDiarmid, Nobel Lecture: “Synthetic metals”: A novel role for organic polymers, *Rev. Mod. Phys.* 73 (2001) 701–712. doi:10.1103/RevModPhys.73.701.
- [11] H. Shirakawa, Nobel Lecture: *The discovery of polyacetylene film—the dawning of an era of conducting polymers*, *Rev. Mod. Phys.* 73 (2001) 713–718. doi:10.1103/RevModPhys.73.713.
- [12] A.G. MacDiarmid, A.J. Epstein, *Polyanilines: a novel class of conducting polymers*, *Faraday Discuss. Chem. Soc.* 88 (1989) 317. doi:10.1039/dc9898800317.
- [13] J. Yue, Z.H. Wang, K.R. Cromack, A.J. Epstein, A.G. MacDiarmid, *Effect of sulfonic acid group on polyaniline backbone*, *J. Am. Chem. Soc.* 113 (1991) 2665–2671. doi:10.1021/ja00007a046.
- [14] L.H.C. Mattoso, S.K. Manohar, A.G. Macdiarmid, A.J. Epstein, *Studies on the chemical syntheses and on the characteristics of polyaniline derivatives*, *J. Polym. Sci. Part A Polym. Chem.* 33 (1995) 1227–1234. doi:10.1002/pola.1995.080330805.
- [15] B.L. Groenendaal, F. Jonas, D. Freitag, H. Pielartzik, J.R. Reynolds, *Poly(3,4-ethylenedioxythiophene) and Its Derivatives : Past , Present , and Future*, *Adv. Mater.* 12 (2000) 481–494. doi:10.1144/GSL.SP.2000.173.01.01.
- [16] A.J. Heeger, R. Pethig, *Charge Storage and Charge Transport in Conducting Polymers: Solitons, Polarons and*

- Bipolarons [and Discussion], *Philos. Trans. R. Soc. A Math. Phys. Eng. Sci.* 314 (1985) 17–35.  
doi:10.1098/rsta.1985.0005.
- [17] R.J. Waltman, J. Bargon, Electrically conducting polymers: a review of the electropolymerization reaction, of the effects of chemical structure on polymer film properties, and of applications towards technology, *Can. J. Chem.* 64 (1986) 76–95.
- [18] D.R. Tobergte, S. Curtis, Electrical Properties of Pyrrole and its copolymers, *Synth. Met.* 4 (1981) 119–130.  
doi:10.1017/CBO9781107415324.004.
- [19] A.O. Patil, A.J. Heeger, Optical properties of conducting polymers, *Chem. Rev.* 88 (1988) 183.  
doi:10.1021/cr00083a009.
- [20] K. Yoshino, S. Nakajima, M. Onoda, R. Sugimoto, Electrical and optical properties of poly(3-alkylthiophene), *Synth. Met.* 28 (1989) 349–357.  
doi:10.1016/0379-6779(89)90545-6.
- [21] K. Yoshino, K. Tada, K. Yoshimoto, M. Yoshida, T. Kawai, H. Araki, M. Hamaguchi, A. Zakhidov, Electrical and optical properties of molecularly doped conducting polymers, *Synth. Met.* 78 (1996) 301–312. doi:10.1016/0379-6779(96)80154-8.
- [22] R.H. Friend, R.W. Gymer, A.B. Holmes, J.H. Burroughes, R.N. Marks, C. Taliani, D.D.C. Bradley, D.A. Dos Santos, J.L. Bredas, M. Logdlund, W.R. Salaneck, Electroluminescence in conjugated polymers, *Nature.* 397 (1999) 121–128.  
doi:10.1038/16393.
- [23] G. Daoust, M. Leclerc, Structure-Property Relationships in Alkoxy-Substituted Polythiophenes, *Macromolecules.* 24 (1991) 455–459.  
doi:10.1021/ma00002a018.
- [24] M.L. and K. Faid, Electrical and Optical Properties of Processable Polythiophene Derivatives: Structure-Property Relationships, *Adv. Mater.* 9 (1997) 1087–1094. doi:10.1143/JPSJ.25.290.
- [25] M.J. Winokur, W. Chunwachirasiri, Nanoscale structure-property relationships in conjugated polymers: Implications for present and future device applications, *J. Polym. Sci. Part B Polym. Phys.* 41 (2003) 2630–2648.  
doi:10.1002/polb.10652.
- [26] D. Tyler McQuade, A.E. Pullen, T.M. Swager, Conjugated polymer-based chemical sensors, *Chem. Rev.* 100 (2000) 2537–2574.  
doi:10.1021/cr9801014.
- [27] X.S. Chang-qin Wu, Nonlinear optical susceptibilities of conducting polymers, *Phys. Rev. B.* 41 (1990) 12845–12849.
- [28] V. Saxena, B.D. Malhotra, Prospects of conducting polymers in molecular electronics, *Curr. Appl. Phys.* 3 (2003) 293–305. doi:10.1016/S1567-1739(02)00217-1.
- [29] R.J. Mortimer, A.L. Dyer, J.R. Reynolds, Electrochromic organic and polymeric materials for display applications, *Displays.* 27 (2006) 2–18.  
doi:10.1016/j.displa.2005.03.003.
- [30] E. Smela, E.W.H. Jager, O. Inganas,

- Microfabricating conjugated polymer actuators, *Science* (80-. ). 290 (2000) 1540–1545.  
doi:10.1126/science.290.5496.1540.
- [31] E. Smela, Conjugated Polymer Actuators for Biomedical Applications, *Adv. Mater.* 15 (2003) 481–494.  
doi:10.1002/adma.200390113.
- [32] H. Sirringhaus, P.J. Brown, R.H. Friend, M.M. Nielsen, K. Bechgaard, B.M.W. Langeveld-Voss, A.J.H. Spiering, R.A.J. Janssen, E.W. Meijer, P. Herwig, D.M. de Leeuw, Two-dimensional charge transport in self-organized, high-mobility conjugated polymers, *Nature*. 401 (1999) 685–688. doi:10.1038/44359.
- [33] Z. Bao, A. Dodabalapur, A.J. Lovinger, Soluble and processable regioregular poly(3-hexylthiophene) for thin film field-effect transistor applications with high mobility, *Appl. Phys. Lett.* 69 (1996) 4108–4110.  
doi:10.1063/1.117834.
- [34] F.C. Spano, Modeling disorder in polymer aggregates: The optical spectroscopy of regioregular poly(3-hexylthiophene) thin films, *J. Chem. Phys.* 122 (2005).  
doi:10.1063/1.1914768.
- [35] Y. Kim, S. Cook, S.M. Tuladhar, S.A. Choulis, J. Nelson, J.R. Durrant, D.D.C. Bradley, M. Giles, I. McCulloch, C.-S. Ha, M. Ree, A strong regioregularity effect in self-organizing conjugated polymer films and high-efficiency polythiophene:fullerene solar cells, *Nat. Mater.* 5 (2006) 197–203.  
doi:10.1038/nmat1574.
- [36] Y. Zhao, G. Yuan, P. Roche, M. Leclerc, A calorimetric study of the phase transitions in poly(3-hexylthiophene), *Polymer (Guildf)*. 36 (1995) 2211–2214.
- [37] J.C. Hummelen, B.W. Knight, F. Lepeq, F. Wudl, J. Yao, C.L. Wilkins, Preparation and Characterization of Fulleroid and Methanofullerene Derivatives, *J. Org. Chem.* 60 (1995) 532–538. doi:10.1021/jo00108a012.
- [38] S. Cho, S.H. Nho, M. Eo, M.H. Lee, Effects of processing additive on bipolar field-effect transistors based on blends of poly(3-hexylthiophene) and fullerene bearing long alkyl tails, *Org. Electron. Physics, Mater. Appl.* 15 (2014) 1002–1011. doi:10.1016/j.orgel.2014.02.003.
- [39] G. Yu, J. Gao, J.C. Hummelen, F. Wudl, A.J. Heeger, Polymer Photovoltaic Cells - Enhanced Efficiencies Via a Network of Internal Donor-Acceptor Heterojunctions, *Science* (80-. ). 270 (1995) 1789–1791.  
doi:10.1126/science.270.5243.1789.
- [40] A. Lefrançois, B. Luszczynska, B. Pepin-Donat, C. Lombard, B. Bouthinon, J.-M. Verilhac, M. Gromova, J. Faure-Vincent, S. Pouget, F. Chandezon, S. Sadki, P. Reiss, Enhanced Charge Separation in Ternary P3HT/PCBM/CuInS<sub>2</sub> Nanocrystals Hybrid Solar Cells, *Sci. Rep.* 5 (2015) 7768. doi:10.1038/srep07768.
- [41] A. Laiho, H.S. Majumdar, J.K. Baral, F. Jansson, R. Österbacka, O. Ikkala, Tuning the electrical switching of

- polymer/fullerene nanocomposite thin film devices by control of morphology, *Appl. Phys. Lett.* 93 (2008) 203309. doi:10.1063/1.3033221.
- [42] S.-K. Lin, L.-L. Shiu, K.-M. Chien, T.-Y. Luh, T.-I. Lin, Fluorescence of fullerene derivatives at room temperature, *J. Phys. Chem.* 99 (1995) 105–111. doi:10.1021/j100001a019.
- [43] M.T. Rispens, A. Meetsma, R. Rittberger, C.J. Brabec, N.S. Sariciftci, J.C. Hummelen, Influence of the solvent on the crystal structure of PCBM and the efficiency of MDMO-PPV:PCBM “plastic” solar cells., *Chem. Commun. (Camb.)*. (2003) 2116–8. doi:10.1039/b305988j.
- [44] F. Gajdos, H. Oberhofer, M. Dupuis, J. Blumberger, On the inapplicability of electron-hopping models for the organic semiconductor phenyl-C61-butyric acid methyl ester (PCBM), *J. Phys. Chem. Lett.* 4 (2013) 1012–1017. doi:10.1021/jz400227c.
- [45] D.L. Cheung, A. Troisi, Theoretical Study of the Organic Photovoltaic Electron Acceptor PCBM: Morphology, Electronic Structure, and Charge Localization †, *J. Phys. Chem. C*. 114 (2010) 20479–20488. doi:10.1021/jp1049167.
- [46] H.S. Nalwa, ed., *Molecular Electronics Devices in Encyclopedia of nanoscience and nanotechnology.*, American Scientific Publishers, USA, 2004.
- [47] G.B.S. J L Bredas, polarons, Bipolarons and Solitons in conducting polymers, (1985) 309–315.
- [48] H.A. Mizes, E.M. Conwell, Stability of polarons in conducting polymers, *Phys. Rev. Lett.* 70 (1993) 1505–1508. doi:10.1103/PhysRevLett.70.1505.
- [49] J.L. Bredas, Bipolarons in Doped Conjugated Polymers: A Critical Comparison Between Theoretical Results and Experimental Data, *Mol. Cryst. Liq. Cryst.* 118 (1985) 49–56. doi:10.1080/00268948508076188.
- [50] A.J. Heeger, S. Kivelson, J.R. Schrieffer, W.P. Su, Solitons in conducting polymers, *Rev. Mod. Phys.* 60 (1988) 781–850. doi:10.1103/RevModPhys.60.781.
- [51] E.H. Lee, Ion-beam modification of polymeric materials- fundamental principles and applications, *Nucl. Inst. Methods Phys. Res. B*. 151 (1999) 29–41.
- [52] S. Bouffard, E. Balanzat, C. Leroy, J.P. Busnel, G. Guevelou, Cross-links induced by swift heavy ion irradiation in polystyrene, *Nucl. Instruments Methods Phys. Res. Sect. B Beam Interact. with Mater. Atoms*. 131 (1997) 79–84. [http://dx.doi.org/10.1016/S0168-583X\(97\)00383-2](http://dx.doi.org/10.1016/S0168-583X(97)00383-2) %5Cnfile://c/Documents and Settings/powles/My Documents/Bibliography/PDFs/Bouffard\_1997.pdf.
- [53] T. Steckenreiter, E. Balanzat, H. Fuess, C. Trautmann, Chemical modifications of PET induced by swift heavy ions, *Nucl. Instruments Methods Phys. Res.*

- Sect. B Beam Interact. with Mater. Atoms. 131 (1997) 159–166.  
doi:10.1016/S0168-583X(97)00364-9.
- [54] J.V. D. Fink, R. Klett, Xuanwen Hu, M. Müller, G. Schiwietz, G. Xiao, L.T. Chadderton, L. Wang, C. Mathis, V. Hnatowicz, Characterization of aged latent ion tracks in polyimide, Nucl. Instrum. Methods B. 116 (1996) 66–71.
- [55] R.P. Torrisi, L., Ion beam processing of polyvinylidene fluoride, Nucl. Instrum. Methods B. 117 (1996) 387–391.  
doi:10.1016/S0026-0657(99)80568-2.
- [56] N. Betz, E. Petersohn, Swift heavy ions effects in fluoropolymers: radicals and crosslinking, NIMB. 116 (1996) 207–211.
- [57] E. Balanzat, N. Betz, S. Bouffard, Swift heavy ion modification of polymers, Nucl. Inst. Methods Phys. Res. B. 105 (1995) 46–54. doi:10.1016/0168-583X(95)00521-8.
- [58] J. Davenas, I. Stevenson, N. Celette, S. Cambon, J.L. Gardette, A. Rivaton, L. Vignoud, Stability of polymers under ionising radiation: The many faces of radiation interactions with polymers, Nucl. Instruments Methods Phys. Res. Sect. B Beam Interact. with Mater. Atoms. 191 (2002) 653–661.  
doi:10.1016/S0168-583X(02)00628-6.
- [59] E. Grossman, I. Gouzman, Space environment effects on polymers in low earth orbit, Nucl. Instruments Methods Phys. Res. Sect. B Beam Interact. with Mater. Atoms. 208 (2003) 48–57.  
doi:10.1016/S0168-583X(03)00640-2.
- [60] R.J. (Robert J. Woods, A.K. (Aleksēi K. Pikaev, Applied radiation chemistry : radiation processing, Wiley, 1994.
- [61] M. Toulemonde, C. Trautmann, E. Balanzat, K. Hjort, A. Weidinger, Track formation and fabrication of nanostructures with MeV-ion beams, Nucl. Instruments Methods Phys. Res. Sect. B Beam Interact. with Mater. Atoms. 216 (2004) 1–8.  
doi:10.1016/j.nimb.2003.11.013.
- [62] L.C. Feldman, J.W. Mayer, S.T. Picraux, Materials analysis by ion channeling : submicron crystallography, Academic Press, New York, 1982.  
<http://www.worldcat.org/title/materials-analysis-by-ion-channeling-submicron-crystallography/oclc/8476304> (accessed October 26, 2017).
- [63] J.F. Ziegler, M.D. Ziegler, J.P. Biersack, SRIM - The stopping and range of ions in matter (2010), Nucl. Instruments Methods Phys. Res. Sect. B Beam Interact. with Mater. Atoms. 268 (2010) 1818–1823.  
doi:10.1016/j.nimb.2010.02.091.
- [64] R.L. Fleischer, P.B. Price, R.M. Walker, Ion explosion spike mechanism for formation of charged-particle tracks in solids, J. Appl. Phys. 36 (1965) 3645–3652. doi:10.1063/1.1703059.
- [65] W.L.B. R.E. Johnson, Electronic mechanism for sputtering of condensed-gas solids by energetic ions, Nu. 198 (1982) 103–118.
- [66] A.I.R. and A.E. Volkov, Model of track formation Russian, Phys. Rev. B. 51

- (1995) 12107.  
doi:10.13246/j.cnki.iae.2014.05.016.
- [67] C. Dufour, Z.G. Wang, M. Levalois, P. Marie, E. Paumier, F. Pawlak, M. Toulemonde, Sensitivity of Metallic Materials under Irradiation with Swift Heavy Ions, *Nucl. Instrum. Methods B.* 107 (1996) 218–222. doi:10.1016/0168-583X(95)01030-0.
- [68] M. Toulemonde, S. Bouffard, F. Studer, Swift heavy ions in insulating and conducting oxides: tracks and physical properties, *Nucl. Inst. Methods Phys. Res. B.* 91 (1994) 108–123. doi:10.1016/0168-583X(94)96200-6.
- [69] A. Meftah, F. Brisard, J.M. Costantini, M. Hage-Ali, J.P. Stoquert, F. Studer, M. Toulemonde, Swift heavy ions in magnetic insulators: A damage-cross-section velocity effect, *Phys. Rev. B.* 48 (1993) 920–925. doi:10.1103/PhysRevB.48.920.
- [70] C. Trautmann, K. Schwartz, T. Steckenreiter, Specificity of ion induced damage, *Most.* 156 (1999) 162–169.
- [71] A. Chapiro, Chemical modifications in irradiated polymers, *Nucl. Instruments Methods Phys. Res. Sect. B Beam Interact. with Mater. Atoms.* 32 (1988) 111–114. doi:10.1016/0168-583X(88)90191-7.
- [72] D. Dudenko, A. Kiersnowski, J. Shu, W. Pisula, D. Sebastiani, H.W. Spiess, M.R. Hansen, A strategy for revealing the packing in semicrystalline ??-conjugated polymers: Crystal structure of bulk poly-3-hexyl-thiophene (P3HT), *Angew. Chemie - Int. Ed.* 51 (2012) 11068–11072. doi:10.1002/anie.201205075.
- [73] M.J. Winokur, D. Spiegel, Y. Kim, A.J. Heeger, S. Barbara, S. Barbara, STRUCTURAL AND ABSORPTION STUDIES OF THE THERMOCHROMIC TRANSITION IN, 28 (1989) 419–426.
- [74] G. Gustafsson, O. Inganäs, H. Österholm, J. Laakso, X-ray diffraction and infra-red spectroscopy studies of oriented poly (3-alkylthiophenes), *Polymer (Guildf).* 32 (1991) 1574. <http://www.sciencedirect.com/science/article/pii/0032386191903905>.
- [75] Z. Bao, A. Dodabalapur, A.J. Lovinger, Soluble and Processable Regioregular poly(3-hexylthiophene) for Thin Film Field-Effect Transistor Applications with High Mobility, *Appl. Phys. Lett.* 69 (1996) 4108. doi:10.1063/1.117834.
- [76] H. Sirringhaus, P.J. Brown, R.H. Friend, M.M. Nielsen, K. Bechgaard, A.J.H. Spiering, Two-dimensional charge transport in conjugated polymers, *Lett. to Nat.* 401 (1999) 685–688.
- [77] H. Sirringhaus, N. Tessler, R.H. Friend, Integrated Optoelectronic Devices Based on Conjugated Polymers, *Science (80-. )*. 280 (1998) 1741. doi:10.1126/science.280.5370.1741.
- [78] Y. Kim, S. Cook, S.M. Tuladhar, S.A. Choulis, J. Nelson, J.R. Durrant, D.D.C. Bradley, M. Giles, I. McCulloch, C.-S. Ha, M. Ree, A strong regioregularity effect in self-organizing conjugated polymer films and high-efficiency

- polythiophene:fullerene solar cells, *Nat. Mater.* 5 (2006) 197–203. doi:10.1038/nmat1574.
- [79] S.E. Shaheen, C.J. Brabec, N.S. Sariciftci, F. Padinger, T. Fromherz, J.C. Hummelen, 2.5% Efficient Organic Plastic Solar Cells, *Appl. Phys. Lett.* 78 (2001) 841–843. doi:10.1063/1.1345834.
- [80] J.Y. Kim, K. Lee, N.E. Coates, D. Moses, T. Nguyen, M. Dante, A.J. Heeger, Efficient Tandem Polymer Solar Cells Fabricated by All-Solution Processing, *Science* (80-. ). 317 (2007) 222–225. doi:10.1126/science.1141711.
- [81] T.D. Anthopoulos, D.M. De Leeuw, E. Cantatore, S. Setayesh, E.J. Meijer, C. Tanase, J.C. Hummelen, P.W.M. Blom, Organic complementary-like inverters employing methanofullerene-based ambipolar field-effect transistors, *Appl. Phys. Lett.* 85 (2004) 4205–4207. doi:10.1063/1.1812577.
- [82] A. Laiho, H.S. Majumdar, J.K. Baral, F. Jansson, R. Österbacka, O. Ikkala, Tuning the electrical switching of polymer/fullerene nanocomposite thin film devices by control of morphology, *Appl. Phys. Lett.* 93 (2008). doi:10.1063/1.3033221.
- [83] E.R. Hull, R.M. Osgood, J. Parisi, *Fundamentals of Ion-Irradiated Polymers*, n.d.
- [84] R. Singhal, D. Kabiraj, P.K. Kulriya, J.C. Pivin, R. Chandra, D.K. Avasthi, Blue-Shifted SPR of Au Nanoparticles with Ordering of Carbon by Dense Ionization and Thermal Treatment, *Plasmonics*. 8 (2013) 295–305. doi:10.1007/s11468-012-9389-6.
- [85] D.K. Avasthi, G.K. Mehta, *Swift heavy ions for materials engineering and nanostructuring*, Springer, 2011.
- [86] E. Herzig, P. Müller-Buschbaum, Organic photovoltaic cells for space applications, *Acta Futur.* 6 (2013) 17–24. doi:10.2420/AF06.2013.17.
- [87] A. Kimoto, H. Takaku, H. Hayakawa, M. Koseki, R. Ishihama, T. Aoyama, Y. Tajima, Multilayer organic photovoltaic devices fabricated by electrospray deposition technique and the role of the interlayer, *Thin Solid Films.* 636 (2017) 302–306. doi:10.1016/j.tsf.2017.06.026.
- [88] L. Sihver, Physics and biophysics experiments needed for improved risk assessment in space, *Acta Astronaut.* 63 (2008) 886–898. doi:10.1016/j.actaastro.2008.04.013.
- [89] M.M. Nasef, K.Z.M. Dahlan, Electron irradiation effects on partially fluorinated polymer films: Structure-property relationships, *Nucl. Instruments Methods Phys. Res. Sect. B Beam Interact. with Mater. Atoms.* 201 (2003) 604–614. doi:10.1016/S0168-583X(02)02068-2.
- [90] M. Guenther, G. Gerlach, G. Suchanek, K. Sahre, K.J. Eichhorn, V. Baturin, S. Duvanov, Physical properties and structure of thin ion-beam modified polymer films, *Nucl. Instruments Methods Phys. Res. Sect. B Beam Interact. with Mater. Atoms.* 216 (2004) 143–148. doi:10.1016/j.nimb.2003.11.070.

- [91] M. Mujahid, P. Singh, D.S. Srivastava, S. Gupta, D.K. Avasthi, D. Kanjilal, Study of chain scission versus crosslinking in MeV ion-irradiated polycarbonate using dielectric constant measurements and UV spectroscopy, *Radiat. Meas.* 38 (2004) 197–203. doi:10.1016/j.radmeas.2003.09.004.
- [92] V.K. Mittal, S. Lotha, D.K. Avasthi, Hydrogen loss under heavy ion irradiation in polymers, 0150 (2016). doi:10.1080/10420159908229009.
- [93] L. Calcagno, Structural modification of polymer films by ion irradiation The, *Nucl. Inst. Methods Phys. Res. B.* 65 (1992) 413–422.
- [94] L. Calcagno, Ion irradiation of polymers, *Nucl. Inst. Methods Phys. Res. B.* 59/60 (1991) 1153–1158.
- [95] S.K. Park, S.Y. Lee, C.S. Lee, H.M. Kim, J. Joo, Y.W. Beag, S.K. Koh, S.K. Park, S.Y. Lee, C.S. Lee, H.M. Kim, J. Joo, High energy ( MeV ) ion-irradiated  $\pi$ -conjugated polyaniline : Transition from insulating state to carbonized conducting state, *J. Appl. Phys.* 96 (2004) 1914–1918. doi:10.1063/1.1769603.
- [96] H. Search, C. Journals, A. Contact, M. Iopscience, I.P. Address, Formation of Nanowires Based on  $\pi$ -Conjugated Polymers by High-Energy Ion Beam Irradiation Formation of Nanowires Based on  $\pi$ -Conjugated Polymers by High-Energy Ion Beam Irradiation, 5839 (n.d.) 23–27. doi:10.1143/JJAP.44.5839.
- [97] A. Kaur, A. Dhillon, D.K. Avasthi, Effect of 100 MeV swift heavy ions [silver(Ag 8+) on morphological and electrical properties of polypyrrole, *J. Appl. Phys.* 106 (2009) 073715. doi:10.1063/1.3233915.
- [98] R.C. Ramola, A. Alqudami, S. Chandra, S. Annapoorni, J.M.S. Rana, R.G. Sonkawade, F. Singh, D.K. Avasthi, Effects of swift heavy ions irradiation on polypyrrole thin films, *Radiat. Eff. Defects Solids.* 163 (2008) 151–159. doi:10.1080/10420150701639985.
- [99] M.Z. G. B. V. S. Lakshmi, Azher M. Siddiqui, Effects of Si 5+ Ion Irradiation on Poly ( 3-methyl thiophene ) Films, *Int. J. Polym. Mater.* 59 (2010) 970–980. doi:10.1080/00914037.2010.504142.
- [100] M.Z. G.B.V.S. Lakshmi, Azher M. Siddiquia, Structural, optical and electrical properties of 60MeV C5+ ion-irradiated poly(3-methylthiophene) films, *Radiat. Eff. Defects Solids.* 166 (2011) 427–434. doi:10.1080/10420150.2011.553234.
- [101] J. Kumar, R.K. Singh, S. Chand, V. Kumar, R.C. Rastogi, R. Singh, Dc Electrical Conduction and Morphology of Poly(3-Octylthiophene) Films, *J. Phys. D. Appl. Phys.* 39 (2006) 196–202. doi:10.1088/0022-3727/39/1/029.
- [102] A. Srivastava, T. V. Singh, S. Mule, C.R. Rajan, S. Ponrathnam, Study of chemical, optical and thermal modifications induced by 100 MeV silicon ions in a polycarbonate film, *Nucl. Instruments Methods Phys. Res. Sect. B Beam Interact. with Mater.*



- Atoms. 192 (2002) 402–406.  
doi:10.1016/S0168-583X(02)00493-7.
- [103] S. Seki, A. Saeki, W. Choi, Y. Maeyoshi, M. Omichi, A. Asano, K. Enomoto, C. Vijayakumar, M. Sugimoto, S. Tsukuda, S.I. Tanaka, Semiconducting cross-linked polymer nanowires prepared by high-energy single-particle track reactions, *J. Phys. Chem. B.* 116 (2012) 12857–12863. doi:10.1021/jp3069249.
- [104] N. Bajwa, A. Ingale, D.K. Avasthi, R. Kumar, A. Tripathi, K. Dharamvir, V.K. Jindal, Role of electron energy loss in modification of C60 thin films by swift heavy ions, *J. Appl. Phys.* 104 (2008). doi:10.1063/1.2968340.
- [105] R. Singhal, A. Kumar, Y.K. Mishra, S. Mohapatra, J.C. Pivin, D.K. Avasthi, Swift heavy ion induced modifications of fullerene C70 thin films, *Nucl. Instruments Methods Phys. Res. Sect. B Beam Interact. with Mater. Atoms.* 266 (2008) 3257–3262. doi:10.1016/j.nimb.2008.04.003.
- [106] A. Kumar, D.K. Avasthi, J.C. Pivin, P.M. Koinkar, Ordering of fullerene and carbon nanotube thin films under energetic ion impact, *Appl. Phys. Lett.* 92 (2008). doi:10.1063/1.2938718.
- [107] R. Singhal, F. Singh, A. Tripathi, D.K. Avasthi, A comparative study of ion-induced damages in in C60 and C70 fullerenes, *Radiat. Eff. Defects Solids.* 164 (2009) 38–48. doi:10.1080/10420150802479638.
- [108] R. Singhal, J.C. Pivin, D.K. Avasthi, Ion beam irradiation-induced tuning of SPR of Au nanoparticles in fullerene C70 matrix: Dependence of energy loss, *J. Nanoparticle Res.* 15 (2013). doi:10.1007/s11051-013-1641-2.
- [109] Y. Maeyoshi, A. Saeki, S. Suwa, M. Omichi, H. Marui, A. Asano, S. Tsukuda, M. Sugimoto, A. Kishimura, K. Kataoka, S. Seki, Fullerene nanowires as a versatile platform for organic electronics, *Sci. Rep.* 2 (2012) 1–6. doi:10.1038/srep00600.
- [110] S. Suwa, Y. Maeyoshi, S. Tsukuda, M. Sugimoto, A. Saeki, S. Seki, Fullerene Nanowires Produced by Single Particle Nanofabrication Technique and Their Photovoltaic Applications, *J. Photopolym. Sci. Technol.* 26 (2013) 193–197. doi:10.2494/photopolymer.26.193.
- [111] P. Zhou, Z.H. Dong, A.M. Rao, P.C. Eklund, Reaction mechanism for the photopolymerization of solid fullerene C60, *Chem. Phys. Lett.* 211 (1993) 337–340. doi:10.1016/0009-2614(93)87069-F.
- [112] T.S. Y. Iwasa, T. Arima, R. M. Fleming, New Phases of C60 Synthesized at High Pressure, *Science* (80-. ). 264 (1994) 1570.
- [113] a. M. Rao, P. Zhou, K. a Wang, G.T. Hager, J.M. Holden, Y. Wang, W.T. Lee, X.X. Bi, P.C. Eklund, D.S. Cornett, M. a Duncan, I.J. Amster, Photoinduced polymerization of solid C\_60 films, *Science* (80-. ). 259 (1993) 955–957. doi:10.1126/science.259.5097.955.
- [114] A. Dhillon, A. Kaur, D.K. Avasthi,

- Electrical and morphological properties of poly ( 3-hexyl thiophene ) irradiated with 100 MeV silver ions, *Thin Solid Films*. 519 (2010) 998–1002.  
doi:10.1016/j.tsf.2010.08.030.
- [115] A. Kaur, A. Dhillon, G.B.V.S. Lakshmi, Y. Mishra, D.K. Avasthi, Modifications induced in poly (3-hexylthiophene) due to swift heavy ion beam of 100MeV silver (Ag<sup>8+</sup>), *Mater. Chem. Phys.* 131 (2011) 436–442.  
doi:10.1016/j.matchemphys.2011.10.001
- [116] P. Singh, S. Kumar, R. Prasad, R. Kumar, Study of physical and chemical modifications induced by 50MeV Li<sup>3+</sup> ion beam in polymers, *Radiat. Phys. Chem.* 94 (2014) 54–57.  
doi:10.1016/j.radphyschem.2013.07.008.
- [117] T. Sasuga, H. Kudoh, T. Seguchi, High energy ion irradiation effects on polymer materials – Changes in mechanical properties of PE , PSF and PES, *Polymer (Guildf)*. 40 (1999) 5095–5102.  
doi:10.1016/S0032-3861(98)00725-3.
- [118] P. Singh, R. Kumar, H.S. Virk, R. Prasad, Modification of optical , chemical and structural response of polymethyl methacrylate polymer by 70 MeV carbon ion irradiation, *Indian J. Pure Appl. Phys.* 48 (2010) 321–325.
- [119] H.D. and W.H. Yifan Yao, Ordering of conjugated polymer molecules: recent advances and perspectives, *Polym. Chem.* (2013). doi:10.1039/c3py00131h.
- [120] R. Mikšová, A. Macková, P. Malinský, P. Slepíčka, V. Švorčík, A study of the degradation of polymers irradiated by C<sup>n+</sup> and O<sup>n+</sup> 9.6 MeV heavy ions, *Polym. Degrad. Stab.* 122 (2015) 110–121.  
doi:10.1016/j.polymdegradstab.2015.10.017.
- [121] A.K. Himanshu, S.K. Bandyopadhyay, P. Sen, T.P. Sinha, Electric modulus studies of low energy Ar<sup>9+</sup> irradiated conducting polymer PANI-PVA, *Radiat. Phys. Chem.* 80 (2011) 414–419.  
doi:10.1063/1.3605810.
- [122] S. Tsukuda, S. Seki, S. Tagawa, M. Sugimoto, A. Idesaki, S. Tanaka, A. Oshima, Fabrication of Nanowires Using High-Energy Ion Beams, *J. Phys. Chem. B*. 108 (2004) 3407–3409.  
doi:10.1021/jp037638s.
- [123] A. Maillard, A. Rochefort, Structural and electronic properties of poly(3-hexylthiophene)  $\pi$ -stacked crystals, *Phys. Rev. B - Condens. Matter Mater. Phys.* 79 (2009) 1–7.  
doi:10.1103/PhysRevB.79.115207.
- [124] D.T. Duong, M.F. Toney, A. Salleo, Role of confinement and aggregation in charge transport in semicrystalline polythiophene thin films, *Phys. Rev. B - Condens. Matter Mater. Phys.* 86 (2012) 1–5. doi:10.1103/PhysRevB.86.205205.
- [125] X. Qian, P. Umari, N. Marzari, First-principles investigation of organic photovoltaic materials  $C_{60}$

- <mo> </mo> <mrow> <mo>[</mo>  
<msub> <mtext>C</mtext>  
<mn>60</m>, Phys. Rev. B. 91 (2015)  
245105.  
doi:10.1103/PhysRevB.91.245105.
- [126] L. Tskipuri, Q. Shao, J. Reutt-Robey,  
Molecular ordering in PCBM-Au(111)  
interface formation, J. Phys. Chem. C.  
116 (2012) 21874–21879.  
doi:10.1021/jp307201k.
- [127] N.D. Treat, T.E. Mates, C.J. Hawker,  
E.J. Kramer, M.L. Chabinyc,  
Temperature Dependence of the Di ff  
usion Coe ffi cient of PCBM in Poly(3-  
hexylthiophene), Macromolecules. 46  
(2013) 1002–1007.
- [128] A.S. Anselmo, A. Dzwilewski, K.  
Svensson, E. Moons, Photodegradation  
of the electronic structure of PCBM and  
C60 films in air, Chem. Phys. Lett. 652  
(2016) 220–224.  
doi:10.1016/j.cplett.2016.04.003.
- [129] D.K. Avasthi, W. Assmann, SPECIAL  
SECTION : ERDA with swift heavy ions  
for materials characterization, 80 (2001).
- [130] D. Kanjilal, S. Chopra, M.M. Narayanan,  
I.S. Iyer, V. Jha, R. Joshi, S.K. Datta,  
Testing and operation of the 15UD  
Pelletron at NSC, Nucl. Inst. Methods  
Phys. Res. A. 328 (1993) 97–100.  
doi:10.1016/0168-9002(93)90610-T.
- [131] P. Kumar, G. Rodrigues, U.K. Rao, C.P.  
Safvan, D. Kanjilal, a Roy, ECR ion  
source based low energy ion beam  
facility, Pramana. 59 (2002) 805–809.  
doi:10.1007/s12043-002-0094-4.
- [132] B.D. Cullity, Elements of X-ray  
diffraction, second, Addison-Wesley  
publishing company, 1978.
- [133] S. (Severin) Amelinckx, R. Gevers, J.  
van. Landuyt, B. International Summer  
Course on Material Science (1969 :  
Antwerp, Diffraction and imaging  
techniques in material science Volume  
II, Imaging and diffraction techniques,  
North-Holland Pub. Co., 1978.
- [134] A.L. Patterson, The scherrer formula for  
X-ray particle size determination, Phys.  
Rev. 56 (1939) 978–982.  
doi:10.1103/PhysRev.56.978.
- [135] J.D.J. Ingle, S.R. Crouch,  
Spectrochemical analysis, NJ (US);  
Prentice Hall College Book Division,  
1988.  
[https://www.osti.gov/biblio/5298199-  
spectrochemical-analysis](https://www.osti.gov/biblio/5298199-spectrochemical-analysis).
- [136] A.V. J. TAUC, R. GRIGOROVICI,  
Optical Properties and Electronic  
Structure of Amorphous Germanium,  
Phys. Status Solidi. 15 (1966) 627–637.  
doi:10.1002/pssb.19660150224.
- [137] C. V. RAMAN, K.S. KRISHNAN, A  
New Type of Secondary Radiation,  
Nature. 121 (1928) 501–502.  
doi:10.1038/121501c0.
- [138] Z.M. Zhang, SURFACE  
TEMPERATURE MEASUREMENT  
USING OPTICAL TECHNIQUES,  
Annu. Rev. Heat Transf. 11 (2000) 351–  
411.  
doi:10.1615/AnnualRevHeatTransfer.v1  
1.80.
- [139] D.J. O’Connor, B.A. Sexton, R.S.C.  
Smart, Surface Analysis Methods in

- Materials Science, Springer Berlin Heidelberg, 1992.
- [140] K. Kalantar-zadeh, B. Nicholas, Nanotechnology-Enabled Sensors, Springer, 2008.  
<http://www.wileyschmidt.com/nanotechnology-enabled-sensors.pdf> (accessed October 27, 2017).
- [141] A. Marmur, Equilibrium and spreading of liquids on solid surfaces, *Adv. Colloid Interface Sci.* 19 (1983) 75–102.  
 doi:10.1016/0001-8686(83)80004-9.
- [142] U.B. Singh, R.P. Yadav, R.K. Pandey, D.C. Agarwal, C. Pannu, A.K. Mittal, Insight Mechanisms of Surface Structuring and Wettability of Ion-Treated Ag Thin Films, *J. Phys. Chem. C.* 120 (2016) 5755–5763.  
 doi:10.1021/acs.jpcc.5b11944.
- [143] U.B. Singh, D.C. Agarwal, S.A. Khan, M. Kumar, A. Tripathi, R. Singhal, B.K. Panigrahi, D.K. Avasthi, Engineering of hydrophilic and plasmonic properties of Ag thin film by atom beam irradiation, *Appl. Surf. Sci.* 258 (2011) 1464–1469.  
 doi:10.1016/j.apsusc.2011.09.105.
- [144] T. Yamamoto, D. Komarudin, M. Arai, B.L. Lee, H. Suganuma, N. Asakawa, Y. Inoue, K. Kubota, S. Sasaki, T. Fukuda, H. Matsuda, Extensive studies on  $\pi$ -stacking of poly(3-alkylthiophene-2,5-diyl)s and poly(4-alkylthiazole-2,5-diyl)s by optical spectroscopy, NMR analysis, light scattering analysis, and X-ray crystallography, *J. Am. Chem. Soc.* 120 (1998) 2047–2058.  
 doi:10.1021/ja973873a.
- [145] P. Brown, D. Thomas, A. Köhler, J. Wilson, J.-S. Kim, C. Ramsdale, H. Sirringhaus, R. Friend, Effect of interchain interactions on the absorption and emission of poly(3-hexylthiophene), *Phys. Rev. B.* 67 (2003) 1–16.  
 doi:10.1103/PhysRevB.67.064203.
- [146] S.S. Pandey, W. Takashima, S. Nagamatsu, T. Endo, M. Rikukawa, K. Kaneto, Regioregularity vs regiorandomness: Effect on photocarrier transport in poly(3-hexylthiophene), *Japanese J. Appl. Physics, Part 2 Lett.* 39 (2000) 2–6. doi:10.1143/JJAP.39.L94.
- [147] R. Singhal, J.C. Pivin, R. Chandra, D.K. Avasthi, Ion irradiation studies of silver/amorphous carbon nanocomposite thin film, *Surf. Coatings Technol.* 229 (2013) 50–54.  
 doi:10.1016/j.surfcoat.2012.05.131.
- [148] A. Kumar, D.K. Avasthi, J.C. Pivin, A. Tripathi, F. Singh, Ferromagnetism induced by heavy-ion irradiation in fullerene films, *Phys. Rev. B - Condens. Matter Mater. Phys.* 74 (2006) 2–5.  
 doi:10.1103/PhysRevB.74.153409.
- [149] M. Baibarac, M. Lapkowski, A. Pron, S. Lefrant, I. Baltog, SERS Spectra of Poly (3-Hexylthiophene) in Oxidized and Unoxidized States, 29 (1998) 825–832.
- [150] A.M. Ballantyne, T.A.M. Ferenczi, M. Campoy-Quiles, T.M. Clarke, A. Maurano, K.H. Wong, W. Zhang, N. Stingelin-Stutzmann, J.-S. Kim, D.D.C. Bradley, J.R. Durrant, I. McCulloch, M. Heeney, J. Nelson, S. Tierney, W. Duffy, C. Mueller, P. Smith, Understanding the

- Influence of Morphology on Poly(3-hexylselenothiophene):PCBM Solar Cells, *Macromolecules*. 43 (2010) 1169–1174. doi:10.1021/ma902477h.
- [151] Y. Yacoby, E. Ehrenfreund, in: M. Cardona, G. Gfintnerodt (Eds.), *Light Scattering in Solids VI*, vol. 68, Springer, Berlin/Heidelberg, 1991, p. 73. - Google Search, (n.d.).
- [152] Y. Gao, J.K. Grey, Resonance Chemical Imaging of Polythiophene / Fullerene Photovoltaic Thin Films : Mapping Morphology-Dependent Aggregated and Unaggregated C d C Species, *J. Am. Chem. Soc.* 131 (2009) 9654–9662.
- [153] W.C. Tsoi, D.T. James, J.S. Kim, P.G. Nicholson, C.E. Murphy, D.D.C. Bradley, J. Nelson, J.S. Kim, The nature of in-plane skeleton Raman modes of P3HT and their correlation to the degree of molecular order in P3HT:PCBM blend thin films, *J. Am. Chem. Soc.* 133 (2011) 9834–9843. doi:10.1021/ja2013104.
- [154] S.K. Srivastava, D.K. Avasthi, W. Assmann, Z.G. Wang, H. Kucal, E. Jacquet, H.D. Carstanjen, M. Toulemonde, Test of the hypothesis of transient molten state diffusion for swift-heavy-ion induced mixing, *Phys. Rev. B - Condens. Matter Mater. Phys.* 71 (2005) 1–4. doi:10.1103/PhysRevB.71.193405.
- [155] A. Kumar, D.K. Avasthi, A. Tripathi, D. Kabiraj, F. Singh, J.C. Pivin, Synthesis of confined electrically conducting carbon nanowires by heavy ion irradiation of fullerene thin film, *J. Appl. Phys.* 101 (2007). doi:10.1063/1.2404794.
- [156] Z.G. Wang, C. Dufour, E. Paumier, M. Toulemonde, The Se sensitivity of metals under swift-heavy-ion irradiation: a transient thermal process, *J. Phys. Condens. Matter*. 6 (1994) 6733–6750. doi:10.1088/0953-8984/6/34/006.
- [157] M. Toulemonde, M. Toulemonde, W. Assmann, C. Trautmann, F. Gr??ner, Jetlike component in sputtering of LiF induced by swift heavy ions, *Phys. Rev. Lett.* 88 (2002) 576021–576024. doi:10.1103/PhysRevLett.88.057602.
- [158] A. Biswas, R. Gupta, N. Kumar, D.K. Avasthi, J.P. Singh, S. Lotha, D. Fink, S.N. Paul, S.K. Bose, A. Biswas, R. Gupta, N. Kumar, Recrystallization in polyvinylidene fluoride upon low fluence swift heavy ion impact Recrystallization in polyvinylidene fluoride upon low fluence swift heavy ion impact, *Appl. Phys. Lett.* 78 (2001) 4136–4138. doi:10.1063/1.1376664.
- [159] T.J. Prosa, M.J. Winokur, J. Moulton, P. Smith, a. J. Heeger, X-ray Structural Studies of Poly(3-alkylthiophenes): An Example of An Inverse Comb, *Macromolecules*. 25 (1992) 4364–4372. doi:10.1021/ma00043a019.
- [160] T. Erb, S. Raleva, U. Zhokhavets, G. Gobsch, B. Stühn, M. Spode, O. Ambacher, Structural and optical properties of both pure poly(3-octylthiophene) (P3OT) and P3OT/fullerene films, *Thin Solid Films*.

- 450 (2004) 97–100.  
doi:10.1016/j.tsf.2003.10.045.
- [161] D.E. Motaung, G.F. Malgas, C.J. Arendse, S.E. Mavundla, C.J. Oliphant, D. Knoesen, Thermal-induced changes on the properties of spin-coated P3HT:C60 thin films for solar cell applications, *Sol. Energy Mater. Sol. Cells*. 93 (2009) 1674–1680.  
doi:10.1016/j.solmat.2009.05.016.
- [162] R.J. Kline, M.D. McGehee, E.N. Kadnikova, J. Liu, J.M.J. Fréchet, M.F. Toney, M.J. Jean, The Dependence of Regioregular Poly ( 3- hexylthiophene ) Film Morphology and Field-Effect Mobility on Molecular Weight, *Macromolecules*. 38 (2004) 3312–3319.  
doi:10.1021/ma047415f.
- [163] A. Zen, J. Pflaum, S. Hirschmann, W. Zhuang, F. Jaiser, U. Asawapirom, J.P. Rabe, U. Scherf, D. Neher, Effect of molecular weight and annealing of poly(3-hexylthiophene)s on the performance of organic field-effect transistors, *Adv. Funct. Mater.* 14 (2004) 757–764. doi:10.1002/adfm.200400017.
- [164] U. Zhokhavets, T. Erb, H. Hoppe, G. Gobsch, N. Serdar Sariciftci, Effect of annealing of poly(3-hexylthiophene)/fullerene bulk heterojunction composites on structural and optical properties, *Thin Solid Films*. 496 (2006) 679–682.  
doi:10.1016/j.tsf.2005.09.093.
- [165] E.R. Hull, R.M. Osgood, J. Parisi, H. Warlimont, Springer Series in Springer Series in MATERIALS SCIENCE, 2008.
- [166] L. Scudiero, Y. Shen, M.C. Gupta, Effect of light illumination and temperature on P3HT films, n-type Si, and ITO, *Appl. Surf. Sci.* 292 (2014) 100–106.  
doi:10.1016/j.apsusc.2013.11.085.
- [167] M. Manceau, J. Gaume, A. Rivaton, J.L. Gardette, G. Monier, L. Bideux, Further insights into the photodegradation of poly(3-hexylthiophene) by means of X-ray photoelectron spectroscopy, *Thin Solid Films*. 518 (2010) 7113–7118.  
doi:10.1016/j.tsf.2010.06.042.
- [168] W.R. Salaneck, O. Inganäs, B. Thémans, J.O. Nilsson, B. Sjögren, J.E. Österholm, J.L. Brédas, Thermochromism in poly ( 3hexylthiophene ) in the solid state : A spectroscopic study of temperaturedependent conformational defects, 4613 (1988).  
doi:10.1063/1.454802.
- [169] F. Reisdorffer, O. Haas, P. Le Rendu, T.P. Nguyen, Co-solvent effects on the morphology of P3HT:PCBM thin films, *Synth. Met.* 161 (2012) 2544–2548.  
doi:10.1016/j.synthmet.2011.08.005.
- [170] J. Clark, C. Silva, R.H. Friend, F.C. Spano, Role of intermolecular coupling in the photophysics of disordered organic semiconductors: Aggregate emission in regioregular polythiophene, *Phys. Rev. Lett.* 98 (2007) 1–4.  
doi:10.1103/PhysRevLett.98.206406.
- [171] D.E. Motaung, G.F. Malgas, C.J. Arendse, Comparative study : The effects of solvent on the morphology , optical and structural features of

- regioregular poly ( 3-hexylthiophene ) : fullerene thin films, *Synth. Met.* 160 (2010) 876–882.  
doi:10.1016/j.synthmet.2010.01.038.
- [172] F.C. Spano, J. Clark, C. Silva, R.H. Friend, Determining exciton coherence from the photoluminescence spectral line shape in poly(3-hexylthiophene) thin films, *J. Chem. Phys.* 130 (2009).  
doi:10.1063/1.3076079.
- [173] N.F. (Nevill F. Mott, E.A. (Edward A. Davis, *Electronic processes in non-crystalline materials*, Clarendon Press, 1979.
- [174] R.K. Singh, J. Kumar, R. Singh, R. Kant, R.C. Rastogi, S. Chand, V. Kumar, Structure-conductivity correlation in ferric chloride-doped poly(3-hexylthiophene), *New J. Phys.* 8 (2006).  
doi:10.1088/1367-2630/8/7/112.
- [175] R. Singh, J. Kumar, A. Kaur, K.L. Yadav, R. Bhattacharyya, E. Hussain, S. Ali, Mechanism of dc electrical conduction and human endothelial cell proliferation in polypyrrole/sodium nitrate membrane, *Polymer (Guildf)*. 47 (2006) 6042–6047.  
doi:10.1016/j.polymer.2006.06.057.
- [176] M. Sawamoto, M. Kamigaito, T. Higashimura, Temperature dependent electrical conductivity of p-doped poly(3,4-ethylenedioxythiophene) and poly(3-alkylthiophene)s, *Polym. Bull.* 412 (1988) 407–412.
- [177] X. Jiang, R. Patil, Y. Harima, J. Ohshita, A. Kunai, Influences of self-assembled structure on mobilities of charge carriers in  $\pi$ -conjugated polymers, *J. Phys. Chem. B.* 109 (2005) 221–229.  
doi:10.1021/jp0460994.
- [178] S. Ukai, H. Ito, K. Marumoto, S.I. Kuroda, Electrical conduction of regioregular and regiorandom poly(3-hexylthiophene) doped with iodine, *J. Phys. Soc. Japan.* 74 (2005) 3314–3319.  
doi:10.1143/JPSJ.74.3314.
- [179] R. Singh, A.K. Narula, Correlation between electron spin resonance and dc conductivity data of polypyrrole , poly ( N -methyl pyrrole-pyrrole ), and poly ( N -methyl pyrrole ) Correlation between electron spin resonance and dc conductivity data of polypyrrole , poly ( N -methyl, 82 (9) (1997) 4362–4371.  
doi:10.1063/1.366246.
- [180] A.B. Kaiser, Electronic transport properties of conducting polymers and carbon nanotubes, 64 (2001) 1–49.
- [181] D.K. Paul, S.S. Mitra, Evaluation of Mott's parameters for hopping conduction in amorphous Ge, Si, and Se-Si, *Phys. Rev. Lett.* 31 (1973) 1000–1003. doi:10.1103/PhysRevLett.31.1000.
- [182] H.S. Nalwa, *Handbook of organic conductive molecules and polymers*. Vol. 3, Wiley, 1997.
- [183] F. Zuo, M. Angelopoulos, A.G. MacDiarmid, A.J. Epstein, ac conductivity of emeraldine polymer, *Phys. Rev. B.* 39 (1989) 3570–3578.  
doi:10.1103/PhysRevB.39.3570.
- [184] A.K. Meikap, A. Das, S. Chatterjee, M. Digar, S.N. Bhattacharyya, Electrical transport in doped polypyrrole films at

- low temperature, *Phys. Rev. B.* 47 (1993) 1340–1345.  
doi:10.1103/PhysRevB.47.1340.
- [185] P. a Lane, X. Wei, Z. V Vardeny, Studies of charged excitations in pi-conjugated oligomers and polymers by optical modulation, *Phys. Rev. Lett.* 77 (1996) 1544–1547.  
doi:10.1103/PhysRevLett.77.1544.
- [186] Y. Furukawa, M. Akimoto, I. Harada, VIBRATIONAL KEY BANDS AND ELECTRICAL CONDUCTIVITY OF POLYTHIOPHENE Y., 18 (1987) 151–156.
- [187] T. Sharma, R. Singhal, R. Vishnoi, G.B.V.S. Lakshmi, S. Chand, D.K. Avasthi, A. Kanjilal, S.K. Biswas, Ion irradiation induced modifications of P3HT : A donor material for organic photovoltaic devices, *Vacuum.* 135 (2017) 73–85.  
doi:10.1016/j.vacuum.2016.10.027.
- [188] W. Fischer, Raman excitation profiles of conjugated segments in solution *Institut,* 51 (1995) 8107–8114.
- [189] R.K. Singh, J. Kumar, R. Singh, R. Kant, S. Chand, V. Kumar, Micromorphology , photophysical and electrical properties of pristine and ferric chloride doped poly ( 3-hexylthiophene ) films, 104 (2007) 390–396.  
doi:10.1016/j.matchemphys.2007.01.024
- [190] M. Trznadel, a Pron, M. Zagorska, R. Chrzaszcz, J. Pielichowski, Effect of Molecular Weight on Spectroscopic and Spectroelectrochemical Properties of Regioregular Poly(3-hexylthiophene), *Macromolecules.* 31 (1998) 5051–5058.  
doi:10.1021/ma970627a.
- [191] M.J. Winokur, D. Spiegel, Y. Kim, S. Hotta, A.J. Heeger, Structural and absorption studies of the thermochromic transition in poly(3-hexylthiophene), *Synth. Met.* 28 (1989) 419–426.  
doi:10.1016/0379-6779(89)90554-7.
- [192] P. Vanlaeke, a. Swinnen, I. Haeldermans, G. Vanhoyland, T. Aernouts, D. Cheyns, C. Deibel, J. D’Haen, P. Heremans, J. Poortmans, J. V. Manca, P3HT/PCBM bulk heterojunction solar cells: Relation between morphology and electro-optical characteristics, *Sol. Energy Mater. Sol. Cells.* 90 (2006) 2150–2158.  
doi:10.1016/j.solmat.2006.02.010.
- [193] B.T. Erb, U. Zhokhavets, G. Gobsch, S. Raleva, B. Stühn, P. Schilinsky, C. Waldauf, C.J. Brabec, Correlation Between Structural and Optical Properties of Composite Polymer / Fullerene Films for Organic Solar Cells \*\*, (2005) 1193–1196.  
doi:10.1002/adfm.200400521.
- [194] T. Erb, U. Zhokhavets, H. Hoppe, G. Gobsch, M. Al-ibrahim, O. Ambacher, Absorption and crystallinity of poly ( 3-hexylthiophene )/ fullerene blends in dependence on annealing temperature, 512 (2006) 483–485.  
doi:10.1016/j.tsf.2005.12.064.
- [195] D. Lee, D. Jang, Charge-carrier relaxation dynamics of poly ( 3-hexylthiophene ) -coated gold hybrid



- nanoparticles, *Polymer (Guildf)*. 55 (2014) 5469–5476.  
doi:10.1016/j.polymer.2014.08.069.
- [196] J.U. Lee, J.W. Jung, T. Emrick, T.P. Russell, W.H. Jo, Morphology control of a polythiophene – fullerene bulk heterojunction for enhancement of the high-temperature stability of solar cell performance by a new donor – acceptor diblock copolymer, 105201 (n.d.).  
doi:10.1088/0957-4484/21/10/105201.
- [197] Warren B.E., B.E. Warren, *X-ray Diffraction*, Dover, New York,... - Google Scholar, new york, 1990.
- [198] A.M.P. Hussain, Study of 160 MeV Ni<sup>12+</sup> ion irradiation effects on electrodeposited polypyrrole films, 240 (2005) 871–880.  
doi:10.1016/j.nimb.2005.06.211.
- [199] X.M. Jiang, R. Osterbacka, O. Korovyanko, C.P. An, B. Horovitz, R. a J. Janssen, Z. V Vardeny, Spectroscopic studies of photoexcitations in regioregular and regiorandom polythiophene films, *Adv. Funct. Mater.* 12 (2002) 587. doi:10.1002/1616-3028(20020916)12:9<587.
- [200] D.E. Motaung, G.F. Malgas, C.J. Adrense, C.J. Oliphant, D. Knoesen, G. Malgas, The influence of thermal annealing on the morphology and structural properties of a conjugated polymer in blends with an organic acceptor material, *J. Mater. Sci.* 44 (2009) 3129.
- [201] W.R. SALANEC, Conformational defects in a conducting polymer, 30 (1989) 403–416.  
doi:10.1080/00107518908221989.
- [202] A.B. Kaiser, Systematic conductivity behavior in conducting polymers: Effects of heterogeneous disorder, *Adv. Mater.* 13 (2001) 927–941. doi:10.1002/1521-4095(200107)13:12/13<927::AID-ADMA927>3.0.CO;2-B.
- [203] J. Li, K. Fang, H. Qiu, S. Li, W. Mao, Micromorphology and electrical property of the HCl-doped and DBSA-doped polyanilines, 142 (2004) 107–111.  
doi:10.1016/j.synthmet.2003.08.014.
- [204] D.S. Maddison, T.L. Tansley, Variable range hopping in polypyrrole films of a range of conductivities and preparation methods Variable range hopping in polypyrrole and preparation methods films of a range of conductivities, 72 (1992) 4677–4682.  
doi:10.1063/1.352073.
- [205] R. Singh, A.K. Narula, R.P. Tandon, A. Mansingh, S. Chandra, R. Singh, A.K. Narula, R.P. Tandon, Mechanism of charge transport in polypyrrole, poly (N-methyl pyrrole) and their copolymers Mechanism of charge transport in polypyrrole, poly (N-methyl pyrrole) and their copolymers, 79 (1996) 1476–1480. doi:10.1063/1.360987.
- [206] B.W. Knight, F. Wudl, Preparation and Characterization of Fulleroid and Methanofullerene Derivatives, *J. Org. Chem.* 60 (1995) 532–538.  
doi:10.1021/jo00108a012.
- [207] C.J. Brabec, N.S. Sariciftci, J.C. Hummelen, Plastic solar cells, *Adv.*

- Funtional Mater. 11 (2001) 15–26.  
doi:10.1002/1616-3028(200102)11:1<15::AID-ADFM15>3.0.CO;2-A.
- [208] R. Singhal, D.C. Agarwal, Y.K. Mishra, D. Kabiraj, G. Mattei, J.C. Pivin, R. Chandra, D.K. Avasthi, Synthesis, characterizations, and thermal induced structural transformation of silver-fullerene C<sub>60</sub> nanocomposite thin films for applications in optical devices, *J. Appl. Phys.* 107 (2010). doi:10.1063/1.3366709.
- [209] R. Singhal, D.C. Agarwal, Y.K. Mishra, F. Singh, J.C. Pivin, R. Chandra, D.K. Avasthi, Electronic excitation induced tuning of surface plasmon resonance of Ag nanoparticles in fullerene C<sub>70</sub> matrix, *J. Phys. D. Appl. Phys.* 42 (2009) 155103. doi:10.1088/0022-3727/42/15/155103.
- [210] R. Singhal, D.C. Agarwal, S. Mohapatra, Y.K. Mishra, D. Kabiraj, F. Singh, D.K. Avasthi, A.K. Chawla, R. Chandra, G. Mattei, J.C. Pivin, Synthesis and characterizations of silver-fullerene C<sub>70</sub> nanocomposite, *Appl. Phys. Lett.* 93 (2008) 91–94. doi:10.1063/1.2976674.
- [211] G.B.V.S. Lakshmi, A. Dhillon, A.M. Siddiqui, M. Zulfequar, D.K. Avasthi, RF-plasma polymerization and characterization of polyaniline, *Eur. Polym. J.* 45 (2009) 2873–2877. doi:10.1016/j.eurpolymj.2009.06.027.
- [212] S. Ameen, G.B.V.S. Lakshmi, M. Husain, Synthesis and characterization of polyaniline prepared with the dopant mixture of (ZrO<sub>2</sub>/PbI<sub>2</sub>), *J. Phys. D. Appl. Phys.* 42 (2009) 105104. doi:10.1088/0022-3727/42/10/105104.
- [213] S. Malik, N. Fujita, P. Mukhopadhyay, Y. Goto, K. Kaneko, T. Ikeda, S. Shinkai, Creation of 1D [60]fullerene superstructures and its polymerization by  $\gamma$ -ray irradiation, *J. Mater. Chem.* 17 (2007) 2454. doi:10.1039/b701583f.
- [214] B.W. Ma, C. Yang, X. Gong, K. Lee, A.J. Heeger, Thermally Stable, Efficient Polymer Solar Cells with Nanoscale Control of the Interpenetrating Network Morphology \*\*, (2005) 1617–1622. doi:10.1002/adfm.200500211.
- [215] T. Sharma, R. Singhal, R. Vishnoi, P. Sharma, A. Patra, S. Chand, G.B.V.S. Lakshmi, S.K. Biswas, Electronic excitation induced modifications of optical and morphological properties of PCBM thin films, *Nucl. Instruments Methods Phys. Res. Sect. B Beam Interact. with Mater. Atoms.* 379 (2015) 176–180. doi:10.1016/j.nimb.2016.03.029.
- [216] A. Dzwilewski, T. Wågberg, L. Edman, Photo-induced and resist-free imprint patterning of fullerene materials for use in functional electronics, *J. Am. Chem. Soc.* 131 (2009) 4006–4011. doi:10.1021/ja807964x.
- [217] F. Piersimoni, G. Degutis, S. Bertho, K. Vandewal, D. Spoltore, T. Vangerven, J. Drijkoningen, M.K. Van Bael, A. Hardy, J. D’Haen, W. Maes, D. Vanderzande, M. Nesladek, J. Manca, Influence of fullerene photodimerization on the

- PCBM crystallization in polymer:  
Fullerene bulk heterojunctions under  
thermal stress, *J. Polym. Sci. Part B  
Polym. Phys.* 51 (2013) 1209–1214.  
doi:10.1002/polb.23330.
- [218] E. Klimov, W. Li, X. Yang, G.G.  
Hoffmann, J. Loos, Scanning near-field  
and confocal Raman microscopic  
investigation of P3HT-PCBM systems  
for solar cell applications,  
*Macromolecules*. 39 (2006) 4493–4496.  
doi:10.1021/ma052590x.
- [219] S. Berhanu, F. Tariq, T. Jones, D.W.  
McComb, Three-dimensionally  
interconnected organic nanocomposite  
thin films: implications for donor-  
acceptor photovoltaic applications, *J.  
Mater. Chem.* 20 (2010) 8005–8009.  
doi:10.1039/c0jm01030h.



# List of Publications

1. Electronic excitation induced modifications of optical and morphological properties of PCBM thin films; **T. Sharma**, R. Singhal, R. Vishnoi, P. Sharma, A. Patra, S. Chand, G.B.V.S. Lakshmi, S.K. Biswas, Nuclear Instruments and Methods in Physics Research B 379 (2016) 176–180.
2. Ion irradiation induced modifications of P3HT: A donor material for organic photovoltaic devices; **T. Sharma**, R. Singhal, R. Vishnoi, G.B.V.S. Lakshmi, S. Chand, D.K. Avasthi, A. Kanjilal, S.K. Biswas, Vacuum 135 (2017) 73-85.
3. Influence of high energy ion irradiation on fullerene derivative (PCBM) thin films; **Trupti Sharma**, Rahul Singhal, Ritu Vishnoi, G.B.V.S. Lakshmi, S.K. Biswas, Nuclear Instruments and Methods in Physics Research B 396 (2017) 5–10.
4. Effect of High Energy Ions on the Electrical and Morphological Properties of Poly(3-Hexylthiophene) (P3HT) Thin Film; **Trupti Sharma**, R. Singhal, R. Vishnoi, G. D. Sharma, S. K. Biswas, Physica B: Condensed Matter 537 (2018) 306-313.



## Bio-data

### **Trupti Sharma**

M. Sc., Ph. D.

Department of Physics,

Malaviya National Institute of Technology Jaipur

JLN Marg, Malaviya Nagar, Jaipur- 302017 (Rajasthan)

Mob:- 9509677611

Email: [tsphy91@gmail.com](mailto:tsphy91@gmail.com), [2013rph9504@mnit.ac.in](mailto:2013rph9504@mnit.ac.in)



---

### Carrier Objective:

Seeking a position in the academic/research field related to impart the learning of fundamental & applied physics and material sciences.

### Detail of Educational Qualifications:

Exam	Board/ University	Division	Year of passing	Percentage	Subjects
10 <sup>th</sup>	Rajasthan board	First	2005	68	Hindi, English, Mathematics, sciences, <del>Social Sciences</del>
12 <sup>th</sup>	Rajasthan board	First	2007	61.08	Hindi, English, Mathematics, Physics, Chemistry
B.Sc. Hons.	University Maharani's college	First	2011	66	Physics, Mathematics
M.Sc.	Malaviya National Institute of Technology, Jaipur	First	2013	82.2	Physics
Ph.D.	Malaviya National Institute of Technology Jaipur	-----	2018	84 (course work)	Physics

### Research Carrier:

## **Ph.D. (Physics)**

**Thesis title:** “*Study on Ion Irradiation Induced Modifications of P3HT and PCBM materials*”

**Supervisor:** Dr. Rahul Singhal, Asst. Prof., Malaviya National Institute of Technology Jaipur.

**Second Supervisor:** Prof. S. K. Biswas, Malaviya National Institute of Technology Jaipur.

## **Experimental Skills:**

- Thermal evaporation
- Spin-coating thin film deposition
- X-ray photoelectron spectroscopy (XPS)
- X-ray diffraction spectroscopy (XRD)
- UV-Visible spectroscopy
- Atomic force microscopy (AFM)
- Raman Spectroscopy
- Electrical measurements
- Photo-luminescence spectroscopy (PL)
- FTIR spectroscopy

## **Personal Particulars:**

**Name:**

**Trupti Sharma**

**Date of Birth:**

10-10-1991

**Permanent Address:**

380-B, Surya Nagar, Gopal Pura Bypass, Jaipur  
Pin- 302015

**Mobile No.:**

9509677611



**(Trupti Sharma)**